

**Infrared Spectroscopy of the Transiting Extrasolar  
Planet HD 209458 b During Secondary Eclipse**

by

**Lee Jeremy Richardson**

M.S., University of Colorado, 1999

B.S., West Virginia University, 1997

A thesis submitted to the  
Faculty of the Graduate School of the  
University of Colorado in partial fulfillment  
of the requirements for the degree of  
Doctor of Philosophy  
Department of Physics

2003

© 2003 by Lee Jeremy Richardson

This thesis entitled:  
Infrared Spectroscopy of the Transiting Extrasolar Planet HD 209458 b During  
Secondary Eclipse  
written by Lee Jeremy Richardson  
has been approved for the Department of Physics

---

Drake Deming

---

Dr. Mihaly Horanyi

---

Dr. Larry W. Esposito

---

Dr. Scott Robertson

---

Dr. Timothy M. Brown

Date \_\_\_\_\_

The final copy of this thesis has been examined by the signatories, and we find that both the content and the form meet acceptable presentation standards of scholarly work in the above mentioned discipline.

Richardson, Lee Jeremy (Ph.D., Physics)

Infrared Spectroscopy of the Transiting Extrasolar Planet HD 209458 b During  
Secondary Eclipse

Thesis directed by Dr. Drake Deming

We present spectroscopic observations that place strong limits on the atmospheric structure of the transiting extrasolar planet HD 209458 b. The discovery of the transit has led to several new observations that have provided the most detailed information on the physical properties of a planet outside the solar system. These observations have concentrated on the primary eclipse, the time at which the planet crosses in front of the star as seen from Earth. The measurements have determined the basic physical characteristics of the planet, including radius, mass, average density, and orbital inclination, and have even refined values of the stellar mass and radius. Transmission spectroscopy of the system during primary eclipse resulted in the first detection of the atmosphere of an extrasolar planet, with the measurement of the sodium doublet.

The present work discusses the first reported attempts to detect the secondary eclipse, or the disappearance of the planet behind the star, in the infrared. We devise the method of ‘occultation spectroscopy’ to detect the planetary spectrum, by searching in combined light for subtle changes in the shape of the spectrum as the planet passes behind the star. Predicted secondary eclipse events were observed from the Very Large Telescope (VLT) on UT 8 and 15 July 2001 using the Infrared Spectrometer and Array Camera (3.5–3.7  $\mu\text{m}$ ). Further observations from the NASA Infrared Telescope Facility (IRTF) using the SpeX instrument (1.9–4.2  $\mu\text{m}$ ) included two predicted secondary eclipse events on UT 20 and 27 September 2001. Analysis of these data reveal a statistically signifi-

cant non-detection of the planetary spectrum. The results place strong limits on the structure of the planetary atmosphere and reject widely-accepted models for the planet that assume the incident stellar radiation is completely absorbed and re-emitted in the substellar hemisphere. Situations that remain consistent with our data include an isothermal atmosphere or the presence of a high absorptive or reflective cloud. The latter case is also consistent with the observed low sodium abundance from transmission spectroscopy. These results represent the strongest limits to date on the temperature structure of the planetary atmosphere.

## Acknowledgements

I would like to extend my heartfelt and sincere thanks to my research advisor, Drake Deming, for his insightful ideas and instantaneous feedback on my work. His enthusiasm and support have motivated me to see this project through to completion.

I thank Guenter Wiedemann for performing the observations from the VLT that I have analyzed in this work. I thank Sara Seager for insightful discussions on radiative transfer and modeling problems. I thank the other members of my thesis committee, Larry Esposito, Tim Brown, Mihaly Horanyi, and Scott Robertson. I also thank Joe Harrington and Cedric Goukenleuque.

This work has been supported primarily by a fellowship through the NASA Graduate Student Researchers Program, funded by the Office of Space Science at NASA Headquarters (grant number NGT5-50273).

Finally, on a more personal note, I would like to thank Gary Rottman, George Lawrence, Jerry Harder, and Dan Baker of LASP for their support of my decision to take on this project. Thanks to my classmates and friends Kurt Miller and Heather Lewandowski for their support throughout my time in graduate school and to my friends Jeff Baltrush, Joe Cook, Ken White, and Ken Rub for being there when I needed them most. I thank my parents, Warren and Rosella Richardson, for their undying love and encouragement, and my brother Cris for his love and acceptance, far beyond what I ever imagined.

## Contents

### Chapter

<b>1</b>	Motivation	1
1.1	History . . . . .	2
1.2	Background . . . . .	2
1.3	A Transiting Planet . . . . .	4
1.4	The Secondary Eclipse . . . . .	7
1.5	Outline . . . . .	8
<b>2</b>	Atmospheric Calculations	9
2.1	Review of Radiative Transfer . . . . .	9
2.1.1	Definitions . . . . .	9
2.1.2	Blackbody Radiation Law . . . . .	11
2.1.3	Interactions with Matter . . . . .	12
2.1.4	The Radiative Transfer Equation and its Solution . . . . .	13
2.1.5	Limiting Cases . . . . .	14
2.1.6	Line Formation and Line Shape . . . . .	15
2.2	Spectral Synthesis Calculations . . . . .	18
2.2.1	Elemental Composition . . . . .	19
2.2.2	The Temperature-Pressure Profile in Radiative Equilibrium	20
2.2.3	The Continuous Opacity . . . . .	23

2.2.4	Line Opacities . . . . .	24
2.2.5	Integration of the Radiative Transfer Equation . . . . .	28
2.2.6	Stellar Spectrum . . . . .	29
2.3	Testing and Optimization of Code . . . . .	29
2.4	Results . . . . .	31
<b>3</b>	<b>Observational Methodology</b>	<b>33</b>
3.1	Introduction to Occultation Spectroscopy . . . . .	33
3.2	Feasibility Arguments . . . . .	35
3.2.1	Blackbody Calculations . . . . .	35
3.2.2	Reflected Starlight . . . . .	39
3.2.3	The Observation Limit . . . . .	41
3.3	Infrared Astrophysics Basics . . . . .	42
3.4	Ephemeris Calculations . . . . .	43
3.5	A Note on the Comparison Star . . . . .	46
3.6	Observational Summary . . . . .	49
<b>4</b>	<b>VLT Observations and Analysis</b>	<b>51</b>
4.1	Introduction . . . . .	51
4.2	The Concept of Occultation Spectroscopy . . . . .	53
4.3	Observational Summary . . . . .	55
4.4	Modeled Spectrum . . . . .	56
4.5	Data Analysis . . . . .	60
4.5.1	Spectral Extraction . . . . .	60
4.5.2	Telluric Correction . . . . .	62
4.5.3	Higher-order Corrections . . . . .	64
4.5.4	Fit to the Planetary Spectrum . . . . .	67
4.5.5	Checks on the Analysis . . . . .	68

4.5.6	Secondary Eclipse Timing . . . . .	70
4.6	Results and Discussion . . . . .	71
<b>5</b>	<b>IRTF Observations and Analysis</b>	<b>76</b>
5.1	Introduction . . . . .	76
5.2	Observations . . . . .	77
5.3	Analysis . . . . .	79
5.3.1	Spectral Extraction . . . . .	79
5.3.2	Corrections to the Extracted Spectra . . . . .	80
5.3.3	Difference Spectra . . . . .	82
5.3.4	Averaging over Wavelength . . . . .	84
5.3.5	Fit to Eclipse Curve . . . . .	86
5.4	Model Calculations . . . . .	88
5.5	Results and Interpretation . . . . .	92
5.6	Conclusion . . . . .	97
<b>6</b>	<b>Conclusion</b>	<b>100</b>
6.1	Implications for HD 209458 b . . . . .	100
6.2	The Effect of Clouds on Temperature Structure . . . . .	102
6.3	Continuing Work . . . . .	107
6.4	Future Studies . . . . .	109
6.4.1	Day-Night Temperature Asymmetry . . . . .	109
6.4.2	Space-Based Observations . . . . .	110
6.5	In Closing . . . . .	111

**Bibliography**

113

**Appendix****A List of Acronyms**

117

## Tables

### Table

1.1	Physical Characteristics of HD 209458 b . . . . .	5
2.1	Elemental Abundances . . . . .	20
3.1	Telescope Locations . . . . .	44
3.2	Favorable Secondary Eclipse Events . . . . .	46
3.3	Stellar Data, Including Both Comparisons . . . . .	47
3.4	Overall Observational Summary . . . . .	48
4.1	Stellar Photometric Data . . . . .	55
5.1	Detection Failures for Fiducial Cases . . . . .	94
5.2	Detection Failures for $f = 1$ Scaled Profiles . . . . .	96

## Figures

### Figure

2.1	Fiducial Temperature-Pressure Profiles . . . . .	22
2.2	Effect of Strength Cutoff on Resulting Spectrum . . . . .	26
2.3	Line Strengths for Carbon Monoxide . . . . .	27
2.4	Line Strengths for Methane . . . . .	28
2.5	Stellar Flux Comparison . . . . .	30
2.6	Planetary Flux in Isothermal Atmosphere . . . . .	31
2.7	Fiducial Results for Relative Flux Density . . . . .	32
3.1	Approximate Relative Flux as Function of Wavenumber . . . . .	37
3.2	Theoretical Primary and Secondary Eclipse Curves . . . . .	38
3.3	Observation Limit for IRTF . . . . .	42
3.4	IRTF Observation Summary, UT 27 Sep 2001 . . . . .	49
4.1	Temperature/Pressure Profiles . . . . .	58
4.2	Model Spectra . . . . .	59
4.3	Sample Extracted Spectra . . . . .	63
4.4	Sample Residual Spectra . . . . .	66
4.5	Noise Distribution of Residuals . . . . .	69
4.6	Noise Distribution of Calculated Model Amplitudes . . . . .	70
4.7	Model Amplitude vs. Time for Eccentricity of 0.01 . . . . .	73

4.8	Model Amplitude vs. Time for Zero Eccentricity . . . . .	74
5.1	Sample Extracted IRTF Spectra . . . . .	81
5.2	Sample Binned Difference Spectra . . . . .	85
5.3	Final Difference Spectrum, Out-of-Eclipse Minus In-Eclipse . . . . .	87
5.4	Temperature-Pressure Profiles of Fiducial Models . . . . .	91
5.5	Planet to Star Contrast for Fiducial Models . . . . .	93
5.6	Number of Detection Failures vs. Temperature Difference . . . . .	95
6.1	Effect of Clouds on Temperature Structure . . . . .	108

## Chapter 1

### Motivation

Through the ages, humans have looked to the stars and wondered about our place in the Universe. How did we get here? Are we alone? Even as our knowledge has increased dramatically over the centuries, these fundamental questions remain. The study of extrasolar planets is providing new knowledge of our physical Universe that will hopefully someday help to answer these questions. Until the first extrasolar planet was discovered in 1995, our Solar System was the only example astronomers could use in devising models of planetary formation. With the discovery of whole new classes of planets, our understanding of the general nature of solar system formation has changed significantly, and new models are being developed to predict planetary formation and explain observational results (e.g., Boss, 2001; Armitage & Bonnell, 2002). By characterizing extrasolar planets we can help distinguish between evolutionary models and gain insight into the formation of planets.

This work explores observations of one extrasolar planet, HD 209458 b, the first one to be discovered that exhibits a **transit** of its parent star. That is, as seen from Earth, the planet travels directly in front of the star and blocks a portion of the emergent starlight. This special circumstance has allowed many new and exciting observations to be performed, and this planet has become the most well-characterized of any of the 105 extrasolar planets known to date. Our

observations of the secondary eclipse, that is, the time when the planet disappears behind the star, have added to this body of knowledge. In this work, we describe a new observational technique designed to detect the secondary eclipse, demonstrate the technique by describing our observations and the results of the analysis for HD 209458 b, and discuss the implications for the physical structure and composition of the planet.

## 1.1 History

At the beginning of the twentieth century, the astronomer E. E. Barnard discovered a star with an extraordinarily high proper motion (Barnard, 1916). The star, which later became known as Barnard's Star, is a faint red dwarf and the second-closest star to Earth. After some two decades of observations, van de Kamp (1963) announced that he had deduced the presence of a companion planet orbiting Barnard's Star, based on measured accelerations. Although the planet has never been confirmed, the question of whether it exists has been debated for years. Van de Kamp never wavered in his conviction that it did in fact exist, right up to his death in 1995 (Mammana & McCarthy, Jr., 1995).

## 1.2 Background

The first confirmed extrasolar planets were detected around pulsars by measuring small changes in timing information (Wolszczan & Frail, 1992). However, because of the extreme radiation environment, these objects almost certainly do not resemble anything in our own solar system. The first extrasolar planet found orbiting a solar-like star was 51 Pegasi b (Mayor & Queloz, 1995), and it was discovered using the radial velocity technique. By far the most successful detection method, the radial velocity technique accounts for nearly all of the extrasolar planets discovered to date. Because a star and orbiting companion effectively

both orbit the center of mass of the system, a measurement of the stellar ‘wobble’ reveals the presence of a planet. The radial velocity technique searches for periodic Doppler shifts in the spectrum of a star, due to the motion of the star along the line of sight toward Earth. Although this idea is not new, dramatic improvements in the experimental techniques during the 1990s, particularly the development of the iodine absorption cell for use as a reference spectrum (Marcy & Butler, 1992), have led to measurements of stellar radial velocities with errors of only 3 m/s (Butler et al., 1996). Given that Jupiter causes a shift in the solar spectrum of  $\sim 12$  m/s, the technique could now begin to detect gas giants around other stars.

The radial velocity technique provides a direct measurement of the period of the planet, and therefore the orbital radius from Kepler’s Third Law. However, since the technique is sensitive only to stellar motion along the line of sight from Earth, only the minimum mass  $M \sin i$  is determined, since the orbital inclination  $i$  of the planetary companion remains unknown. The technique also provides other orbital information about the planet, including the orbital eccentricity. In addition, the radial velocity curves also indicate the time of a possible crossing of the planet in front of or behind the star; each time the velocity reaches zero, both objects would be moving perpendicular to the line of sight. Using this information, observers know the precise times at which to look for planetary transits.

A host of ongoing programs employ the radial velocity technique to search for planets around solar-like stars. One of the leading teams, led by Geoff Marcy and Paul Butler, notes that over 1000 have been surveyed, representing a nearly complete sample of the solar-type stars within 30 pc of the Sun.<sup>1</sup> One limitation of the method is that it can only be used on so-called ‘quiet’ stars, i.e., ones with low chromospheric activity, to ensure that the periodic signal is truly due

---

<sup>1</sup> <http://exoplanets.org/science.html>

to the orbiting companion, rather than a stellar effect. Even so, with such a large sample of radial velocities and detected planets, useful statistics on the frequency of planets and the mass distribution of planets are now available. Marcy & Butler (2000) note that, as of two years ago, some 5% of planets around main-sequence stars harbor planets of  $(0.5 - 8) M_J$ . The method is biased toward more massive objects orbiting close to the primary star, and after only a few years of observations, it became clear that a new ‘class’ of planets had emerged. These are gas giants that orbit at a distance of less than 0.1 AU from the primary star, and they are sometimes referred to as ‘hot Jupiters’ or ‘close-in extrasolar giant planets’ (CEGP’s).

### 1.3 A Transiting Planet

Assuming a random orientation of orbits, a simple geometrical argument gives the chance that a planet will eclipse the parent star as seen from Earth. The probability is simply  $P = d_*/a$ , where  $d_*$  is the diameter of the star and  $a$  is the orbital radius of the planet. For the close-in planets,  $a \leq 0.1$  AU, and the probability of observing a planetary transit is  $\simeq 10\%$ . About 18 such planets are currently known.

One such close-in planet was discovered in 1999 around the star HD 209458 by radial velocity measurements (Mazeh et al., 2000). Follow-up observations revealed that the starlight dimmed by  $\simeq 1.6\%$  periodically at the expected times given by the radial velocity measurements. This discovery, reported nearly simultaneously by two independent groups (Charbonneau et al., 2000; Henry et al., 2000), represents the first extrasolar planet known to exhibit a transit across its parent star. Other researchers subsequently reported the discovery of the transit in the Hipparcos photometry data set (Robichon & Arenou, 2000; Castellano et al., 2000). The detection of the **primary eclipse** (which occurs when the

Table 1.1: Currently accepted values of the physical parameters of HD 209458 b.

Parameter (units)	Value	Uncertainty
Radius <sup>a,b</sup> (R <sub>J</sub> )	1.42	+0.10 -0.13
Mass <sup>a,b</sup> (M <sub>J</sub> )	0.685	±0.02
Orbital Period <sup>c</sup> (days)	3.5247542	±0.0000044
Orbital Inclination <sup>c</sup> (°)	86.135	±0.104
Orbital Semi-Major Axis <sup>d</sup> (AU)	0.0468	
Orbital Eccentricity <sup>e</sup>	0.011	±0.015

<sup>a</sup>Value reported in terms of Jupiter value.

<sup>b</sup>Cody & Sasselov (2002)

<sup>c</sup>Schultz et al. (2003)

<sup>d</sup>Brown et al. (2001b)

<sup>e</sup>G. Marcy (private communication, 2002)

planet passes in front of the star) led immediately to the most detailed knowledge of the physical characteristics of any known extrasolar planet. With the orbital inclination now known, the true mass ( $\simeq 70\%$  that of Jupiter) could be determined, and the planetary radius ( $\simeq 40\%$  larger than that of Jupiter) could be calculated from the depth of the eclipse, since the eclipse depth is directly proportional to the ratio of the planetary to stellar area. This led immediately to an estimate of the average density of the planet,  $0.3 \text{ g/cm}^3$  (based on updated planetary parameters in Cody & Sasselov (2002)), confirming that the object is, in fact, a gas giant (Burrows et al., 2000). A summary of the basic physical characteristics of HD 209458 b is given in Table 1.1.

Because of the orientation of the planet's orbital plane, many new observations are now possible, and HD 209458 b has become the most well studied of any known extrasolar planet. Follow-up measurements of the primary eclipse have been performed by Brown et al. (2001b) using the Space Telescope Imaging Spectrograph (STIS) on the Hubble Space Telescope. These observations resulted in a spectacular primary eclipse curve, which not only helped refine the planetary mass and radius estimates, but in fact also led to a more accurate determination

of the stellar radius.

One of the most exciting observational possibilities is the concept of performing transmission spectroscopy on the planet. Considering a gas giant with an extended atmosphere, one can envision the absorption of starlight passing through the annulus of the planet's atmosphere as it crosses in front of the star as viewed from Earth. Theorists have studied this well-known idea and its applications to transiting extrasolar planets (Seager & Sasselov, 2000; Brown, 2001). In particular, Seager & Sasselov (2000) suggest that strong absorption effects of Na I, K I, and He I may be observable, but they point out that the strength and number of such absorptions is sensitive to the level of the cloud top.

With the discovery of HD 209458 b, observers have begun to measure the primary eclipse with higher spectral resolution to look for evidence of absorption in the planet's atmosphere. One such effort led to the first detection of an extrasolar planet atmosphere (Charbonneau et al., 2002), and they find that the column density of sodium is reduced by a factor of 3 from model predictions. Bundy & Marcy (2000) searched for transit effects in HD 209458 as well as in 51 Pegasi. Finally, Brown et al. (2002) attempted to detect CO during a planetary transit of HD 209458 b; although their measurements were unsuccessful, they suggest that better observing conditions would make this measurement feasible.

A host of programs are currently underway or are being developed that search for extrasolar planetary transits. One ambitious project is the Kepler mission, a Discovery-class mission that is a space-based telescope to search for transits of Earth-sized planets in the habitable zone around nearby solar-like stars. With its five-year mission life, Kepler could reveal a few hundred Earth-sized planets, as well as over one thousand giant planets, depending on the frequency of planet formation (Borucki et al., 2002). Most recently, a second transiting planet has been reported, discovered by the Optical Gravitational Lensing Experiment

(OGLE) team. The planet, catalogued OGLE-TR-56b, has the smallest orbital period of any known extrasolar planet ( $\simeq 1.2$  days) and is the first planet to be discovered using the transit method.

#### 1.4 The Secondary Eclipse

The observations discussed thus far have been concerned with what I have called the **primary eclipse**, or the time that the planet passes in front of the star. I make a clear distinction between this and the **secondary eclipse**, which occurs when the planet disappears behind the star. The possibility of detecting the secondary eclipse in the infrared was first suggested by Charbonneau et al. (2000). No detection of the secondary eclipse has been made to date. Our observations are among the first attempts to detect the secondary eclipse, and they are certainly the most sensitive. Although we concentrate here on observing direct radiation from the planet, it is worth noting that reflected starlight from the planetary atmosphere is another possibility for detecting the planet. This method would apply to non-transiting planets as well, and in fact, Charbonneau et al. (1999) placed an upper limit on reflected light from the planet orbiting  $\tau$  Bootis.

It is also worth clarifying the meaning of ‘direct’ radiation. This refers not only to the radiative output from the planet’s internal energy source but also to the shortwave stellar radiation that is absorbed by the planetary atmosphere and re-emitted as longwave radiation. Clearly, the infrared region is of interest for observing this type of planetary radiation; in the visible region, where the primary eclipse has been observed, the direct planetary radiation is insignificant compared to the reflected stellar radiation. Since the planet is expected to be hot ( $T \sim 1400$  K for zero albedo), a simple blackbody argument reveals that the planetary output is possibly as much as 0.1% that of the star (for  $\lambda = 3.6 \mu\text{m}$ ). Although this is a small signal, we argue in Chapter 3 that it is attainable from the

ground with careful measurements and good atmospheric conditions. A detection of the secondary eclipse in the infrared would therefore represent the first detection of radiation emitted by an extrasolar planet, and would yield the first observational estimate of the temperature of a planet outside the solar system.

## 1.5 Outline

To close Chapter 1 we describe briefly the organization of the rest of this work. Chapter 2 reviews the fundamental equations and concepts of radiative transfer and describes the spectral synthesis calculations used in the subsequent analysis. Chapter 3 gives a general introduction to the observational methodology, as well as an overall summary of the observational data. Chapter 4 discusses the observations of two secondary eclipse events from the Very Large Telescope (VLT) and the results of the search for methane in the planetary atmosphere. Chapter 5 gives a similar discussion for the two secondary eclipse events observed from the NASA Infrared Telescope Facility (IRTF) and reports on analysis of the planetary spectrum from 2.0–2.5  $\mu\text{m}$ . Finally, Chapter 6 summarizes the implications of these observations for the atmospheric structure of HD 209458 b and discusses the exciting future observations of this and other extrasolar planets.

The field of extrasolar planet research is dynamic; the wealth of information grows almost daily. The number of known extrasolar planets increases so frequently that it is not worthwhile to provide a detailed summary in this work, because it would be outdated before the material went to press. I refer the interested reader to the Extrasolar Planets Encyclopedia, an excellent website maintained by Jean Schneider.<sup>2</sup> The site is a valuable resource, containing up-to-date information on known extrasolar planets and their characteristics, detection methods, references, scientific meetings and workshops, and other news.

---

<sup>2</sup> <http://www.obspm.fr/encycl/encycl.html>

## Chapter 2

### Atmospheric Calculations

This project has focused on the observations of the transiting planet and the reduction of these data. In order to interpret the results, however, we present calculations describing the atmospheric structure of the planet. While modeling of planetary atmospheres is a vast and highly specialized subject, the calculations presented here represent a helpful way of interpreting the observational results and placing useful constraints on the structure of the atmosphere of HD 209458 b.

#### 2.1 Review of Radiative Transfer

We begin with a brief summary of the basic ideas and equations of radiative transfer. A wealth of useful textbooks are available on the subject (e.g. Liou, 2002; Salby, 1996; Goody, 1995), and any of these would provide a more complete description. For our purposes, however, it is sufficient to provide an overview as a starting point for the subsequent calculations relating to HD 209458 b. Much of the following discussion follows the description of the principles of radiative transfer in Salby (1996, Chapter 8) and Liou (2002, Chapter 1).

##### 2.1.1 Definitions

No description of radiative transfer, however brief, is complete without a summary of the basic radiative quantities. The nomenclature describing these

quantities is often confusing and inconsistent from different sources. As a basis for the following discussion, we first recall the well-known relation between frequency and wavelength,

$$\lambda f = c, \quad (2.1)$$

where  $c$  is the speed of light in a vacuum,  $\lambda$  is the wavelength, and  $f$  represents the frequency. Also, the wavenumber  $\nu$  is defined by

$$\nu = \frac{1}{\lambda} \quad (2.2)$$

and is often measured in inverse centimeters ( $\text{cm}^{-1}$ ).

Following convention, we consider a pencil of radiation traveling through a medium. The energy in the beam is given by

$$dE_\nu = I_\nu(\mathbf{r}, \mathbf{n}, t) \cos \theta dA d\Omega d\nu dt, \quad (2.3)$$

where  $I_\nu$  is the monochromatic (spectral) **radiance** (which depends on the position vector  $\mathbf{r}$  and the direction  $\mathbf{n}$ ),  $\theta$  is the angle from the normal to the surface, and  $\Omega$  is the solid angle in steradians. From Equation 2.3 we see that the radiance, which is often called intensity, has units of energy/(area · time · solid angle · wavenumber). (I will avoid the use of the term intensity, because it is frequently used incorrectly and leads to confusion.) Furthermore, we can define the monochromatic flux density by integrating over the solid angle:

$$\mathbf{F}_\nu = \int I_\nu(\mathbf{r}, \mathbf{n}, t) \cdot \mathbf{n} d\Omega \quad (2.4)$$

The flux density is in general a vector quantity, until we choose a coordinate system and calculate the flux density through a surface, as in

$$F_\nu = \mathbf{F}_\nu \cdot \hat{\mathbf{k}} = \int_\Omega I_\nu(z, \theta, \phi) \cos \theta d\Omega. \quad (2.5)$$

The quantity  $F_\nu$  is also called the specific **irradiance**, and it has units of energy/(area · time · wavenumber). Here is another nomenclature trap; the flux density or irradiance is often incorrectly called ‘flux.’ In fact, the flux is calculated by an integration over area, as in

$$f_\nu = \int_A F_\nu dA. \quad (2.6)$$

Note that all the quantities described thus far have been defined as ‘spectral’ or ‘monochromatic’ quantities, meaning that they depend explicitly on wavenumber (or equivalently, wavelength). The word ‘spectral’ may be dropped and replaced by the word ‘total’ with a simple integration of the quantity over wavenumber. For example, the total flux density is calculated from

$$F = \int_\nu F_\nu d\nu \quad (2.7)$$

and similarly for the other quantities described above.

### 2.1.2 Blackbody Radiation Law

Next, we recall the definition of the Planck radiation law. Although the derivation is beyond the scope of this work, his formula for the radiation emitted or absorbed by a blackbody is

$$B_\lambda(T) = \frac{2hc^2}{\lambda^5(e^{hc/\lambda kT} - 1)}, \quad (2.8)$$

where  $k$  is Boltzmann’s constant,  $T$  is the temperature of the blackbody, and  $h$  is Planck’s constant. Note that  $B_\lambda(T)$  represents the monochromatic radiance of a blackbody; a factor of  $\pi$  shows up in the numerator if the radiation is assumed to be isotropic and we integrate over the solid angle to obtain the irradiance. Also, by enforcing the physical constraint that

$$B_\lambda d\lambda = B_\nu d\nu, \quad (2.9)$$

Equation 2.8 can also be written in terms of the wavenumber  $\nu$ :

$$B_\nu(T) = \frac{2hc^2\nu^3}{e^{hc\nu/kT} - 1}. \quad (2.10)$$

By integrating Equation 2.8 over wavelength and solid angle, we obtain the Stefan-Boltzmann Law, an expression for the total flux density of a blackbody:

$$F = \sigma T^4 \quad (2.11)$$

where  $\sigma = 5.67 \times 10^{-8} \text{ J m}^{-2}\text{s}^{-1}\text{K}^{-4}$  is the Stefan-Boltzmann constant.

### 2.1.3 Interactions with Matter

The beam of energy considered above interacts with the matter as it propagates. The radiative transfer equation is derived from an understanding of how the radiation beam changes as it propagates, and we therefore consider the processes that affect the radiation beam in a general sense. Consider a beam of radiation with spectral radiance  $I_\nu$  that after traversing a distance  $ds$  through a medium then has radiance  $I_\nu + dI_\nu$ . The amount of radiation removed from the beam can be written

$$dI_\nu = -k_\nu \rho I_\nu ds \quad (2.12)$$

where  $k_\nu$  represents the monochromatic extinction cross section and  $\rho$  is the mass density of the matter in the medium. The extinction cross section represents a sum of the cross sections due to absorption and scattering processes, as in

$$k_\nu = \sigma_{av} + \sigma_{sv} \quad (2.13)$$

Matter can emit radiation, adding to the total energy in the radiation beam. We can define an emission cross section  $j_\nu$  as

$$dI_\nu = j_\nu \rho ds \quad (2.14)$$

The source function  $S_\nu$  is defined as the ratio of the emission cross section to the scattering cross section:

$$S_\nu = \frac{j_\nu}{k_\nu} \quad (2.15)$$

Combining Equations 2.12, 2.14, and 2.15 and rearranging, we obtain

$$\frac{dI_\nu}{\rho k_\nu ds} = -I_\nu + S_\nu. \quad (2.16)$$

Equation 2.16 represents the fundamental radiative transfer equation in one dimension.

#### 2.1.4 The Radiative Transfer Equation and its Solution

The radiative transfer equation can be written in a more convenient form with only a few simple definitions. The displacement  $ds$  in the medium is not the most important physical variable when solving radiative transfer problems. The most relevant physical quantity is related to the amount of absorption that occurs in a given displacement  $ds$ . If we consider a plane-parallel atmosphere, we are typically interested in the radiation flowing in the vertical direction. Note that

$$ds = \cos \theta dz, \quad (2.17)$$

and we can define

$$\mu = \cos \theta \quad (2.18)$$

where  $\theta$  is the angle measured from the vertical, or the zenith angle. We can now define the **optical depth**  $\tau$  as

$$\tau_\nu(z) = - \int_z k_\nu(z) \rho(z) dz. \quad (2.19)$$

The minus sign appears because the optical depth is by convention measured from the top of the atmosphere increasing downward. Using the definition of the optical

depth, we can rewrite Equation 2.16 as

$$\mu \frac{dI_\nu}{d\tau} = I_\nu - S_\nu. \quad (2.20)$$

Note that the quantities  $I_\nu$  and  $S_\nu$  are both dependent on  $\tau$  and  $\mu$ . Equation 2.20 represents the basic radiative transfer equation for studying plane-parallel atmospheres in one dimension.

Although it is simple to write an analytic solution to Equation 2.20, solving it in practice turns out to be difficult. This is due, in part, to the fact that the specification of the source function  $S_\nu$  is not obvious. Since the source function accounts for all processes of absorption, emission, and scattering in the atmosphere, it can be quite difficult to obtain an analytic form for  $S_\nu$  suitable for substitution in Equation 2.20. However, if we assume that such an analytic form can be found, the formal solution to the radiative transfer equation, after using an integration factor  $e^{-\tau/\mu}$ , can be written

$$I_\nu(\tau_\nu, \mu) = I_\nu(\tau_\nu=0, \mu) e^{\tau_\nu(z)/\mu} - \int_{\tau_\nu=0}^{\tau_\nu=\tau_\nu(z)} S_\nu(\tau_\nu, z) e^{(\tau_\nu(z)-\tau_\nu)/\mu} \frac{d\tau_\nu}{\mu} \quad (2.21)$$

Given that a complex form of  $S_\nu$  could easily make the analytic solution of the integral in Equation 2.21 impossible, it is useful to consider two special cases where  $S_\nu$  is known to have a simple form.

### 2.1.5 Limiting Cases

First, consider the case when  $S_\nu = 0$ . This implies that the scattering and emission terms are negligible. Equation 2.20 reduces to

$$\mu \frac{dI_\nu}{d\tau} = I_\nu, \quad (2.22)$$

which can easily be integrated to obtain

$$I_\nu(z) = I_\nu(z=0) e^{\tau_\nu(z)/\mu}. \quad (2.23)$$

This equation is known as Beer's Law or Lambert's Law. It describes the dissipation of radiation as it travels through a medium.

Next consider the situation where the medium is in local thermodynamic equilibrium and suppose that scattering can be ignored. This implies that the medium is undergoing emission as well as absorption, and that the source function is simply equal to the Planck function from Equation 2.10:

$$S_\nu = B_\nu(T). \quad (2.24)$$

Substituting into Equation 2.20, we have

$$\mu \frac{dI_\nu}{d\tau} = I_\nu - B_\nu(T). \quad (2.25)$$

This equation is the one we will solve in the spectral synthesis procedures described below in Section 2.2.

### 2.1.6 Line Formation and Line Shape

We now return to the subject of absorption in the medium and turn specifically to subject of absorption lines. This will form a key part of the calculations performed in the spectral synthesis routines.

Discrete energy transitions lead to characteristic absorption lines at particular wavelengths in the spectrum of the atom. For molecules, these electronic transitions are not the only way to transfer energy. Imagining the molecule as a classical rigid body, we see it can store energy as translational, rotational, or vibrational energy. The latter two, like electronic transitions, are quantized and therefore give rise to discrete lines in the absorption spectrum of the molecule (Liou, 2002, p. 17). In the mid-infrared region of the electromagnetic spectrum, the region in which our observations were performed, the rotational and vibrational transitions are coupled, giving rise to a band of lines called the rotational-vibrational band.

For any real observation, the line spectrum is affected by external forces on the atom or molecule as well as energy losses, and thus, in a practical sense, infinitely sharp lines will not appear; rather, a spectrum with lines having a finite line width will be observed. The broadening of spectral lines occurs through three main mechanisms (Liou, 2002, p. 20): energy losses in emission, changes induced by collision effects (pressure broadening), and the Doppler effect. At the deepest layers in the atmosphere, broadening is dominated by the pressure effect, while higher in the atmosphere, a combination of the Doppler and pressure effects causes line broadening. We briefly state the basic equations governing these processes.

Pressure broadening is the process by which the line shape is distorted due to atomic and molecular collisions. The line shape is given by the Lorentz profile, as in

$$k_\nu = \frac{S}{\pi} \frac{\alpha}{(\nu - \nu_0)^2 + \alpha^2} = S f(\nu - \nu_0) \quad (2.26)$$

where  $k_\nu$  is the absorption coefficient,  $\nu_0$  is the central wavenumber of the absorption line, and  $\alpha$  is the half-width at half-maximum. The line strength parameter  $S$  represents an integration of the absorption coefficient over all wavelengths (Pugh & Rao, 1976). The quantity  $f(\nu - \nu_0)$  is called the line shape factor, and as Equation 2.26 suggests, it must be multiplied by the line strength in order to calculate the absorption coefficient, and ultimately, the opacity. For pressure broadening, the line shape factor is therefore given by

$$f_L(\nu - \nu_0) = \frac{1}{\pi} \frac{\alpha}{(\nu - \nu_0)^2 + \alpha^2}. \quad (2.27)$$

In the absence of collisions, there is still a line broadening effect due to the thermal motion of the particles. For non-relativistic motion ( $v \ll c$ ), where  $v$  represents the line-of-sight velocity of the particle, we recall the well-known formula for the Doppler shift in terms of wavenumber  $\nu$ :

$$\nu = \nu_0 \left( 1 \pm \frac{v}{c} \right). \quad (2.28)$$

We can insert this expression into the Maxwell-Boltzmann distribution for the thermal energy of the particles, and assuming the same relation between line strength and absorption coefficient as seen above in Equation 2.26, we have

$$k_\nu = \frac{S}{\alpha_D \sqrt{\pi}} \exp\left(-\frac{\nu - \nu_0}{\alpha_D}\right)^2, \quad (2.29)$$

where  $\alpha_D$  is the Doppler width,

$$\alpha_D = \nu_0 \sqrt{\frac{2k_B T}{mc^2}} \quad (2.30)$$

and the half-width at half-maximum is given by  $\alpha_D \sqrt{\ln 2}$ . Again, the line shape factor for Doppler broadening is then given by

$$f_D(\nu - \nu_0) = \frac{1}{\alpha_D \sqrt{\pi}} \exp\left(-\frac{\nu - \nu_0}{\alpha_D}\right)^2. \quad (2.31)$$

In some physical situations, we have an intermediate case, where we need a combination of the Lorentz and Doppler profiles to determine the line profile. As noted by Liou (2002), we can perform a convolution of the Lorentz and Doppler profiles to obtain

$$\begin{aligned} f_V(\nu - \nu_0) &= \int_{-\infty}^{\infty} f_L(\nu' - \nu_0) f_D(\nu - \nu') d\nu' \\ &= \frac{1}{\pi^{3/2}} \frac{\alpha}{\alpha_D} \int_{-\infty}^{\infty} \exp\left(-\frac{(\nu - \nu')^2}{\alpha_D^2}\right) d\nu'. \end{aligned} \quad (2.32)$$

This equation can be simplified by making a few substitutions, as in

$$f_V(\nu - \nu_0) = \frac{1}{\alpha_D \sqrt{\pi}} K(x, y), \quad (2.33)$$

where  $K(x, y)$  is the Voigt function, given by

$$K(x, y) = \frac{y}{\pi} \int_{-\infty}^{\infty} \frac{1}{y^2 + (x - t)^2} e^{-t^2} dt \quad (2.34)$$

and letting  $t = (\nu - \nu')/\alpha_D$ ,  $y = \alpha/\alpha_D$ , and  $x = (\nu - \nu_0)/\alpha_D$ . This turns out to be the general expression for the line shape function. In the limit of high pressures, this reduces to the Lorentz profile. We use the general Voigt profile in the subsequent spectral calculations.

## 2.2 Spectral Synthesis Calculations

In order to gain an understanding of radiative transfer problems and to interpret our observational data on HD 209458 b, we have implemented a set of computational routines to calculate synthetic spectra. The general idea behind any spectral synthesis routine is to calculate a theoretical spectrum based on physical arguments. The process consists of several distinct steps, as discussed by Nieminen & Ross (2001), including the determination of the source function, the calculation of the continuum opacity, the calculation of the line opacities, and ultimately the numerical integration of the radiative transfer equation. In this section we describe the details of this process and the specifics of the IDL code developed to implement it.

Since the physical structure of the atmosphere is largely unknown, we are not interested in calculations of an excessively elaborate nature. The purpose of the effort described here is to provide a relatively simple method for calculating spectra of HD 209458 b for comparison to the observational data. As such, we have included the most relevant processes and made simplifying assumptions whenever possible. More importantly, this allows us to get a general sense of the atmospheric physics, and by comparing different physical situations to the observational data, we will ultimately obtain a **model independent** result—that is, our results will not depend on any one model of the atmospheric structure of HD 209458 b. Instead, we will have a general idea of which physical situations are consistent and which are inconsistent with our observational data.

The planetary parameters we adopted correspond to those listed in Table 1.1. The value for the surface gravity of the planet,  $g = 842 \text{ cm s}^{-2}$ , is calculated from the law of gravitation, given the adopted values for the planetary mass, the stellar mass, and the orbital radius. HD 209458 is a G0V star very similar to

the Sun, with an effective temperature of  $T_* = 6000$  K.

### 2.2.1 Elemental Composition

In order to calculate mixing ratios later, we must make an assumption about the abundances of the elements. We make the typical assumption that the elemental abundances are identical to those of the Sun, given by Anders & Grevesse (1989). The values presented by Anders & Grevesse (1989) represent an exhaustive collection of abundance information for the elements and isotopes, based on evidence from meteorites and from the solar photosphere. In the subsequent calculations, we consider only the most important molecular species. The relevant elemental abundances for these species are shown in Table 2.1. However, for our model atmosphere, we assume that all of the hydrogen atoms are combined in molecular hydrogen,  $\text{H}_2$ . This is a valid assumption, given that the planet is a gas giant, and at these temperatures, hydrogen combines with itself to form molecular hydrogen. This changes the total number of molecules in the atmosphere, and therefore we have to adjust the relative abundances for H and He from the values shown in Table 2.1. Using these values, we can calculate the abundance fraction for  $\text{H}_2$  from

$$A_{\text{H}_2} = \frac{\frac{1}{2}A_{\text{H}}}{\frac{1}{2}A_{\text{H}} + A_{\text{He}}} \quad (2.35)$$

which reduces to  $A_{\text{H}_2} = 0.821$ . Similarly, the adjusted He abundance can be found from

$$A'_{\text{He}} = \frac{A_{\text{He}}}{\frac{1}{2}A_{\text{H}} + A_{\text{He}}} \quad (2.36)$$

which is  $A'_{\text{He}} = 0.179$ . These numbers are needed to compute the number densities and partial pressures of the species, as well as the mean molecular mass of the atmosphere, given by

$$\bar{m} = 2 A_{\text{H}_2} M_{\text{H}} + A'_{\text{He}} M_{\text{He}}. \quad (2.37)$$

Table 2.1: Values for elemental abundances based on data for the solar photosphere given by Anders & Grevesse (1989). Given as fraction of total number of atoms.

Element	Abundance Fraction
H	0.902
He	0.098
C	$3.63 \times 10^{-4}$
O	$8.51 \times 10^{-4}$

Using the results from Equations 2.35 and 2.36, we have  $\bar{m} = 2.374$ .

From the elemental abundance fractions calculated above for H<sub>2</sub> and the values for C and O listed in Table 2.1 we can calculate the abundances of three molecular species of interest, H<sub>2</sub>O, CO, and CH<sub>4</sub>. We use the analytic formulas given by Burrows & Sharp (1999), derived from chemical equilibrium arguments for CO, H<sub>2</sub>O, and H<sub>2</sub>. The result gives the mixing ratio for the molecular species as a function of temperature, which we use later during the line opacity calculation.

### 2.2.2 The Temperature-Pressure Profile in Radiative Equilibrium

Researchers who construct fully self-consistent models of atmospheric structure produce results that include not only the emergent spectrum but also the relevant parameters of the atmosphere at each layer, such as temperature, pressure, density, optical depth, etc. This requires assumptions concerning the boundary layers of the model atmosphere; for example, some have an opaque cloud deck that serves as the lower boundary, and some assume irradiation from the star as the upper boundary. The properties of each layer are usually calculated by enforcing hydrostatic equilibrium and assuming local thermodynamic equilibrium and radiative equilibrium. **Local thermodynamic equilibrium** implies that the properties of a given layer are determined solely by the temperature of that layer. **Radiative equilibrium** means that all of the energy is transported by

radiation. Applications of radiative transfer problems to stellar atmospheres are described in detail by Mihalas (1970), and many of these techniques are readily applicable to studies of brown dwarf and extrasolar planet atmospheres.

However, the fully self-consistent calculation is beyond the scope of this work. For our purposes, we want to see how different conditions in the planetary atmosphere affect the emergent spectrum. Therefore, we start with a given temperature-pressure (T-P) profile, and then continue by calculating opacities, enforcing hydrostatic equilibrium, and finally integrating the radiative transfer equation. This allows us to check a variety of models, computed under different circumstances, and look at the changes in the resulting spectrum. This is an excellent way to gain an understanding of the atmospheric physics involved, and it is extremely useful in interpreting our observational results.

We have employed a suite of T-P profiles, calculated by Sara Seager (private communication, 2003), to compute the resulting emergent spectra. The different cases are designed to test a variety of possible configurations for the atmosphere of HD 209458 b. The fiducial profiles are plotted in Figure 2.1 and described in detail in Chapter 5. We chose the fiducial models to cover as many physical situations as possible, including the cloudy and cloudless cases, as well as the assumption for redistribution of incident stellar radiation ( $f = 1$  for redistribution of the incident radiation over the entire planet and  $f = 2$  for re-emission of the incident radiation on the day side only; see description of Equation 3.16).

The Sudarsky et al. (2003) profile (dashed line) is shown in Figure 2.1 as a reference; we used their calculated flux for comparison to our observational data, as described in Chapter 5. The other T-P profiles, calculated by Sara Seager, are used as input to the spectral synthesis code to calculate emergent spectra. The first is the cloudless  $f = 1$  model (solid line) and the second is the cloudy  $f = 1$  model (dashed line), which includes cloud opacities for  $\text{MgSiO}_3$ , Fe, and  $\text{Al}_2\text{O}_3$ .

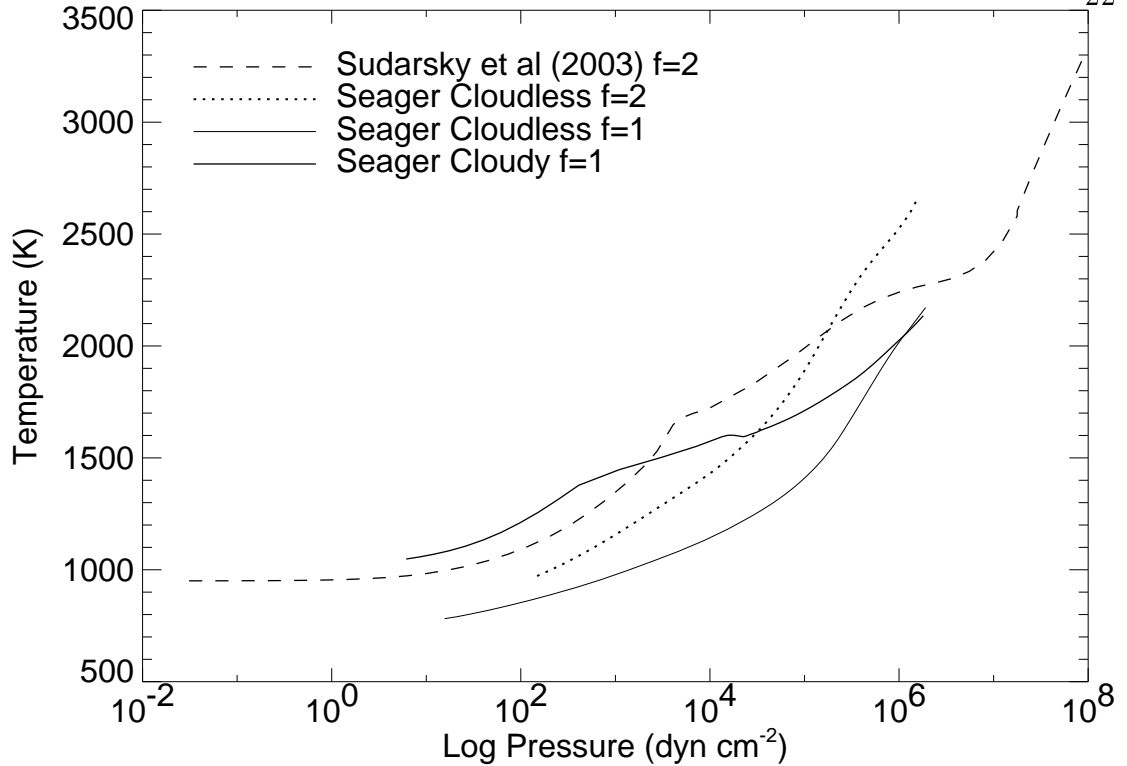


Figure 2.1: Fiducial temperature-pressure profiles used in the spectral synthesis routine. The Sudarsky et al. (2003) profile is shown as a dashed line. The other three profiles were calculated by Sara Seager. The cloudless  $f = 1$  model is shown as a solid (lower) line, and the cloudy  $f = 1$  model is shown as a solid (upper) line. The cloudless  $f = 2$  model is shown as a dotted line.

The cloudy profile is significantly hotter than the cloudless profile. Furthermore, the ‘bump’ in the profile represents the location of the clouds; in those regions, the cloudy opacity has increased the total continuous opacity, and since more radiation is absorbed, the atmosphere is hotter there. Finally, a cloudless  $f = 2$  profile is also shown. In order to investigate different possibilities for the atmospheric structure, we have scaled the two  $f = 1$  profiles using the following prescription:

$$T'_i = T_0 + \gamma(T_i - T_0) + T_{\text{offset}}, \quad (2.38)$$

where  $T_i$  is the original temperature of layer  $i$ ,  $T_0$  is the temperature at the top layer (the boundary temperature),  $T_{\text{offset}}$  is a constant added to calculate the new

profile, and  $\gamma$  is a multiplicative factor used to change the shape of the new profile. By choosing an array of values for both  $T_{\text{offset}}$  and  $\gamma$ , we can construct a profile of essentially any shape, covering the range of plausible physical conditions for the atmosphere. We record the difference in temperature from the boundary to the level where the optical depth  $\tau$  in the center of the bandpass ( $\nu_c$ ) is unity,

$$\Delta T = T(\tau_{\nu_c}=1) - T_0. \quad (2.39)$$

Equation 2.39 provides a method of characterizing the temperature gradient of the atmosphere.

### 2.2.3 The Continuous Opacity

One of the fundamental steps in any spectral calculation is the determination of the opacity. This depth- and wavelength-dependent quantity determines the optical depth scale, as seen in Equation 2.19, and thus governs the amount of radiation transmitted and absorbed by the atmosphere. We first discuss the contribution to the opacity by continuous absorbers, and then we move on to a discussion of the effect due to spectral lines.

The model atmosphere constructed for these calculations consists only of  $\text{H}_2$  gas and He, in addition to some trace amounts of other molecular species that give rise to the line opacities. Since all the hydrogen is assumed to be in the form of hydrogen gas, there are no free electrons available for interactions, and thus, it is not necessary to include the bound-bound and bound-free states of the hydrogen ion,  $\text{H}^-$ . We consider only the effect due to collision-induced absorption (CIA) of  $\text{H}_2$  with itself and with He.

Collision-induced absorption arises from the phenomenon that a dipole moment is induced in a body of interacting molecules (Frommhold, 1993). We obtained data on CIA absorption coefficients from extensive calculations performed

by A. Borysow.<sup>1</sup> These absorption coefficients were reported in obscure units and required a conversion factor before using them in the calculation. The optical depth  $\tau$  is calculated slightly differently than shown in Equation 2.19. In this case, since the opacity results from an interaction between two molecules, the opacity and optical depth are defined slightly differently. The opacity is defined by

$$\kappa_{\text{CIA}} = n_1 n_2 \sigma_{\text{CIA}} \quad (2.40)$$

where  $n_1$  and  $n_2$  represent the number densities of the two interacting species in  $\text{cm}^{-3}$  and  $\sigma_{\text{CIA}}$  represents the Borysow absorption coefficient, which is a function of temperature and wavenumber, with the appropriately-applied conversion factor to give units of  $\text{cm}^5$ . This gives the opacity value in  $\text{cm}^{-1}$ , and we can then calculate the optical depth from

$$\tau_{\text{CIA}} = \int_z \kappa_{\text{CIA}} dz. \quad (2.41)$$

For our calculations, we included the effect of  $\text{H}_2$ - $\text{H}_2$  CIA (Borysow, 2002) and  $\text{H}_2$ -He CIA (Jørgensen et al., 2000). We obtained a grid of absorption coefficients as a function of wavenumber and temperature, and we linearly interpolated the grid to the wavenumber scale of interest at a given temperature. Using Equations 2.40 and 2.41, we then calculate the contribution to the total optical depth scale by collision-induced absorption.

### 2.2.4 Line Opacities

As described in Section 2.1.6, the presence of discrete energy transitions within a given molecular species leads to absorption and emission of photons with particular values of energy (or, equivalently, with a given wavenumber). These rotational-vibrational energy transitions reveal themselves in the spectrum

---

<sup>1</sup> <http://www.astro.ku.dk/~aborysow/programs/>

because the absorption of a particular frequency of radiation causes an increase in the overall opacity of the atmosphere at that wavelength, because all the photons at that frequency are removed and re-emitted by interactions with the gas. In our spectral calculations, we have included only the dominant absorbers for our observational wavelength region, namely water, methane, and carbon monoxide.

#### 2.2.4.1 Water

Water is the most significant absorber in the mid-infrared region of the electromagnetic spectrum. This simple molecule exhibits literally millions of discrete transitions. The accuracy of the ultimate spectral calculation depends on the completeness of the line database used in the line opacity calculation. This is especially true for water, since the transitions are highly dependent on the temperature of the gas.

For our purposes, we employ the water line list constructed by Partridge & Schwenke (1997). This extensive database contains over 300 million lines, with over 8 million between  $1.85 \mu\text{m}$  and  $2.55 \mu\text{m}$ . The theoretical calculations cover the rotational-vibrational states of water, and the results are compared with experimental data for water transitions. Because many water lines are weak and difficult to measure experimentally, the results have greatly improved the existing knowledge of water line data. We also adopt the partition function given by Partridge & Schwenke (1997).

In the interests of making this large data set more manageable, but at the same time preserving the completeness of the data set, we set a lower limit, or cutoff value, on the strength of a given line; any line below the cutoff is ignored in the subsequent calculation of the line opacity. A comparison of the resulting spectrum given different cutoff values is shown in Figure 2.2. Because the line opacity calculation requires a loop over the number of lines, the reduction of the

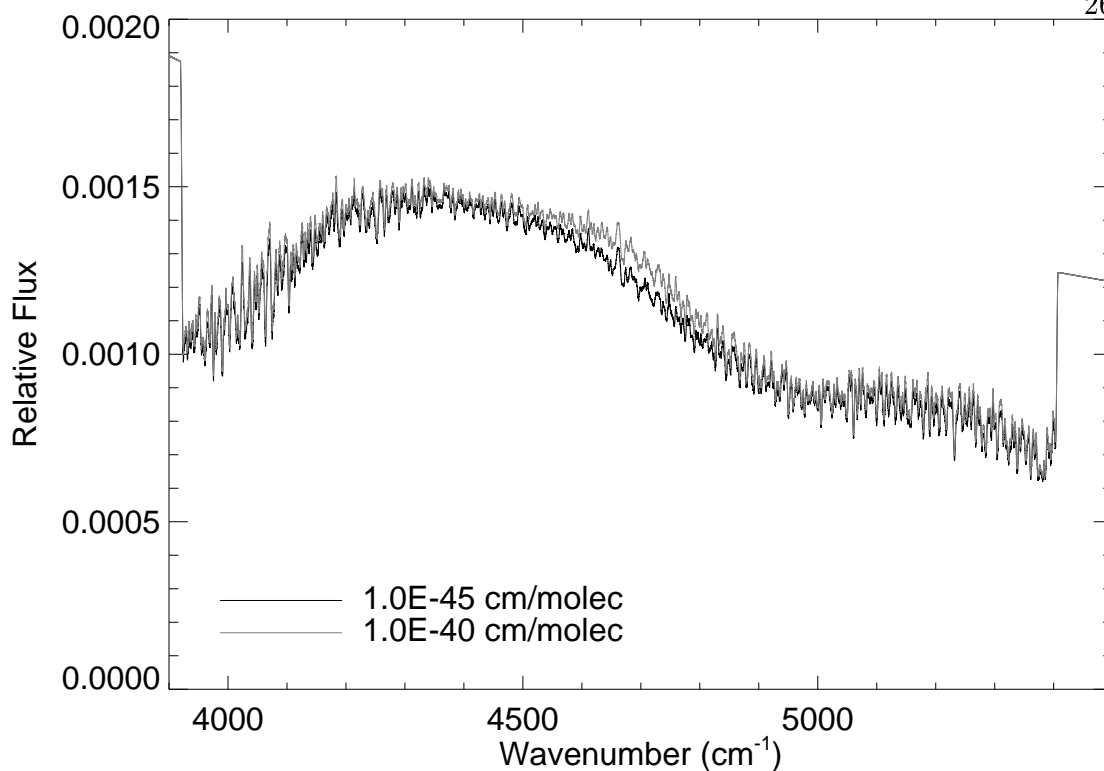


Figure 2.2: The resulting synthetic spectrum is shown for two cutoff values in line strength. The spectrum converges and this suggests that it is not necessary to include the over 8 million Partridge & Schwenke (1997) lines in this region. Cutoff values given in cm/molecule at 296 K.

number of lines needed for the calculation greatly speeds up the execution of the program. With the chosen cutoff value ( $1.0 \times 10^{-40}$  cm/molecule at 296 K), the execution time of the line opacity calculation is only about two hours; this is a great improvement over the more than ten hours required for calculating the opacity from the entire line list.

#### 2.2.4.2 Carbon Monoxide

The list of carbon monoxide lines was obtained from the HITRAN molecular absorption database (Rothman et al., 1998). The strength distribution of the line list in the relevant wavelength region is shown in Figure 2.3. We adopted

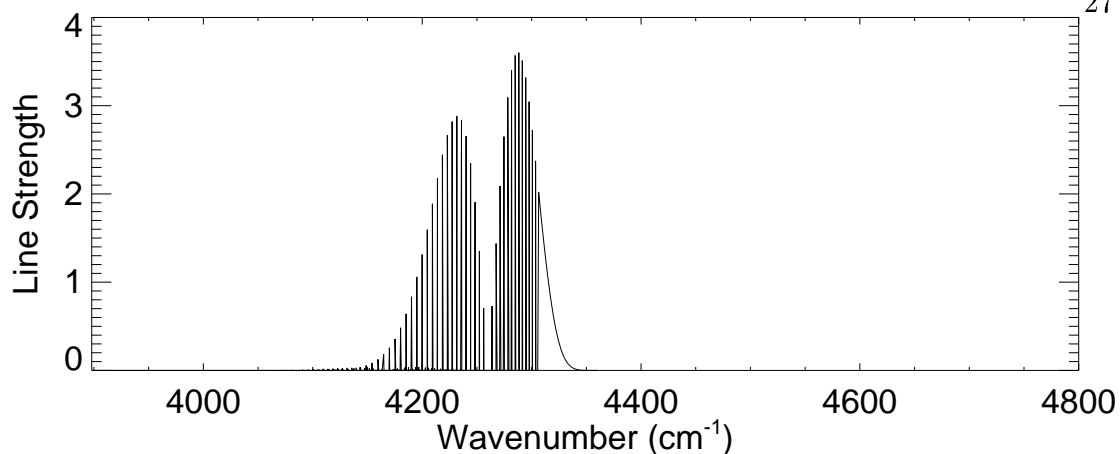


Figure 2.3: The HITRAN lines for CO in the wavelength region used for these calculations. Strength is plotted in HITRAN units of  $\text{cm}^{-1}/(\text{molecule} \cdot \text{cm}^{-2})$  at 296 K (and the values have been divided by a factor of  $10^{-21}$ ).

the analytic formula for the partition function given by Goorvitch (1994, eq. 7). CO is included in these calculations because it must be considered when calculating the thermochemical equilibrium of oxygen and carbon. Depending on the temperature, the carbon most likely appears in the form of methane or carbon monoxide.

### 2.2.4.3 Methane

Just as with CO, the methane line list was obtained from the HITRAN molecular absorption database (Rothman et al., 1998). The strength distribution for the same wavelength region is shown in Figure 2.4. Mixing ratios are calculated based on thermal equilibrium with CO based on the calculations given in Burrows & Sharp (1999). The rotational and vibrational partition functions we adopted are the same as those used by (Wiedemann et al., 2001).

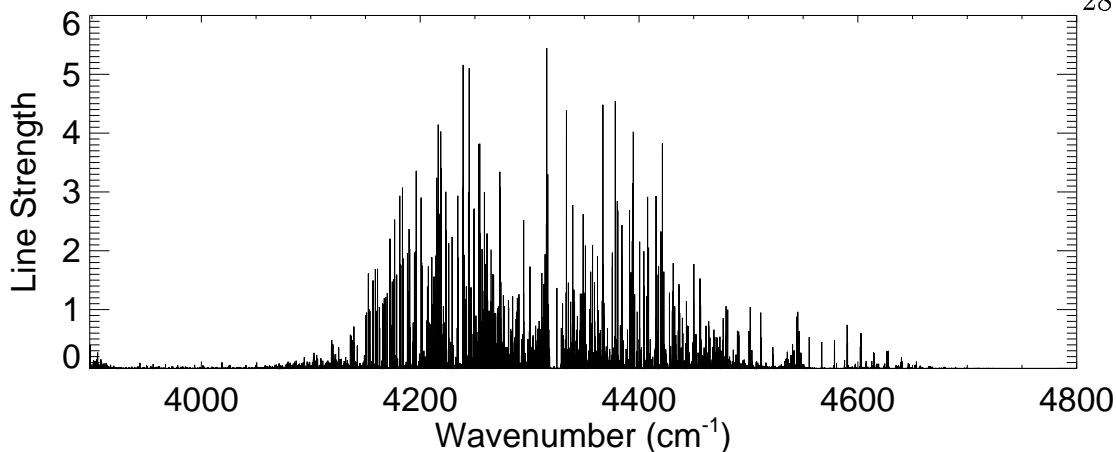


Figure 2.4: The HITRAN lines for  $\text{CH}_4$  in the wavelength region used for these calculations. As in Figure 2.3, strength is plotted in HITRAN units of  $\text{cm}^{-1}/(\text{molecule} \cdot \text{cm}^{-2})$  at 296 K (and the values have been divided by a factor of  $10^{-21}$ ).

### 2.2.5 Integration of the Radiative Transfer Equation

With the grid of continuum and line opacities determined for a given temperature profile, the only remaining step in the calculation of the planetary spectrum is the integration of the radiative transfer equation. First, the optical depth scale is determined from the opacity grids, as in Equation 2.41 for the continuum opacity and Equation 2.19 for the line opacities. By adding the contribution to the optical depth from the continuum and the lines, we calculate the optical depth scale as a function of temperature and pressure. We found that the resulting numerical integration of the transfer equation was more accurate if we interpolated onto a standard optical depth scale, regularly spaced in the logarithm of  $\tau$ . Since we have ignored scattering in these calculations, the source function is simply equal to the Planck function, and we find for the solution of Equation 2.25,

$$I_\nu(\mu) = \int_\tau B_\nu(T(\tau)) \frac{e^{-\tau/\mu}}{\mu} d\tau. \quad (2.42)$$

Finally, to calculate the emergent flux density, we use a standard IDL integration routine to calculate the integral over  $\mu$ . The flux density or irradiance is given by

$$F_\nu = \int_\mu I_\nu(\mu) \mu d\mu. \quad (2.43)$$

The  $\mu$  grid was defined from 0.1 to 1.0 in increments of 0.1.

### 2.2.6 Stellar Spectrum

Finally, we require the use of a spectrum of the parent star, HD 209458, because our data are analyzed relative to the stellar continuum. Once the planetary flux density has been calculated from the methods described above, we then simply ratio this spectrum to the stellar flux density to calculate the relative flux density. We experimented with several methods of calculating a stellar spectrum, including the simplest method of using a 6000 K blackbody, as well as the slightly more complicated case of the gray atmosphere, as described in detail by (Mihalas, 1970, Chapter 2). Ultimately, however, we opted to use a Kurucz model of HD 209458 provided to us by Sara Seager (private communication, 2003). The three cases are compared in Figure 2.5. One can see from the upper panel that the Kurucz model has small but significant deviations in shape from the blackbody calculation of the flux density. However, an integration over all wavelengths (yielding the total flux density) gives the same temperature (within a few degrees) for both cases from  $F = \sigma T^4$  (Equation 2.11).

### 2.3 Testing and Optimization of Code

In order to check that the spectral synthesis code was working properly, we used several simple cases. One of the first of these test cases was an isothermal atmosphere. In this case the source function reduces to the Planck function, and the emergent spectrum should simply look like a blackbody. For this test we removed

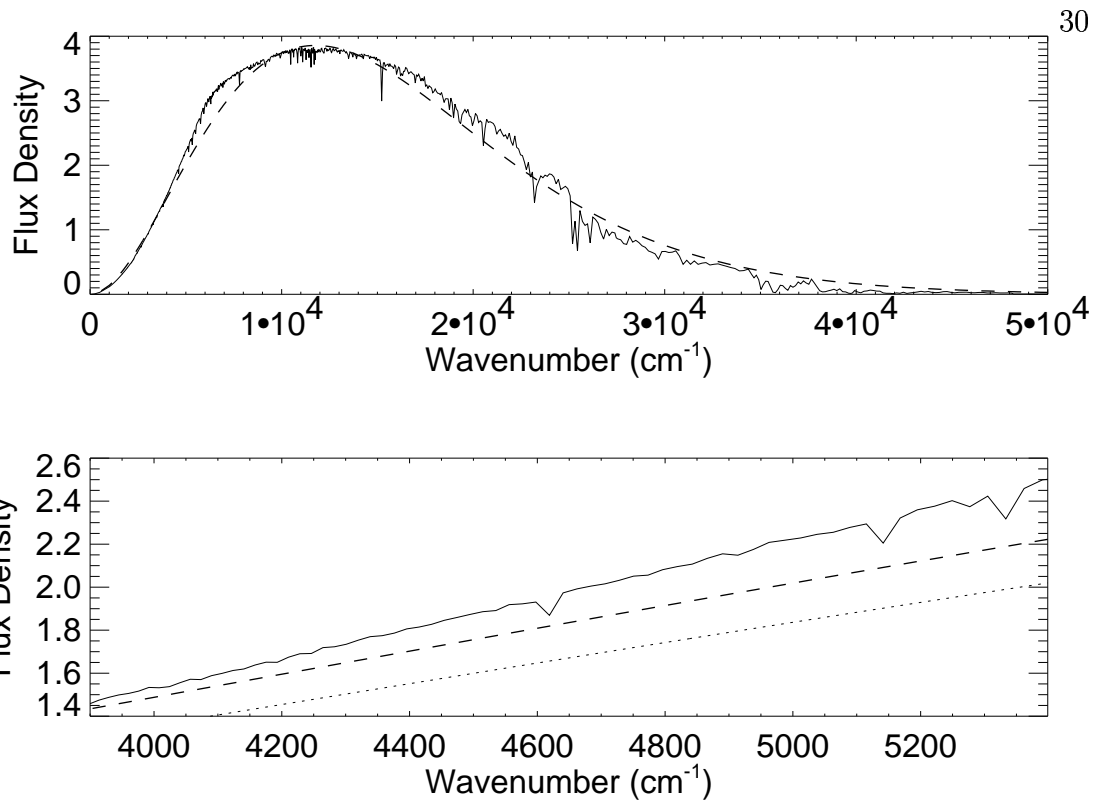


Figure 2.5: Comparison of different methods for calculating the stellar flux. Upper panel shows Kurucz model (solid line) compared to a blackbody (dashed line). Lower panel shows only the wavenumber region of interest for the IRTF data (3900 to 5400  $\text{cm}^{-1}$ ) and also indicates the stellar flux calculated from the gray atmosphere approximation (dotted line). In both panels, the units on the y-axis are  $\text{erg}/\text{cm}^2/\text{s}/\text{cm}^{-1}$ , divided by a factor of  $10^6$ .

the line opacities and clouds, and we simply replace the temperature profile with a constant value (1000 K) as a function of layer in the atmosphere. We then allow the calculation of the spectrum to proceed. The result is shown in Figure 2.6, which indicates the spectral flux density as a function of wavenumber. It is seen that the integrated planetary flux density is within 2% of the blackbody flux density for most of the range of wavenumbers shown. This agreement improves if more values of  $\mu = \cos \theta$  are included in the integration over the irradiance to calculate the flux. A similar result is obtained for the stellar flux in comparison to a 6000 K blackbody; in that case the agreement is approximately 5%.

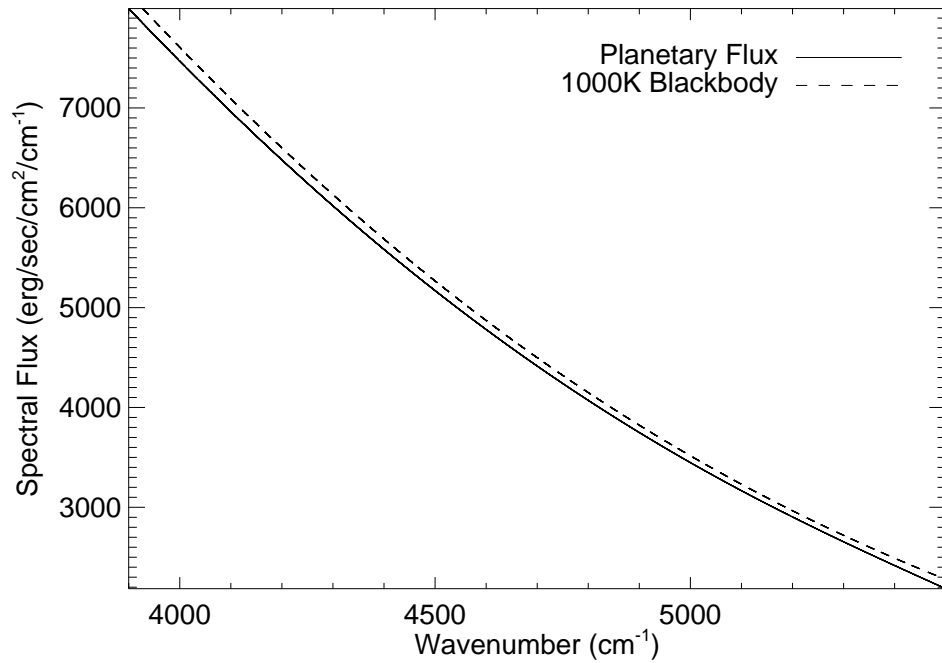


Figure 2.6: test

A further test of the isothermal case is to include the line opacities in the spectrum calculation. Since all layers in the model atmosphere have the same temperature, the temperature gradient is zero. In determining the structure of the emergent spectrum, the temperature gradient is the most important property of the atmosphere. With the gradient equal to zero, there can be no contrast from one layer to the next. That is, for a given line, each layer emits and absorbs the same amount of radiation, and therefore no line structure is observed in the emergent spectrum. We verified that even when including the line opacities, the code produces a blackbody ‘spectrum’ in the case of an isothermal atmosphere.

## 2.4 Results

A full and detailed description of the results of these calculations can be found in Chapter 5 in the context of the analysis of the IRTF data. At this point we show the results from the four fiducial cases in Figure 2.7. The Sudarsky

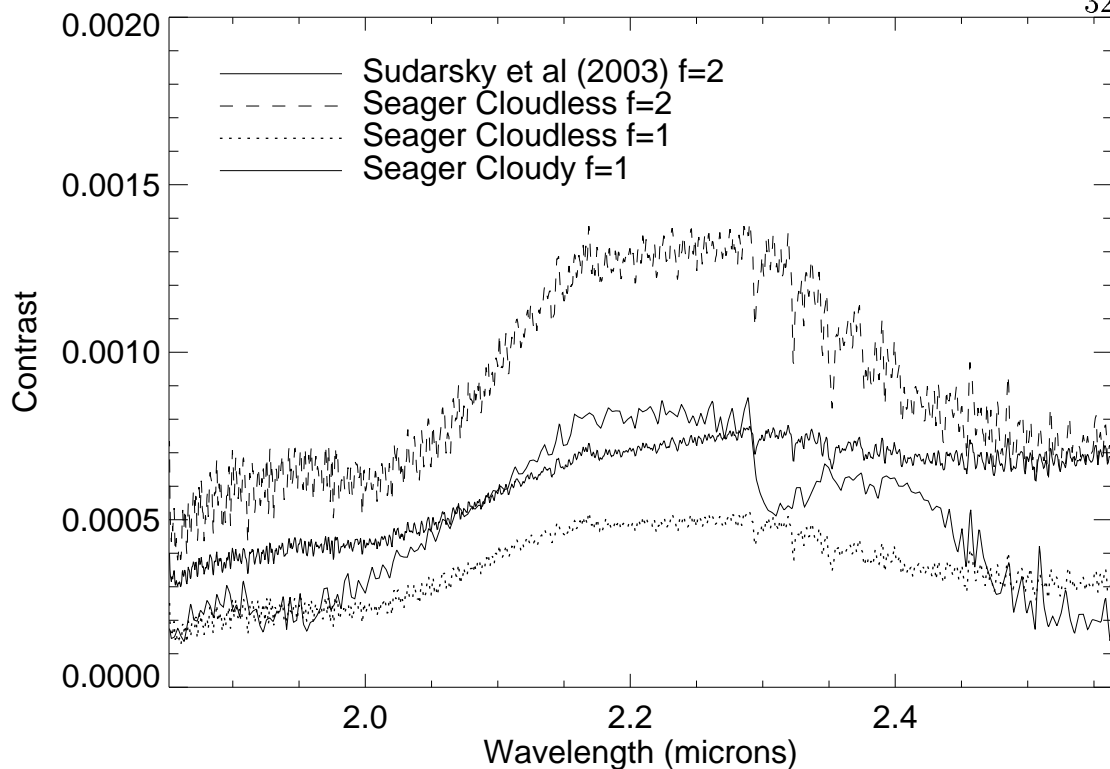


Figure 2.7: Resulting spectrum (relative to stellar flux density) for the cloudy case (thick, solid line) and the cloudless case (lower, dotted line) from the Seager temperature-pressure profiles. The cloudless  $f = 2$  result is shown as the upper dashed line. Self-consistent spectra calculated by Seager are comparable. For comparison, a spectrum calculated by Sudarsky et al. (2003) is overplotted (solid, thin line).

et al. (2003) spectrum (thin, solid line) is their calculated flux ratio divided by a model for the stellar spectrum, rather than the result from our spectral synthesis procedure. The other spectra represent the results from the spectral synthesis procedure for the three Seager profiles. The spectra calculated from the spectral synthesis procedure are comparable to the self-consistent calculations. The results from the scaled temperature-pressure profiles, based on the two  $f = 1$  fiducial profiles, are described in detail later, also in Chapter 5.

## Chapter 3

### Observational Methodology

The purpose of this chapter is to provide an introduction to the idea of occultation spectroscopy and how we have applied it to the observations of HD 209458 b. We present simple blackbody calculations that suggest the secondary eclipse is observable from the ground, given favorable observing conditions. We also present the ephemeris calculations used to select the most favorable secondary eclipse events to observe, and we summarize the observations conducted at the VLT and the IRTF.

#### 3.1 Introduction to Occultation Spectroscopy

In this section we introduce the concept of occultation spectroscopy and compare with the idea of transmission spectroscopy. By occultation spectroscopy we mean the detection of the planetary spectrum by subtracting the total (stellar and planetary) spectrum observed outside eclipse from the stellar spectrum observed during secondary eclipse, as in

$$F_p = (F_p + F_*) - F_*, \quad (3.1)$$

where  $F_p$  represents the planetary flux density and  $F_*$  represents the stellar flux density, and the dependence on wavenumber is implied. In practice, however, this is difficult to measure directly because of the variability of terrestrial atmospheric

absorption. Therefore, our approach is to determine the planetary spectrum **relative** to the stellar spectrum, as in

$$F_r = \frac{(F_p + F_*) - F_*}{F_*}. \quad (3.2)$$

This is the basic goal that forms the foundation of the observations of HD 209458 b described in Chapters 4 and 5.

Occultation spectroscopy is not a new concept to astrophysics. A very similar idea was used in observations of the Pluto-Charon system in 1987 by several researchers. In fact, observations of a series of mutual eclipse events provided the most comprehensive and precise information about these distant solar system objects. Essentially, by applying the concept captured in Equation 3.2, observers were able to record the spectrum of Pluto while it blocked its moon Charon during the eclipse (Sawyer et al., 1987). By comparing the Pluto spectrum with the total (out-of-eclipse) spectrum, the spectrum of Charon was also obtained, and the result was the identification of water ice (Buie et al., 1987). The observations led to better estimates of the geometric albedo of both objects. The difference between these observations and those described in this work is that the Pluto-Charon observations focused on reflected light, because both objects are cold. In our observations, we seek to identify direct radiation from the orbiting planet, since it is estimated to be around 1400 K, thus having significant output in the infrared.

At visible and near-infrared wavelengths, the self-emitted flux of the planet is negligible, making occultation spectroscopy of thermal emission unfavorable. However, many of the strongest molecular features of interest in extrasolar planets (e.g., the very strong fundamental  $\nu_3$  band of methane) occur at longer wavelengths. With increasing wavelength, the total signal detectable using occultation spectroscopy becomes as large, or larger, than that from transit spectroscopy.

As applied to our observations, occultation spectroscopy is essentially direct infrared spectroscopy of the extrasolar planet. In principle this could be done at most orbital phases and also for planets that do not transit. However, it requires detection of the small-amplitude planetary spectrum (the precise nature of which is unknown), superposed on a strong stellar background. The measurement becomes much easier if the signal is modulated predictably. The disappearance of the planetary spectrum during secondary eclipse is therefore an essential part of our technique. Note, however, that modulation by variations in Doppler velocity could also be used for all hot Jupiter systems, even ones without transits (Wiedemann et al., 2001).

### 3.2 Feasibility Arguments

Before we proposed the observations to detect the secondary eclipse, we did some simple calculations to determine whether the eclipse would be detectable from the ground. We describe these calculations as a motivation for our observations and analysis in subsequent chapters. As we shall see, the planetary signal is small but detectable, given good observing conditions and careful analysis.

#### 3.2.1 Blackbody Calculations

As a first approximation, one can model the planet and star as simple blackbodies, using the expression in Equation 2.10. Since we are interested in the relative energy output of the planet compared to that of the star, we define the parameter  $\alpha_\nu$  as the ratio of the Planck function for the planet and star,

$$\alpha_\nu = \frac{B_\nu(T_p)}{B_\nu(T_*)}, \quad (3.3)$$

where  $T_p$  represents the blackbody temperature of the planet and  $T_*$  represents the temperature of the parent star. Substituting Equation 2.10 yields explicitly

$$\alpha_\nu = \frac{e^{hc\nu/kT_*} - 1}{e^{hc\nu/kT_p} - 1}. \quad (3.4)$$

The quantity of interest, however, is not the radiance (represented by  $B_\nu(T)$ ), but the total flux  $f_\nu$  observed from Earth, or specifically, the ratio of the total flux for the planet relative to that of the star. As described in Section 2.1.1, the monochromatic flux density, or irradiance, is simply the integral over the hemispheric solid angle (Equation 2.5):

$$F_\nu = \int_{\Omega} I_\nu \cos \theta \, d\Omega. \quad (3.5)$$

Note that under the assumption of isotropic radiation, this equation reduces to

$$F_\nu = \pi I_\nu. \quad (3.6)$$

Finally, to calculate the total flux at a given wavenumber  $\nu$ , we integrate over area:

$$f_\nu = \int_A F_\nu dA. \quad (3.7)$$

Thus, for under the assumption of isotropic radiation and for the blackbody approximation, we have for the total flux of the star

$$f_\nu(T_*) = \pi A_* B_\nu(T_*) \quad (3.8)$$

with a similar expression for the planet.

Although the planet is so distant that it cannot be spatially resolved from the star, nonetheless there are three physical situations under which the HD 209458 system can be observed—primary eclipse, secondary eclipse, and no eclipse. To get an idea of the magnitude of the effect, consider the total flux (as given in Equation 3.8) from the system relative to the total stellar flux in each of these

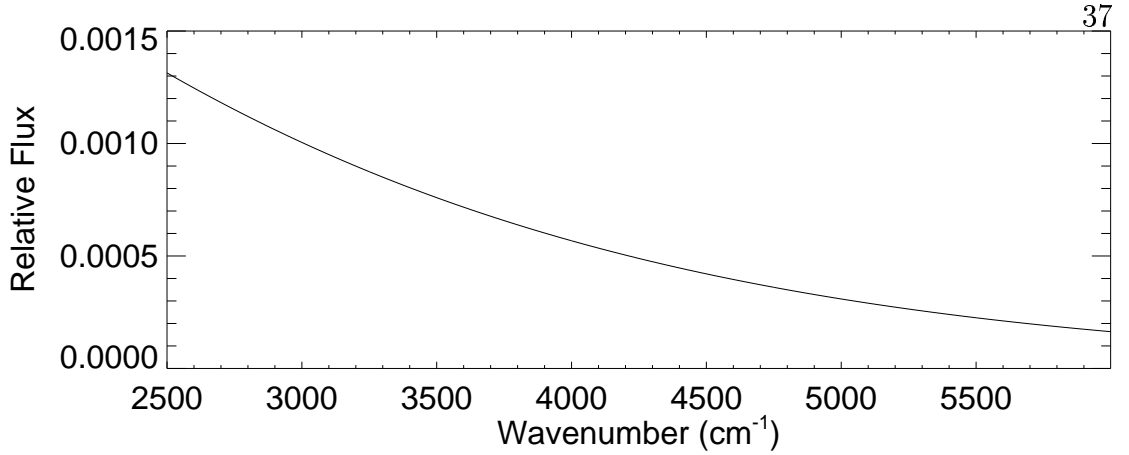


Figure 3.1: Rough estimate of the planetary flux relative to the stellar flux under the blackbody approximation. Note that the area ratio is actually a function of wavenumber, and this calculation assumes the value from the visible region.

cases. During a time of no eclipse, the total signal from the system is a sum of the stellar and planetary effects, since both are visible:

$$f_{\nu}^{(0)} = \frac{\pi B_{\nu}(T_p)A_p + \pi B_{\nu}(T_*)A_*}{\pi B_{\nu}(T_*)A_*} = 1 + \alpha_{\nu} \frac{A_p}{A_*}, \quad (3.9)$$

where  $A_p$  and  $A_*$  are the visible area (solid angle) of the planet and the star, respectively. For the primary eclipse, part of the star is blocked by the planet, so we have

$$f_{\nu}^{(1)} = \frac{\pi B_{\nu}(T_p)A_p + \pi B_{\nu}(T_*)(A_* - A_p)}{\pi B_{\nu}(T_*)A_*} = 1 + (\alpha_{\nu} - 1) \frac{A_p}{A_*}. \quad (3.10)$$

Finally, for the case of the secondary eclipse, when the planet is completely hidden, we have only

$$f_{\nu}^{(2)} = \frac{\pi B_{\nu}(T_*)A_*}{\pi B_{\nu}(T_*)A_*} = 1. \quad (3.11)$$

Evaluating these equations for  $T_p = 1500$  K,  $T_* = 6000$  K, and  $\nu = 2778$   $\text{cm}^{-1}$  ( $\lambda = 3.6$   $\mu\text{m}$ ), and using the ratio of the areas from visible measurements of the primary eclipse, we have  $f_{\nu}^{(0)} = 1.0013$ , which implies that at secondary eclipse the total flux from the system is reduced by  $\simeq 0.1\%$ . This signal is small but observable from the ground with careful measurements and good observing conditions.

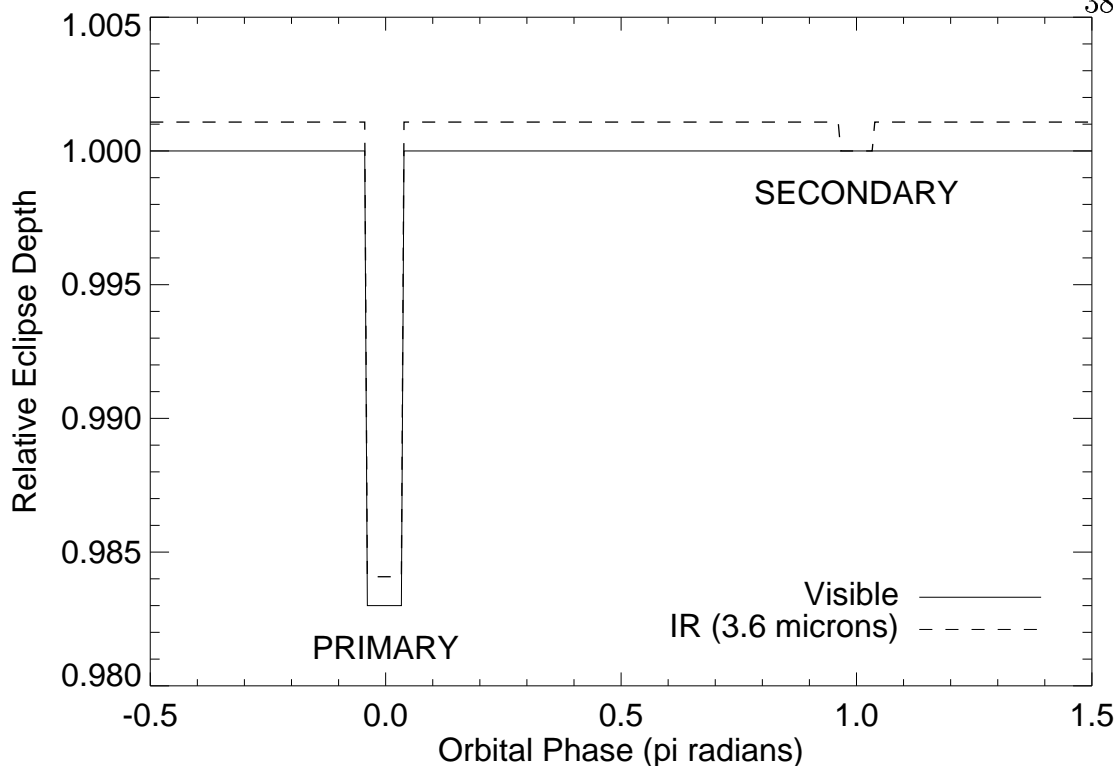


Figure 3.2: Simple calculations indicating the primary and secondary eclipses in the visible (solid line) and the infrared (dashed line).

The ratio  $\alpha_\nu \frac{A_p}{A_\star}$  is shown in Figure 3.1 for the region between 2500–6000  $\text{cm}^{-1}$ . Clearly, as expected, the detection of the planetary signal becomes more favorable for longer wavelengths. Note that this is only a rough approximation, not only because we use the blackbody assumption, but also because we have approximated the area ratio with the value from measurements in the visible region.

This result for the eclipse curve is illustrated in Figure 3.2, which shows a simple theoretical estimate of the primary and secondary eclipses in both the visible and the infrared as a function of orbital phase (where 0 marks the time when the planet is directly in front of the star and 1 represents the point when the planet is directly behind the star). The solid curve represents the eclipse in the visible; the depth of the primary eclipse is  $\sim 1.7\%$ , as determined by the initial discovery of the transit (Charbonneau et al., 2000). Based on simple blackbody

arguments, the secondary eclipse should not be observed at visible wavelengths, and indeed it is not (Charbonneau 2002, private communication). The dashed line, on the other hand, represents the eclipse curve at  $3.6 \mu\text{m}$ . In this case, as described in the equations above, the flux at time of no eclipse has increased by  $\simeq 0.1\%$  relative to the visible case. The primary eclipse has filled in relative to the visible case, but the relative depth is unchanged, since the ‘no eclipse’ level has also increased. The important difference is the secondary eclipse, which shows up at the  $0.1\%$  level.

### 3.2.2 Reflected Starlight

In this section we estimate the irradiance due to reflected starlight and compare it to the irradiance due to thermal emission. Since our goal is to detect the thermal emission of the planet, we need to check that it is not expected to be drowned out by the reflected starlight.

The expression for the irradiance due to reflected starlight is

$$F_R = AB_\nu(T_*) \left( \frac{R_*}{a} \right)^2 \quad (3.12)$$

where  $T_*$  is the blackbody temperature of the star,  $R_*$  is the stellar radius, and  $a$  is the orbital radius of the planet. The factor  $R_*/a$  appears because we must multiply the Planck function by the solid angle subtended by the star. The quantity  $A$  is the albedo, which represents the ratio of the reflected power to the incident power. Although there are more complicated definitions involving phase integrals, in a general sense, the albedo is simply the reflection coefficient. Comparatively, the irradiance due to thermal emission is simply

$$F_T = \pi B_\nu(T_{\text{eff}}) \quad (3.13)$$

where  $T_{\text{eff}}$  represents the effective temperature of the planet.

It is useful to derive an expression for  $T_{\text{eff}}$  by equating the radiant power from absorbed stellar radiation to the thermal emission. If we assume that all of the incident stellar radiation must be either reflected or absorbed, the quantity  $1 - A$  represents the fraction absorbed by the atmosphere. Thus, we can write an expression for the total radiant power absorbed by the planet's atmosphere:

$$P_A = (1 - A)\sigma T^4 \pi R_p^2 \left(\frac{R_*}{a}\right)^2. \quad (3.14)$$

Using Equation 2.11 and multiplying by the surface area of the planet, we have

$$P_T = \frac{4\pi R_p^2}{f} \sigma T_{\text{eff}}^4 \quad (3.15)$$

where  $f$  is a redistribution factor;  $f = 1$  if the incident radiation is evenly distributed and re-radiated over the surface, and  $f = 2$  if only the heated side re-radiates the incident radiation, as in an atmosphere with no energy transport mechanism (Seager & Sasselov, 1998; Guillot et al., 1996). By equating the expressions in Equations 3.15 and 3.14 we can derive an equation for the effective temperature of the planet:

$$T_{\text{eff}} = T_* [f(1 - A)]^{\frac{1}{4}} \sqrt{\frac{R_*}{2a}}. \quad (3.16)$$

Substituting the stellar and planetary parameters, we find that  $T_{\text{eff}} = 1200$  K. Now we are ready to compute the ratio of the intrinsic planetary output to the reflected stellar flux,

$$\frac{F_T}{F_R} = \frac{\pi B_\lambda(T_{\text{eff}})}{AB_\lambda(T_*) \left(\frac{R_*}{a}\right)^2}. \quad (3.17)$$

Evaluating this ratio for  $\lambda = 3.6 \mu\text{m}$  and assuming a Bond albedo of 0.5, we find that the intrinsic planetary flux density is nearly six times the reflected stellar flux density.

### 3.2.3 The Observation Limit

While the preceding arguments suggest that the flux density from the planetary internal energy source (as opposed to the stellar radiation that has been absorbed and re-radiated) is a small but detectable signal in the infrared, we now consider the important fact that the planetary flux is not expected to be well-represented as a blackbody. In the following arguments we continue to assume that the star and terrestrial atmospheric background are blackbodies. This simplifying approximation is sufficient to estimate the planetary output relative to the background noise, due to the star and terrestrial atmosphere, but we note that beyond  $3\ \mu\text{m}$  the blackbody curve is not accurate because the spectrum is dominated by terrestrial absorption lines.

The observation limit is illustrated in Figure 3.3 for the IRTF. The upper solid curve represents the total number of ‘background’ photons collected from the star and terrestrial atmospheric background calculated for a three-hour integration time, the approximate duration of the secondary eclipse. The dashed line below is the square root of the number of total background (star and atmosphere) photons collected, representing the error in the background signal. A model for the planetary spectrum, based on calculations by Adam Burrows<sup>1</sup> for HD 209458 b, is also shown. The plot indicates that the planetary spectrum is expected to be significantly above the background noise level in the region between approximately  $1$  and  $4\ \mu\text{m}$ .

Finally, we emphasize that the basic observational goal is spectroscopy of the extrasolar planet—our method will search for changes in the shape of the observed spectrum due to the presence of the planet. Note that we are not attempting to derive an absolute flux measurement of the planet.

---

<sup>1</sup> <http://zenith.as.arizona.edu/~burrows/>

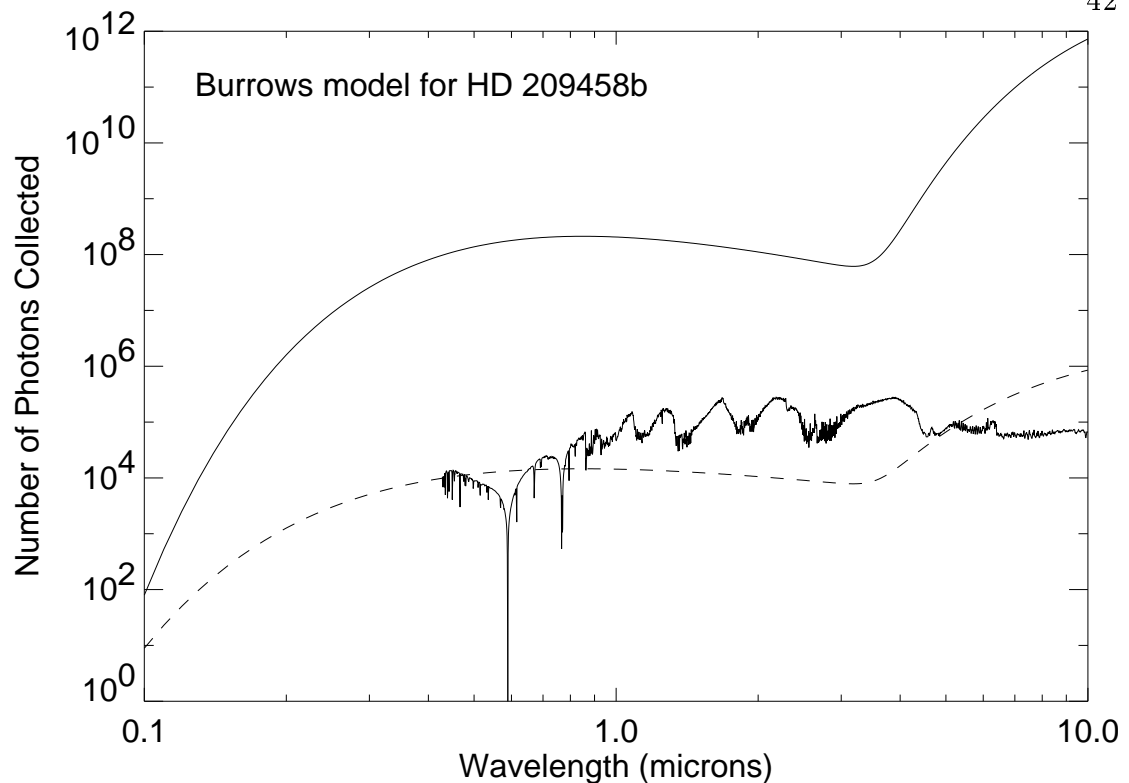


Figure 3.3: Expected number of photons collected using the 3-meter aperture of the IRTF over a 3-hour integration time (upper solid line). Spectral resolution is  $R = 1500$ , a typical value for the SpeX instrument. Model spectrum for HD 209458 b by Adam Burrows is above the photon noise limit (shown by the dashed line) over a large range of the near- and mid-infrared regions of the spectrum.

### 3.3 Infrared Astrophysics Basics

In the mid-infrared region of the spectrum, the sky emission of the Earth's atmosphere is bright, as indicated in Figure 3.3. The effect is so large that it can drown out the signal from the astronomical object one is trying to observe, and it must be removed. The common method for removing the sky background is often called **pair subtraction**. In spectroscopic modes, one typically 'nods' the telescope along the slit length (spatial dimension, perpendicular to the dispersion direction). The object is observed at two positions on the slit length,

called ‘a’ and ‘b’. If the two observations are made within a few minutes of each other, the ‘ab’ pairs can be subtracted to remove the sky background to first order, under the assumption that it has remained constant during that time. The observation sequence is typically ‘abba’, so that gradual and linear changes in the background can be removed. One advantage of spectroscopic observations is that the sky emission is recorded in the unused portions of the slit for each observation of the object of interest. We can in principle exploit this fact in making second-order corrections when the conventional pair subtraction method fails to remove the background completely. Correction of the atmospheric background to a few percent (usually achieved by the first order correction) is typically sufficient for most applications, but clearly in this case we must do better, given that the signal we are trying to detect is of order 0.1%. Thus, in instances where the first order correction clearly fails to remove the background completely, we apply the second order correction.

### 3.4 Ephemeris Calculations

In planning the observations of HD 209458, we calculated upcoming primary and secondary eclipse events by simply propagating the orbital period forward in time, given an initial time of center of primary eclipse. The calculations were performed with recent published values of  $T_c = 2452223.896173$  HJD and  $P = 3.5247542$  d, based on the measurements from the Fine Guidance Sensor (FGS) on the Hubble Space Telescope (Schultz et al., 2003). Published values of  $T_c$  are usually given in HJD (heliocentric Julian day), as are many astronomical times, so that the value is independent of the location of the Earth in its orbital path. Our calculation therefore also includes a correction for the light travel time from the Earth to the Sun, so that we can calculate the eclipse times in terms of the local time from our observing sites.

Table 3.1: Latitude, Longitude, and Altitude of VLT and IRTF.\* Offset refers to the time that must be added to a UT value to obtain the local apparent time.

Telescope	Latitude	Longitude	Altitude (m)	Offset (hr)
IRTF	19°50' N	155°28' W	4160	-10.37
VLT	24°38' S	70°24' W	2635	-4.67

\*Data from <http://www.seds.org/billa/bigeyes.html>

Next, we must find the optimum eclipse events given a particular observing location. In determining whether an eclipse is optimum, we consider the airmass effect, which is discussed in more detail later. The air mass  $x$  is defined as the inverse of the cosine of the zenith angle  $\theta$ :

$$x = \frac{1}{\cos \theta} = \frac{1}{\mu}. \quad (3.18)$$

As a celestial object moves away from the zenith, air mass increases and the observed intensity from the object decreases, since the light must travel through a longer path length of the terrestrial atmosphere, thus suffering greater extinction. The optimal case with regard to observing the eclipse is when HD 209458 reaches its zenith just as the eclipse begins or ends. In this case, the out-of-eclipse observations and the in-eclipse observations are recorded symmetrically about the zenith (corresponding to maximum intensity), which helps mitigate the air mass effect.

Practically speaking, however, it is not usually possible to select an eclipse event with such a precise location and timing. With a period of only  $\simeq 3.5$  days, an opportunity for observing an eclipse (primary or secondary) occurs approximately once per week. (Every other eclipse event will occur during the daytime and thus not be observable.) Thus, during a given observing season, only four to six eclipse events will meet the criteria to be deemed “favorable”, namely that the entire  $\sim 3$ -hour duration of the eclipse occurs while the star is visible and that the

center of the eclipse occurs within a few hours of the transit across the meridian. In order to calculate the location of the star HD 209458 at a given time, we use the well-known relation for the hour angle (HA) and right ascension (RA) of two objects:

$$\text{HA}_1 + \text{RA}_1 = \text{HA}_2 + \text{RA}_2. \quad (3.19)$$

Specifically, we need to calculate the HA of HD 209458, which represents the angular distance from the local meridian, at a given time. We use the Sun as the reference object. The RA of the Sun is tabulated, and we look up the data using WebMICA,<sup>2</sup> a website maintained by the U. S. Naval Observatory containing a wealth of astronomical data. We obtain the RA of the Sun for a range of dates at 0<sup>h</sup> UT, when the HA of the Sun is 12<sup>h</sup>. That is, 0<sup>h</sup> UT is defined as the time when the Sun is directly behind the Earth, or 12<sup>h</sup> away from the local meridian. Since the RA of the Sun changes gradually, we can assume that its value at 0<sup>h</sup> UT is approximately the same as its value at local midnight. Substituting into Equation 3.19, we have for the HA of the star

$$\text{HA}_* = \text{RA}_\odot + 12 - \text{RA}_*. \quad (3.20)$$

This equation represents the local time at which RA<sub>\*</sub> transits the local meridian. Thus, we can directly add this value (taking care to use the correct sign) to the calculated local time of center eclipse, and we find the position of the star in the sky at that time. The eclipse events are easily calculated in UT and must be converted to local time based on the observing location. The longitudes shown in Table 3.1 are used to calculate the offset from UT for that location. This offset is then added to the UT value to calculate the local apparent time.

I have written an IDL routine called `ephemeris.pro` that performs all these calculations. Results are shown in Table 3.2 for observing from the VLT during the

---

<sup>2</sup> <http://aa.usno.navy.mil/AA/data/docs/webMICA2.html>

Table 3.2: Favorable secondary eclipse events as observed from the IRTF and VLT during the summer and fall of 2001. Error in the time of center eclipse is given in seconds. The HA of the star at the time of center eclipse is also shown; a negative value implies that the star is east of the local meridian.

Location	Time of Center Eclipse (UT)	Error (s)	HA <sub>*</sub>
VLT	Sun Jul 01 05:05:46 2001	16.1	-2.97
VLT	†Sun Jul 08 06:18:09 2001	15.4	-1.28
VLT	†Sun Jul 15 07:30:37 2001	14.7	0.41
VLT	Sun Jul 22 08:37:30 2001	14.1	-1.93
IRTF	Sun Aug 12 12:09:57 2001	12.2	-0.57
IRTF	Sun Aug 19 13:22:50 2001	11.6	-0.13
VLT	Thu Aug 23 01:56:29 2001	11.3	0.09
IRTF	†Thu Sep 20 06:43:37 2001	9.3	-1.86
IRTF	†Thu Sep 27 07:57:04 2001	8.8	-0.21
IRTF	Thu Oct 04 09:04:59 2001	8.4	1.35
IRTF	Mon Nov 12 03:42:28 2001	7.4	-1.56

†Denotes an observed event.

summer of 2001 and for observing from the IRTF during the fall of 2001. Included in the table are the events we actually observed, as described in Chapters 4 and 5. As seen in the table, all the favorable events occur when the star is within 3 hours of the meridian at the time of secondary eclipse, and within 2 hours for the observed events. This routine can be used to predict future primary and secondary eclipse events for HD 209458 b, and it could even be generalized to calculate ephemerides for any object.

### 3.5 A Note on the Comparison Star

An integral part of our method to detect the signature of HD 209458 b is the use of a comparison star. The single biggest hurdle to detecting the planet from the ground is the variability of terrestrial atmospheric absorption, which is significant and happens on practically all time scales. By observing a suitable comparison star, we can remove the effect of the changing terrestrial absorption.

Table 3.3: Location, brightness and photometric colors of the three stars used in the IRTF and VLT observations. Right ascension (RA) and declination (Dec) are given in Epoch 2000.0 coordinates.

	HD 209458	HD 210483	HD 210460
RA	22 03 10.8	22 10 26.2	22 10 19.0
Dec	+18°53'04".0	+18°47'49".6	+19°36'58".8
V*	7.648	7.586	6.178
B-V*	0.594	0.585	0.706
b-y <sup>†</sup>	0.361	0.391	0.445

\*Hipparcos Catalogue (Perryman et al., 1997).

<sup>†</sup>*uvby* Photometric Catalogue (Hauck & Mermilliod, 1998)

By ‘suitable’ we mean a star that has a small angular separation from HD 209458 and is a good spectral match to HD 209458. By observing such a star within minutes of HD 209458, we can derive the relative planetary spectrum  $F_r$  from a slight modification to Equation 3.2:

$$F_r \simeq \frac{(F_p + F_*) - F_c}{F_c}, \quad (3.21)$$

where  $F_r$  represents the observed flux density of the comparison star. Note that a similar result can be obtained by returning to Equation 3.2 and substituting into the denominator the average HD 209458 spectrum when the planet is hidden. This would have the advantage of avoiding any slight variations between the stellar spectrum and the comparison spectrum. However, the advantage of the using the comparison star is that by switching frequently between the two stars, we have nearly-continuous monitoring of the variability of the terrestrial atmosphere, and this provides a method of correcting for these changes. Furthermore, the timing of the secondary eclipse is uncertain, making the determination of the average stellar spectrum more complicated.

Originally, on our first run at the IRTF in 2000, we had intended to use the star HD 210460 as the comparison star for the experiment. Later, after being

Table 3.4: Observational summary for the IRTF and the VLT in 2000 and 2001. Over 1000 individual spectra of HD 209458 were recorded.

Telescope	UT Date	Secondary Eclipse?	Number of Spectra Recorded		
			HD 209458	HD 210483	HD 210460
IRTF	17 Oct 2000	no	160	0	144
	19 Sep 2001	no	161	40	172
	20 Sep 2001	yes	319	320	0
	26 Sep 2001	no	252	192	112
	27 Sep 2001	yes	304	316	0
VLT	8 Jul 2001	yes	144	80	0
	15 Jul 2001	yes	164	96	0

awarded a second round of observing nights in 2001, we discovered that HD 210483 was a better spectral match to HD 209458. We continued to make some observations of HD 210460 during the second run, in hopes of comparison to the 2000 data. However, we were able to obtain interesting results using only HD 210483, and so the subsequent description of the analysis of the IRTF data will concentrate primarily on the use of HD 210483 as the comparison star. Information on HD 210460 is included in Tables 3.3 and 3.4 for completeness. Table 3.3 gives data concerning the location, brightness, and color indices of all three stars. (Refer to Table 4.1 for further photometric data on HD 209458 and HD 210483.)

Finally, the use of the comparison star differed for the observations at the two telescopes. At the 3-meter IRTF, slewing the telescope from HD 209458 to HD 210483 required only about 15 seconds. At the VLT, this operation required an overhead of over 6 minutes. This was obviously not well suited to track rapid variations of the terrestrial atmosphere. Therefore, for the VLT observations, we switched to the comparison star much less frequently, and we use those observations as a ‘control’ group, as described in Chapter 4.

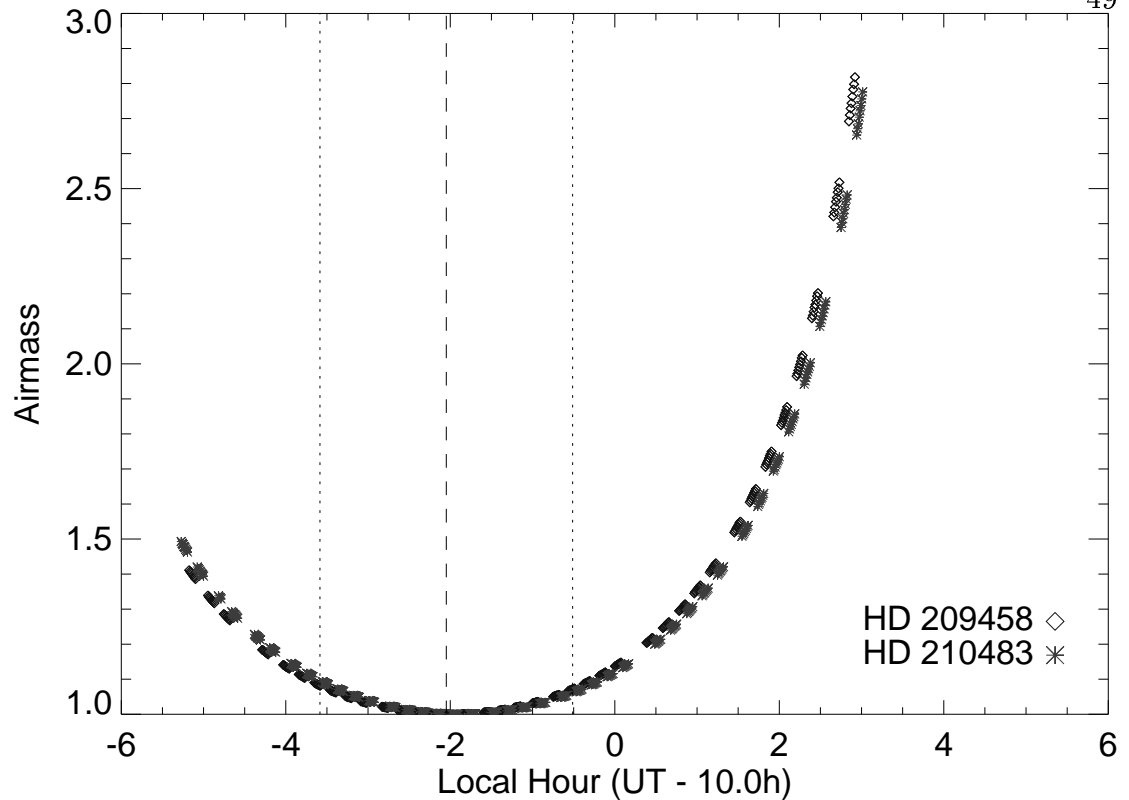


Figure 3.4: Air mass vs. Time of Observation for all spectra of HD 209458 and HD 210483 recorded on UT 27 September 2001. Predicted time of secondary eclipse (assuming the orbital eccentricity is zero) is shown by the dashed line, and boundaries of the eclipse duration are shown by the dotted lines.

### 3.6 Observational Summary

As a transition into the following chapters on the analysis of the observational data, this section provides an overview of the observations performed during the course of this project. All of the secondary eclipse events we observed are indicated in Table 3.2. We conducted observations from the NASA IRTF in September 2001, with an additional non-eclipse night in October 2000. The observations at the VLT were performed by a collaborator, Günter Wiedemann, in July 2001. A summary of these nights is shown in Table 3.4, along with the corresponding number of spectra we obtained of the main program objects.

In Figure 3.4 we show a summary of the observations of HD 209458 and HD 210483 recorded on UT 27 September 2001. This serves to bring together the concepts discussed over the course of the last few sections. The calculated eclipse and its duration are indicated, showing that HD 209458 was nearly directly overhead during the eclipse. Furthermore, it can be seen that the comparison observations are recorded at nearly the same air mass as the corresponding HD 209458 observations. At worst, the difference is approximately 0.05, occurring beyond 2.0 air masses, and furthermore, we correct for this small difference.

With an understanding of the basic purpose and methods of the observations, we are ready to proceed to the analysis and a description of the results.

## Chapter 4

### VLT Observations and Analysis

In this chapter we discuss the analysis and results of the observations of HD 209458 b recorded at the European Southern Observatory's Very Large Telescope (VLT) in July 2001. The material presented in this chapter appears as a published paper in the *Astrophysical Journal* (Richardson et al., 2003).

#### 4.1 Introduction

The discovery of the transiting extrasolar planet HD 209458 b (Charbonneau et al., 2000; Henry et al., 2000; Mazeh et al., 2000) has provided a unique opportunity to deduce the physical characteristics of one example of the so-called 'hot Jupiter' class of extrasolar planets. The transit geometry has allowed an accurate derivation of the stellar and planetary mass and radius (Brown et al., 2001b) and also provides an opportunity to measure the composition of the planet atmosphere. The scale height of an atmosphere in hydrostatic equilibrium is proportional to  $T/g$ , where  $T$  is the atmospheric temperature and  $g$  is the surface gravity. Because stellar irradiation of the planet is intense at 0.046 AU (Seager & Sasselov, 1998), the atmosphere could be as hot as  $T \sim 1400$  K or more. Coupled with the relatively low surface gravity ( $g = 848 \text{ cm s}^{-2}$ ), the atmospheric scale height is potentially as large as  $H \sim 750$  km. Moreover, when viewed tangent to the limb, the atmosphere can be opaque over several scale heights at the wavelength

of a strong absorption line. The effective absorbing area of the planet can thus be greater in a strong line by a detectable amount, producing a slightly deeper eclipse at wavelengths close to the line core (Seager & Sasselov, 2000; Brown, 2001; Hubbard et al., 2001). That is, the opacity of the planet atmosphere will impose weak, but potentially detectable, absorption lines on the stellar spectrum as the planet passes in front of the star. Several investigations attempted to detect the transmission spectrum extrasolar planetary systems (Bundy & Marcy, 2000; Moutou et al., 2001). Using the Hubble Space Telescope to observe the primary eclipse, Charbonneau et al. (2002) succeeded in detecting the sodium doublet in the atmosphere of HD 209458 b.

In addition to sodium, absorption in molecular features of water, methane, and carbon monoxide may also be observable (Hubbard et al., 2001; Brown, 2001). Brown et al. (2002) attempted to detect absorption by carbon monoxide using ground-based observations. From their attempt and our own experience, we recognize that the terrestrial atmosphere can potentially frustrate such efforts, but we believe that good observing conditions and appropriate observational and analytical techniques will enable successful measurements from the ground. The known timing of the transit (Brown et al., 2001b) is a boon to this technique, because it discriminates against false signals by providing a temporal modulation on the signal.

In this chapter we introduce a new observational approach involving the secondary eclipse, when the planet passes behind the star. The importance of the secondary eclipse was first pointed out by Charbonneau et al. (2000), but no measurement attempt has been reported in the literature. We have performed moderate resolution ‘occultation spectroscopy’ to measure the modulation (i.e., disappearance and reappearance) of the potential planetary line spectrum as the planet is hidden and revealed by the star. We have also performed lower reso-

lution spectroscopy during and near secondary eclipse using the NASA Infrared Telescope Facility (IRTF), attempting to isolate the broad infrared (IR) flux peaks from the planet's presumably hot atmosphere at wavelengths where the opacity is minimal. This paper introduces the concept of occultation spectroscopy for extrasolar planets, and reports the Very Large Telescope (VLT) spectroscopic results; lower resolution occultation spectroscopy of the IR flux peaks using the IRTF observations will be the subject of Chapter 5.

## 4.2 The Concept of Occultation Spectroscopy

In this section, we define the concept of occultation spectroscopy and briefly explain our rationale for attempting this at secondary eclipse, as opposed to more conventional transmission spectroscopy during primary eclipse. By occultation spectroscopy we mean the detection of the planetary spectrum by comparing the total (stellar and planetary) spectrum observed outside eclipse with the stellar spectrum observed during secondary eclipse.

At visible and near-infrared wavelengths, the self-emitted flux of the planet is negligible, making occultation spectroscopy of thermal emission unfavorable. However, many of the strongest molecular features of interest in extrasolar planets (e.g., the very strong fundamental  $\nu_3$  band of methane) occur at longer wavelengths. With increasing wavelength, the total signal detectable using occultation spectroscopy becomes as large, or larger, than that from transit spectroscopy. As an example, consider a spectral line having sufficient strength to be opaque  $N$  scale heights higher in the atmosphere compared to the nearby continuum when viewed tangent to the limb. Cases of interest are for large  $N$ , so we can safely assume that the line is also optically thick when viewed at normal incidence to the planetary atmosphere. Transit spectroscopy searches for this absorption against a stellar continuum flux proportional to  $\sim 2\pi RNHB_\lambda^*$ , where  $H$  is the atmospheric

scale height of the planet,  $2\pi RNH$  is the area of the annulus of the planetary atmosphere, and  $B_\lambda^*$  is the Planck function for the stellar continuum temperature at wavelength  $\lambda$ . Occultation spectroscopy, on the other hand, looks for the modulation of the planetary spectrum itself, with continuum flux proportional to  $\sim \pi R^2 B_\lambda^p$ , where  $B_\lambda^p$  is the Planck function for the planet's continuum temperature. With increasing wavelength, the increase in  $B_\lambda^p$  and the large area of the planet ( $\pi R^2$ ) dominates the area of the atmospheric annulus ( $2\pi RNH$ ) in spite of the greater stellar intensity ( $B_\lambda^*$ ). Evaluating the ratios of these fluxes for  $N = 3$ ,  $H = 750$  km,  $R = 1.0 \times 10^5$  km, and for stellar and planetary temperatures of 6000 K and 1200 K, respectively, we find that the ratio equals unity for  $\lambda = 2.6 \mu\text{m}$ . A rigorous treatment would of course include the line profiles and many other factors, but the inevitable tendency is that, for wavelengths longward of the K photometric band, occultation spectroscopy becomes increasingly favorable over transmission spectroscopy.

Occultation spectroscopy is essentially direct IR spectroscopy of the planet, and in principle this could be done at most orbital phases, and also done for planets which do not transit. However, it requires detection of the small-amplitude planetary spectrum (the precise nature of which is unknown), superposed on a strong stellar background. The measurement becomes much easier if the signal is **modulated predictably**. The disappearance of the planet spectrum during secondary eclipse is therefore an essential part of our technique. Note, however, that modulation by variations in Doppler velocity could also be used for all hot Jupiter systems, even ones without transits (Wiedemann et al., 2001). Note also that the concept of occultation spectroscopy is not new; it was successfully used to obtain the IR spectra of Pluto and its moon Charon (Sawyer et al., 1987).

Table 4.1: Stellar photometric data for both stars, including V magnitude and color and metallicity indices.

Parameter	HD 209458	HD 210483
V*	7.648	7.586
B-V*	0.594	0.585
b-y <sup>†</sup>	0.361	0.391
m <sub>1</sub> <sup>†</sup>	0.174	0.175
c <sub>1</sub> <sup>†</sup>	0.362	0.354

\*Hipparcos Catalogue (Perryman et al., 1997).

<sup>†</sup>*uvby* $\beta$  Photometric Catalogue (Hauck & Mermilliod, 1998)

### 4.3 Observational Summary

We observed two secondary eclipses, on UT 2001 July 8 and UT 2001 July 15, with the ISAAC spectrometer on the VLT (Antu) at Cerro Paranal in Chile. The observations were performed in visitor mode, with real-time decisions regarding nodding frequency, integration time, etc. Both nights were clear, with 10 – 20% relative humidity, and seeing in the range from 0.5 – 0.7 arcsec. The zenith column of precipitable water vapor, as measured from telluric water lines in our spectra, was  $\sim 6$  mm on July 8 and 1.6 mm on July 15.

ISAAC is capable of imaging and spectroscopy in the wavelength region between 1 and 5  $\mu\text{m}$  (Moorwood, 1997). We used spectroscopic mode with a resolving power of 3300, covering the 3.5 to 3.75  $\mu\text{m}$  range (2667 – 2852  $\text{cm}^{-1}$ ). Both eclipses occurred within an hour of transit across the local meridian, where the star reached a minimum airmass of 1.38. The spectra maintained good quality to the largest airmass we observed (2.51).

At approximately one half-hour intervals, we observed a comparison star, HD 210483. The comparison star is within a degree of HD 209458, with nearly the same B and V magnitudes and photometric colors (Table 4.1). We observed both stars using a conventional ‘nod’ technique, placing them alternately at ‘a’ and ‘b’

positions on the slit, in the order ‘abba’, with 60-second integrations at each slit position. On July 8 we obtained 36 ‘abba’ sets of HD 209458, and 20 ‘abba’ sets of HD 210483, while on July 15 we recorded 41 and 24 sets, respectively. About once per hour, we obtained spectra of a continuum lamp for flat-fielding. We did not rely on the standard flats; instead, we recorded flat field exposures immediately after each block of HD 209458 observations without moving the telescope or instrument, in order to avoid small but non-negligible flexure effects.

#### 4.4 Modeled Spectrum

We do not expect to achieve sufficient precision to detect the planetary spectrum in each individual spectral resolution element; instead, we look for the candidate signal by performing a least-squares fit of the observations to a model ‘template’. We computed the template as the emergent flux from a model atmosphere for the planet, using a series of specific radiance spectra at different values of  $\mu$  (the cosine of the zenith angle). These were computed from the formal integral of the radiative transfer equation, using an LTE source function; we neglected all scattering terms, since the long-wavelength region is of interest and we are assuming a cloud-free model. Flux density was computed by a quadrature integration of the radiance spectra. The spectrum synthesis was done at very high spectral resolution, and convolved to the  $0.8 \text{ cm}^{-1}$  resolution of our ISAAC data using a Gaussian instrument profile. We adopted the parameters for the star and planet given by Cody & Sasselov (2002).

Model atmospheres for the planet can vary widely, with one major difference being the treatment of clouds and aerosols. The maximum thermal contrast in IR spectra is generally obtained from clear atmospheres; one reason for this is the fact that scattering processing in clouds tend to wash out strong absorption features. We have therefore used this most optimistic case as a reference point. Our fiducial

model follows the calculation of Goukenleuque et al. (2000), with the surface gravity appropriate for HD 209458 b. This model includes irradiation by the star, but uses only gaseous opacities; condensates and particulates are assumed to have settled out of the atmosphere forming a deep cloud layer. Figure 4.1 compares the pressure/temperature structure from our fiducial model with a recent model from Sara Seager (2002, private communication). The temperature vs. optical depth structures of these models are similar, but the fiducial model requires a much higher pressure (due to lower opacity) to attain the same optical depth as the Seager model. (We also inspected a model for HD 209458 b kindly sent to us by David Sudarsky (2002, private communication); it is slightly hotter than the Seager model at all depths.)

We calculated the number densities of methane in the fiducial model, using the simple analytic formulae given by Burrows & Sharp (1999). The methane mixing ratio peaks at  $\sim 7 \times 10^{-6}$  at 25 mbar pressure, similar to the values for the 51 Peg model (Goukenleuque et al., 2000). In computing the template, we used the current best-available experimental methane line parameters from Brown, Dulick, & Devi (2001a), now incorporated into HITRAN (Rothman et al., 1998), and the calculation followed Wiedemann et al. (2001) in other respects (partition functions, etc.). Since line parameters are critical to calculation of the template, we calculated spectra of hot methane (773 K) at ISAAC resolution for laboratory conditions, using both our adopted line data and also theoretical line parameters from the spherical top data system theory (Wenger & Champion, 1998). We compared these calculated spectra to laboratory measurements of hot methane at 773 K, measured by Steyert & Reuter (2002, private communication) at the same resolution. Based on these comparisons, we have confidence in the HITRAN methane line data used to compute our model spectrum. Since our spectral region also exhibits absorption due to water, we experimented using water lines in our

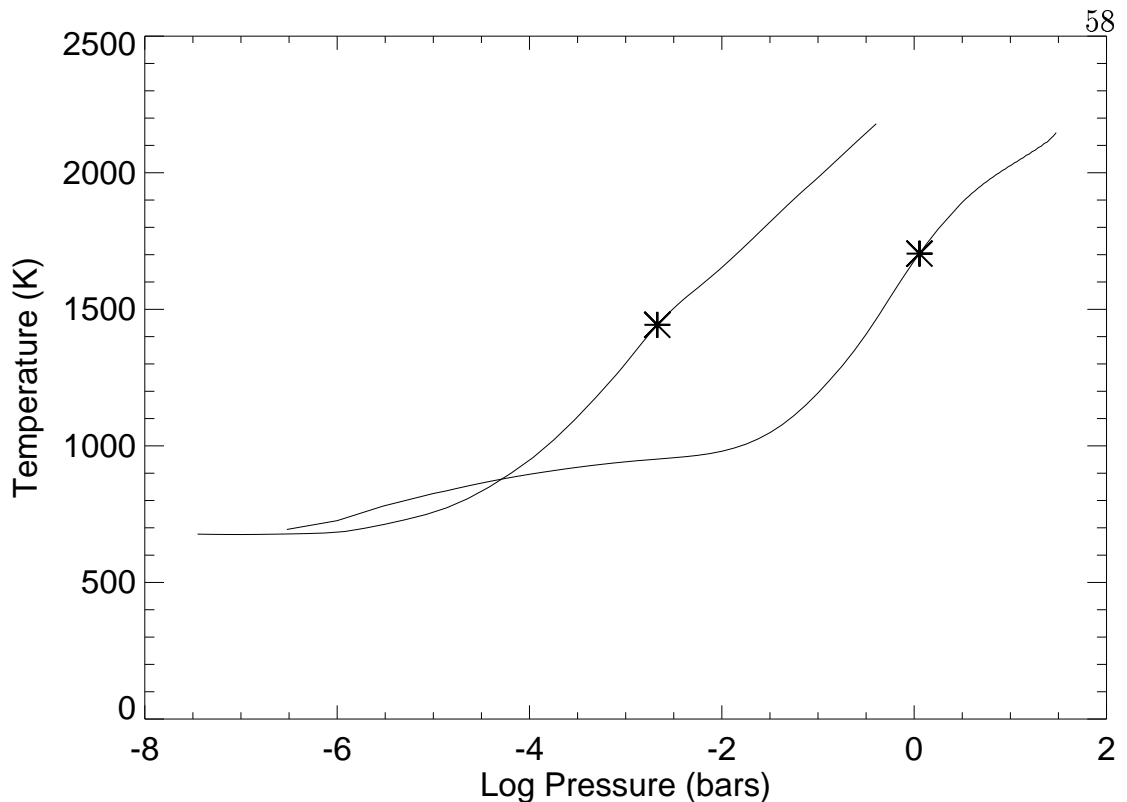


Figure 4.1: Temperature vs. pressure structure for our fiducial model for HD 209458 b (rightmost curve), and for a model by Seager (2002). The asterisks mark the points of Rosseland optical depth unity (Seager model) and  $3.6 \mu\text{m}$  optical depth unity (fiducial model).

template, also based on HITRAN. Because the HITRAN database is incomplete at high temperatures, we also experimented with using HITEMP, a HITRAN line database extension for higher temperatures, to obtain water line data. This results in abundant weak absorption lines that do not significantly change the template. We have therefore neglected water absorption in the analysis until more complete information is available for individual hot water lines in this spectral region.

We expressed the planetary flux spectrum as a ratio to the stellar flux. We computed the stellar flux from a gray atmosphere at  $T = 5800$  K, reducing the adopted 6000 K stellar temperature by 200 K to allow for the decrease in brightness temperature from the visible to  $3.6 \mu\text{m}$ , as documented for the solar

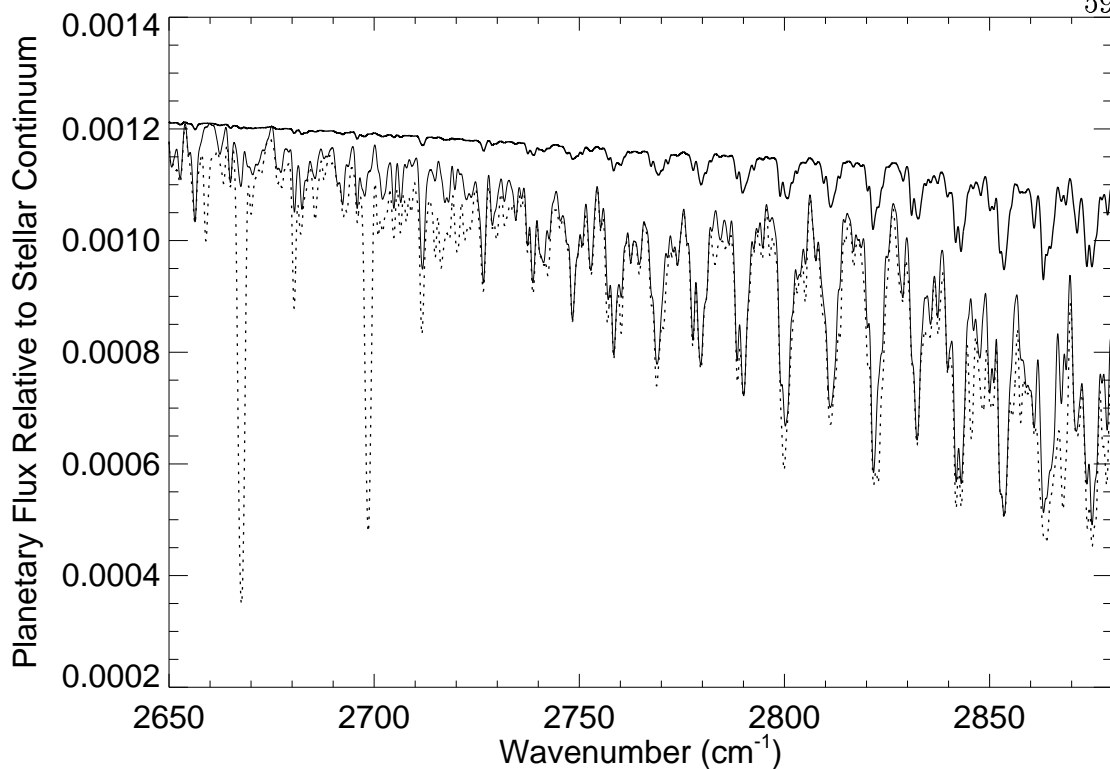


Figure 4.2: Model template spectra containing only methane lines (lower solid curve), and both methane and water lines (dotted curve). The upper solid curve represents the ‘methane only’ template with a factor of three increase in the continuous opacity, but retaining the same temperature-optical depth relation.

spectrum by Vernazza et al. (1976).

Figure 4.2 shows the modeled template spectrum, with and without water lines from HITRAN included. In the results quoted and discussed below, we have used the ‘methane only’ version of the model template, for reasons given above. However, our results and associated errors do not change significantly if ‘HITRAN water’ or ‘HITEMP water’ is included in the model template.

We computed methane spectra from models intermediate between our fiducial model and the Seager model. If we increase the continuous opacity in the fiducial model, while preserving the same temperature-optical depth relation, the methane bands weaken rapidly (again, see Figure 4.2). The greater continuous

opacity pushes all line formation to lower pressure layers, giving lower column densities ‘above the continuum.’ The mixing ratio of methane decreases at low pressures (Burrows & Sharp, 1999), further lowering the methane column density. Our fiducial model is a limiting case of an exceptionally clear atmosphere, and many other models for the planet will not exhibit significant methane features, thereby escaping the test of our present analysis.

## 4.5 Data Analysis

Analysis of the HD 209458 observations took place in four stages: 1) extraction of spectra from the 2-D data frames, 2) removal of the telluric (and the few intrinsically stellar) absorption features from the spectra, yielding residuals which potentially contain the planetary spectrum, 3) estimation of the ‘amplitude’ of the planetary spectrum in each residual spectrum, and 4) fitting of the aggregate results to a secondary eclipse curve. Since our present (and future) results depend critically on the fidelity of our data analysis, we describe this process in some detail, and we also describe checks made to insure the integrity of the analysis.

### 4.5.1 Spectral Extraction

The spectral frames were first cleaned of ‘hot pixels’ and temporary anomalies such as energetic particle events. Temporal sequences of frames at a single nod position were examined to locate hot pixels based on their variability, and these pixels were given zero weight in subsequent analysis. Energetic particle events were identified and repaired separately using a median filter applied to the temporal sequence. The cleaned ‘abba’ set was combined by adding the ‘a’ frames and subtracting the ‘b’ frames to produce a difference image, which was then divided by a flat-field frame. The flat-field frame was computed as an average of the individual flats during the night. We verified that temporal variations in the

flats were negligible for purposes of our analysis.

At an excellent IR site such as Paranal, changes in the thermal background are approximately linear with time during the several minutes required to record an ‘abba’ set. Consequently, most of the background emission is removed by construction of the difference image  $a-b-b+a$ . However, we found that a second order correction was necessary to remove the background completely. We compute the residual background spectrum by summing the region between the a and b slit positions in the difference image. The relatively long slit used in ISAAC facilitates the precision of this correction by providing a 17 arcsec length of background. This residual background spectrum is subtracted from each row of the difference image prior to the extraction of the spectra. Note that our technique differs from usual IR practice, which would be to subtract the (negative) ‘b’ spectrum from the ‘a’ spectrum after their extraction from the difference image, which would automatically subtract the background to second order. However, this would not maintain separate ‘a’ and ‘b’ spectra, which we desired in order to verify that our results are independent of the position of the spectra on the detector array.

We extracted the ‘a’ and ‘b’ spectra from the difference image using the optimal extraction formalism of Horne (1986). The spatial profile needed in the optimal extraction was constructed by fitting polynomials in the intensity vs. wavelength distribution at each slit position, and then sampling these curves in the spatial direction at each wavelength. In the process of extracting the spectra, we noted that the approximate signal-to-noise ratio of each spectrum ( $\sim 200$ ) was close to the value expected based on the noise from Poisson statistics of photoelectrons from the background.

At this stage of the analysis, the spectra were separated into sets corresponding to July 8 or July 15, HD 209458 or HD 210483, and ‘a’ or ‘b’ slit positions. Each of the 8 sets was analyzed independently of the other sets. The individual

spectra in each set were shifted slightly using spline interpolation, so that the telluric absorption features were all coincident. Frequencies in wavenumber for the telluric lines were derived from high-resolution solar Fourier transform spectra (Livingston & Wallace, 1991), convolved down to the resolution of the ISAAC data. (This accounted for any blending of telluric lines, which can change their effective wavenumbers.) Wavenumbers for each point in our ISAAC spectra were derived by spline interpolation using the telluric lines as standards; the error of this procedure was  $\sim 0.1 \text{ cm}^{-1}$ , much less than the  $0.8 \text{ cm}^{-1}$  spectral resolution. A single accurate wavenumber scale was thereby inferred for all the spectra in each set. Sample spectra from both nights are shown in Figure 4.3.

#### 4.5.2 Telluric Correction

The intensities in each spectrum fluctuate due to variable losses at the ISAAC slit, as well as changes in the telluric line and continuum absorption. For each set of spectra, we made an intensity normalization, followed by a correction to remove the telluric absorption. A pseudo-continuum was used as an aid to normalization; it was determined as a spline fitted to a set of points in each spectrum having the greatest intensity in pre-determined wavenumber intervals. We then used a wavelength-independent scale factor to normalize each spectrum so that the integral intensity under the pseudo-continuum was constant for all spectra. That is, we enforce the condition that the total intensity under each pseudo-continuum is equal to the total intensity under the average pseudo-continuum; the normalization factor  $f_i$  is calculated from

$$f_i = \frac{\sum_{\lambda} \bar{c}}{\sum_{\lambda} c_i} \quad (4.1)$$

where  $\bar{c}$  represents the average pseudo-continuum,  $c_i$  represents the fitted pseudo-continuum to spectrum  $i$ , and  $f_i$  is the factor by which each spectrum  $i$  is multi-

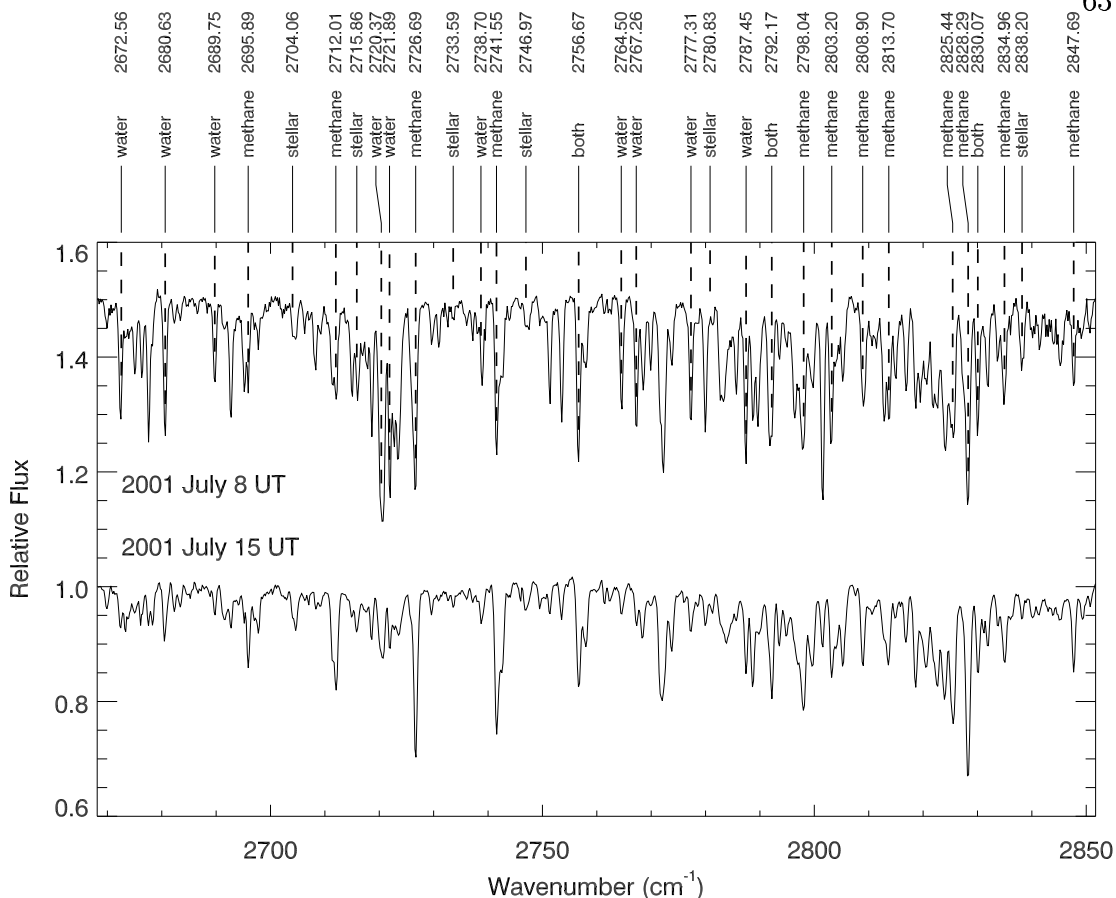


Figure 4.3: Sample spectra of HD 209458 for both observing nights. Most of the line structure is telluric, due to methane and water vapor, as noted by the line identifications. A few stellar lines are also marked (Farmer, 1989). Note that the telluric water vapor lines were stronger on 2001 July 8. The spectrum from 2001 July 8 has been shifted by +0.5 for plotting purposes.

plied. Thus, the normalized spectra are calculated by

$$n_i = f_i s_i \quad (4.2)$$

where  $n_i$  is the normalized spectrum and  $s_i$  is the original spectrum.

In the normalized spectra, at each wavelength element, we fit a least-squares line to the natural log of intensity with airmass,  $\ln n_i(x, \lambda)$ . The fitted slope  $b_\lambda$  was used to correct each intensity value to the minimum airmass in that set of spectra (this corrects for airmass-dependent telluric absorption). That is, the

airmass-corrected spectrum  $n'_i$  is obtained from

$$n'_i = \exp(\ln n_i(x, \lambda) - b_\lambda(x - x_{min})) \quad (4.3)$$

Each set of corrected spectra was then averaged. Residual spectra were calculated by subtracting the average spectrum and dividing the difference by a continuum fitted to the average spectrum. This produced residual spectra given by

$$r_i = \frac{n'_i - \bar{n}'}{c_{\bar{n}'}} \quad (4.4)$$

which presumably contain the candidate planetary signal.

It is important to note several properties of the residual spectra. Division by the pseudo-continuum of the average spectrum leaves the residuals expressed in units of the stellar continuum. But since we divided by only one continuum curve per data set, temporal changes in intensity were not masked by fluctuating errors in continuum fits. Also, the subtraction of the average spectrum means that the sum of the residuals at each wavelength is identically zero. So only variations in the spectra survive this process. In particular, the planetary spectrum will survive (since it varies due to the eclipse), but the intrinsically stellar lines (Farmer, 1989) are subtracted.

### 4.5.3 Higher-order Corrections

Several additional corrections were needed before the residuals could be compared with the model spectrum. First, we noticed that a broad absorption feature was evident in some of the residual spectra, and it corresponded to a blend of water lines near  $2720 \text{ cm}^{-1}$ . The depth of this feature was  $\sim 20\%$  relative to the stellar continuum. This indicated a change in telluric water vapor absorption from one observation to the next. To correct it, we obtained a low-noise residual water spectrum by differencing the natural logarithms of the average spectrum for

July 8 and July 15 (for both stars, and for both the ‘a’ and ‘b’ spectra, separately). This exploits the (fortuitous) fact that the precipitable water vapor column was appreciably different on the two nights, but telluric methane absorption was the same. We tested each residual spectrum to see whether a significant correlation existed with the water vapor spectrum. If it did, then we removed it from the residuals by least-squares fitting.

We also noticed that the residuals sometimes exhibit variations at low spatial frequencies (see upper panel of Figure 4.4). These baseline effects (typically  $\sim 0.2 - 0.3\%$ ) are not surprising, because our analysis treats each wavelength point independently. (We do not introduce artificial baselines - e.g., by continuum fitting - but neither do we suppress real baseline variations.) A Fourier analysis also revealed a spike of excess power at the Nyquist frequency (0.5 cycles per pixel), which is commonly seen in IR data, usually indicating a difference in the two output amplifiers reading alternate columns of the detector array. We removed these effects by computing the Fourier transform for each set of residuals; then we zeroed-out an appropriate number of low frequency elements, as well as the DC offset (zero frequency) and the Nyquist frequency components. The number of low frequencies removed (up to 0.0079 cycles per pixel) was taken to be the maximum possible without impinging on frequencies where the model planetary spectrum exhibited significant power. The same filter operations were performed on the model template spectrum as on the observed residuals. Then we inverse-transformed the filtered residuals and template, which were then suitable for comparison. The effect of this Fourier filtering on the observed residuals is seen the lower panel of Figure 4.4.

Even after the removal of variable water vapor absorption, and Fourier filtering, the residuals needed an additional correction. We discovered that they contained an excess of ‘outliers’, i.e., points more than several standard devia-

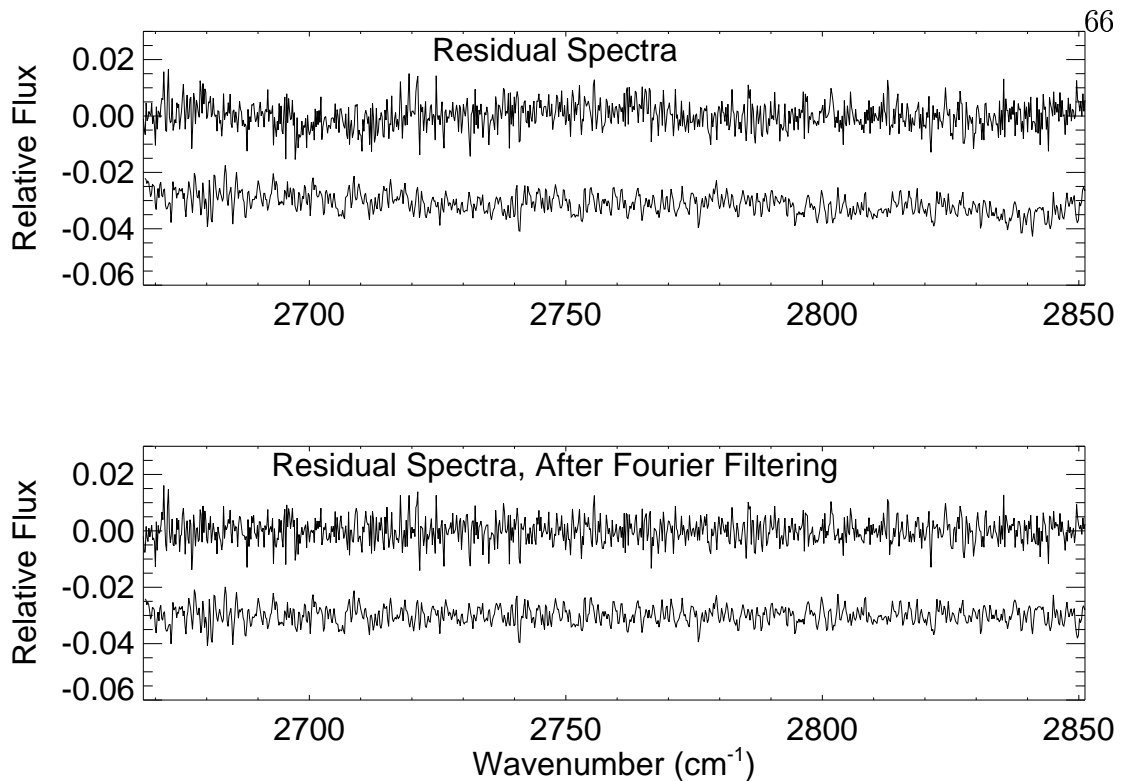


Figure 4.4: Residual spectra corresponding to the example spectra shown in Figure 4.3. Upper panel shows the residuals from the extracted spectra after telluric correction. Lower panel shows the same residuals after the Fourier filtering process. The residual spectrum from July 15 (lower curve) has been shifted by  $-0.03$  in both panels for plotting purposes.

tions from zero. We exploited our comparison star observations to find those wavelengths which tended to become outliers and reject them from the analysis. The procedure was applied to the ‘a’ and ‘b’ spectra separately, since we suspected low-amplitude ‘hot pixels’ as a likely cause of outliers. We applied a wavelength-dependent ‘weighting mask’ to the residuals, where the weight of the mask (normally unity) was set to zero when a particular wavelength was found to deviate from zero by more than  $2.5\sigma$  in two or more spectra for both HD 209458 and HD 210483. The requirement that points are zero-weighted only if that wavelength tends to be discrepant in spectra from **both** stars assures that this procedure does not bias the results. About 7% of the points were zero-weighted using

this method; we found that our final results were remarkably insensitive to the limits for the rejection. The reason for this is that the total number of outliers was much less than 7%, because a given point was always zero-weighted when it met the above criterion, even if it was ‘well-behaved’ in the majority of spectra. The standard deviation of the Fourier-filtered and masked residual spectra was in the range 0.003 to 0.006.

#### 4.5.4 Fit to the Planetary Spectrum

Prior to fitting the model template and Fourier filtering, the residuals are corrected for the heliocentric Doppler shift due to the relative motion of HD 209458 with respect to the Sun (Nidever et al., 2002), as well as the geocentric Doppler shift due to the relative motion of the Earth around the Sun. We have also corrected for the non-negligible Doppler shift due to the orbital motion of the extrasolar planet with respect to HD 209458. The residuals are shifted in wavenumber to the rest frame of the planet, and the model spectrum (already in the planet’s rest frame) is interpolated onto the same wavenumber grid. Note that although the correction is small, we have corrected each residual (each frame) for the Doppler effect, based on its time of observation. The residuals calculated for HD 210483 are analyzed in an identical manner. Although HD 210483 is not known to host a planet, we apply the same Doppler correction as we did to HD 209458, but we calculate the correction based on the time of observation of each HD 210483 residual.

The comparison between each residual spectrum and the model planetary spectrum is made using linear least-squares. For this purpose we use the ‘methane only’ version of the model (see Section 4), since the state of the spectroscopic line data gives us the most confidence in this version. (Our overall results do not change with the ‘methane plus water’ version.) The result of a least-squares

regression of the residuals vs. the model spectrum gives a quantitative estimate of the degree to which each residual spectrum ‘contains’ the model planetary spectrum. We refer to these estimates as ‘model amplitudes’, since they represent the degree to which the model spectrum appears in each residual spectrum. The least-squares fit also estimates the random error in the model amplitudes, typically 1.5 – 2.5. In other words, the signal-to-noise ratio for detecting the modeled planetary spectrum in a single set of residuals is about 0.5. This is sufficient precision to expect detection of the planetary spectrum in the average of  $\sim 50$  residual spectra, provided that the signal-to-noise ratio increases as the square root of the number of spectra averaged.

#### 4.5.5 Checks on the Analysis

We have checked our analysis procedures in several ways. Since we use linear least-squares, the analysis should have the property that averaging the best-fit model amplitudes for a set of residual spectra should give the same result as fitting to the average of those residual spectra. We verified that our results satisfy this identity exactly, if the time-variable Doppler shift applied to the residuals is neglected (with Doppler shifts included, the equality is approximate.) We have also confirmed that our numerical procedures do not attenuate potential signals. We added a synthetic signal, identical to the modeled spectrum, at the earliest practical stage of the analysis (immediately after the extraction of the spectra from the 2-D data frames). The least-squares solutions recover this signal (as a difference, out of eclipse minus in eclipse) with a best-fit model amplitude of near unity.

Another important check on our analysis is to examine the nature of the noise, specifically the distribution of noise as compared to a normal error distribution. This is important because our error estimates implicitly assume that the

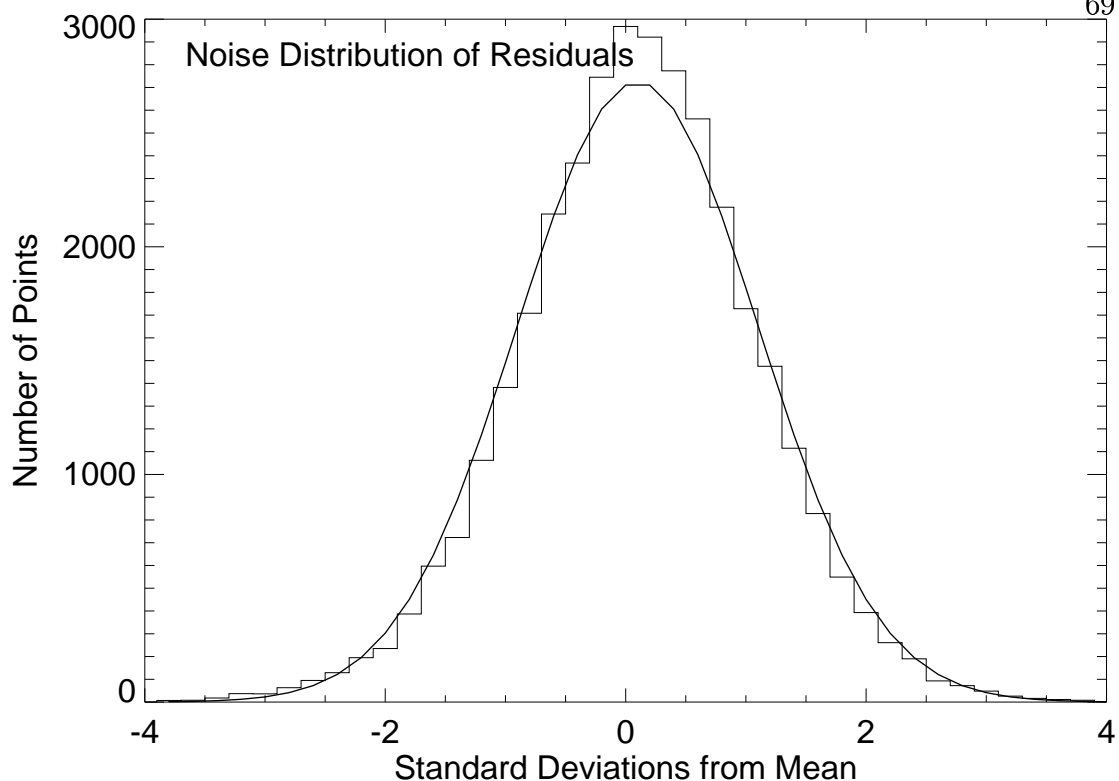


Figure 4.5: Noise distribution of the residuals for the target ‘a’ spectra on the UT 2001 July 8. Solid line indicates the theoretical value based on the Gaussian probability distribution.

data reflect a normal error distribution. Figure 4.5 shows the error distribution for all of the points (after masking) in the ‘a’ residuals of HD 209458 from July 8. Apart from an excess of points within  $1\sigma$  of zero, the distribution closely approximates a normal error curve. Similar distributions are found for the other sets of data.

Figure 4.6 shows the distribution of ‘model amplitudes.’ In this case we construct the distribution from the least-squares fits to all residual spectra for both HD 209458 and HD 210483 from both nights; this comprehensive inclusion is needed to provide sufficient points to expect a reasonable approximation to the normal error curve. Considering the number of residual spectra represented (242), the data are in good agreement with the normal error curve. As a further check

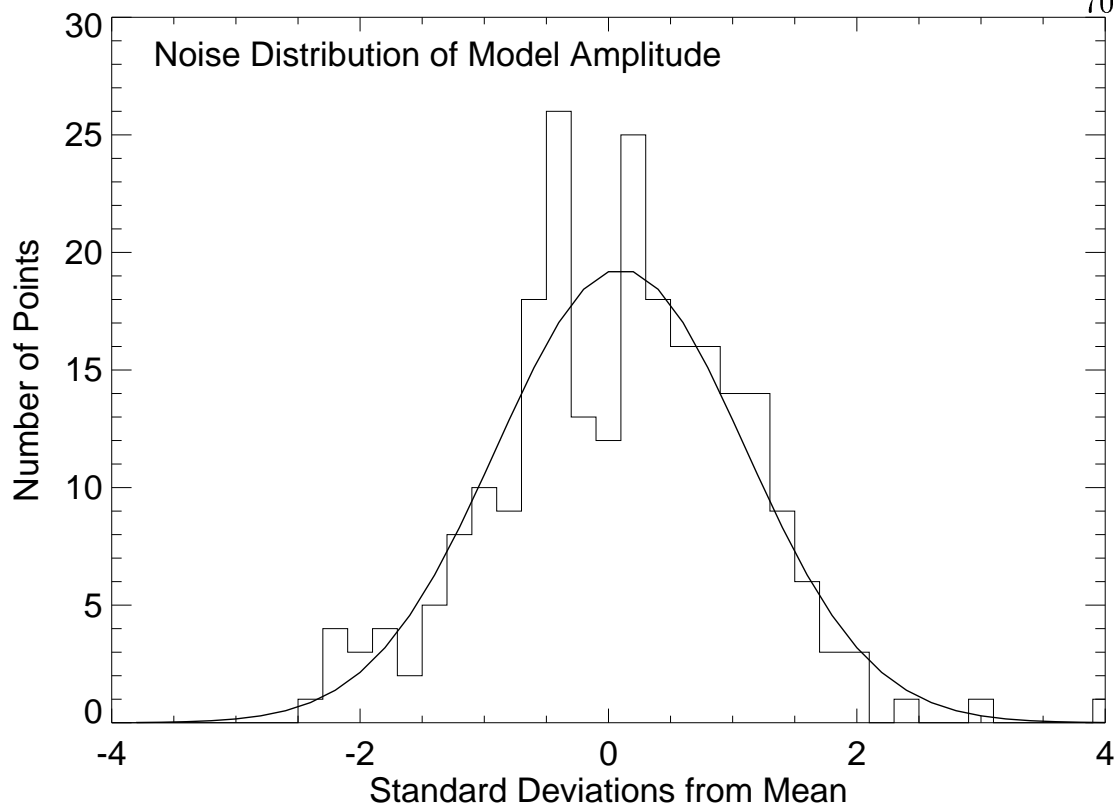


Figure 4.6: Noise distribution for computed values of model amplitude. All measurements (242) are included: both stars, both nights, and for both the ‘a’ and ‘b’ spectra. Solid line indicates the theoretical value based on the Gaussian probability distribution.

on the errors, we computed the variation in fitted model amplitudes which result from fitting Gaussian random noise whose standard deviation varied from 0.003 to 0.006, the same as the range of our filtered and masked residuals. The results of this simulation were in close agreement with the error estimates derived from the least-squares fits to the actual residual data.

#### 4.5.6 Secondary Eclipse Timing

The timing of secondary eclipse depends on the orbital eccentricity. If the eccentricity is identically zero (as might be expected based on tidal circularization arguments) the secondary eclipse will occur exactly mid-way between primary

eclipses. If the eccentricity is non-zero, it can occur up to  $\sim 90$  minutes earlier or later (depending also on  $\omega$ ). Doppler observations to date (G. W. Marcy 2002, private communication) give  $e = 0.011 \pm 0.015$  with  $\omega = 156^\circ$ , which would imply  $\delta t = -31$  minutes, i.e., a slightly earlier secondary eclipse. We computed the time of secondary eclipse as a function of the eccentricity, using  $P = 3.52474$  days (G. W. Marcy 2002, private communication), and the zero-point from primary eclipse at  $T_0 = 2451659.93675$  HJD (Brown et al., 2001b), and we corrected for light travel time. We checked our calculations against a primary eclipse ephemeris by David Charbonneau<sup>1</sup> (2002), obtaining essentially identical results, and we did a similar check for the time difference introduced by using a non-zero eccentricity (D. Charbonneau 2002, private communication). Given a calculated time for secondary eclipse, we fit a simple eclipse curve to our model amplitude data by linear least-squares. Our eclipse curve uses two levels (in- and out-of-eclipse) connected by straight lines. The time from first to fourth contact was taken to be 184.3 minutes, and from second to third contact 132.2 minutes (Charbonneau et al., 2002). Note that, due to the subtraction of an average spectrum in our data analysis, only the **amplitude** of the eclipse curve is significant; the ‘zero-point’ in the fitted eclipse curve is not meaningful.

#### 4.6 Results and Discussion

Given the precision achieved by our analysis, we would expect to detect the planetary spectrum if it is represented by the irradiated, cloudless, zero-albedo atmosphere, with thermochemical equilibrium abundances of methane (and water), and also provided that the timing of the secondary eclipse is known, and the stellar and planetary parameters (radii, etc.) are exactly as adopted. We first conclude that this precision can indeed be achieved using ground-based observations.

---

<sup>1</sup> <http://www.astro.caltech.edu/~dc/frames.html>

The recent results and discussion of Brown et al. (2002) imply the feasibility of ground-based detection, since these authors came within a factor of  $\sim 3$  of the required precision, using data for only one night in poor weather. Our experience, using a somewhat different technique, confirms that the requisite precision can be obtained if good observing conditions prevail.

Our results for the secondary eclipse are illustrated in Figures 4.7 and 4.8, showing the derived ‘model amplitudes’ for each HD 209458 spectrum (‘a’ and ‘b’ for both nights) vs. time from the assumed mid-point of secondary eclipse. Recall that the error bars for individual spectra were derived from the least-squares fits to the residuals after telluric corrections, Fourier filtering, and masking. We fit an eclipse curve to the aggregate results at each assumed eclipse time. (We fold the curve about the mid-point of secondary eclipse for the figures.) Also, there is no evidence that the results from the ‘a’ and ‘b’ spectra analyzed separately are significantly different. Figure 4.7 shows the result for  $e = 0.011$ , i.e., taking the slightly non-zero eccentricity from the Doppler data at face value, again for all spectra. The solid line is the least-squares estimate of the eclipse amplitude,  $-0.1 \pm 0.3$ , and the dashed line shows the levels corresponding to an eclipse amplitude of unity (i.e., if the model template spectrum correctly represents the planet, and the timing is correct.) Figure 4.8 shows the corresponding result ( $0.5 \pm 0.4$ ) under the assumption that the eccentricity is identically zero. In each case the reduced chi-squared of the fit is  $\sim 1.5$ , indicating that the scatter of the data is only slightly larger than the independently-assigned error bars. Note that each plot for HD 209458 is accompanied by a similar fit to the comparison star, shown in the lower panels. In both cases, the comparison star shows no significant change, as expected.

Adopting  $e = 0.01$  from the Doppler data, our results for non-detection of the secondary eclipse ( $-0.1 \pm 0.3$ ) exclude the model template spectrum at the

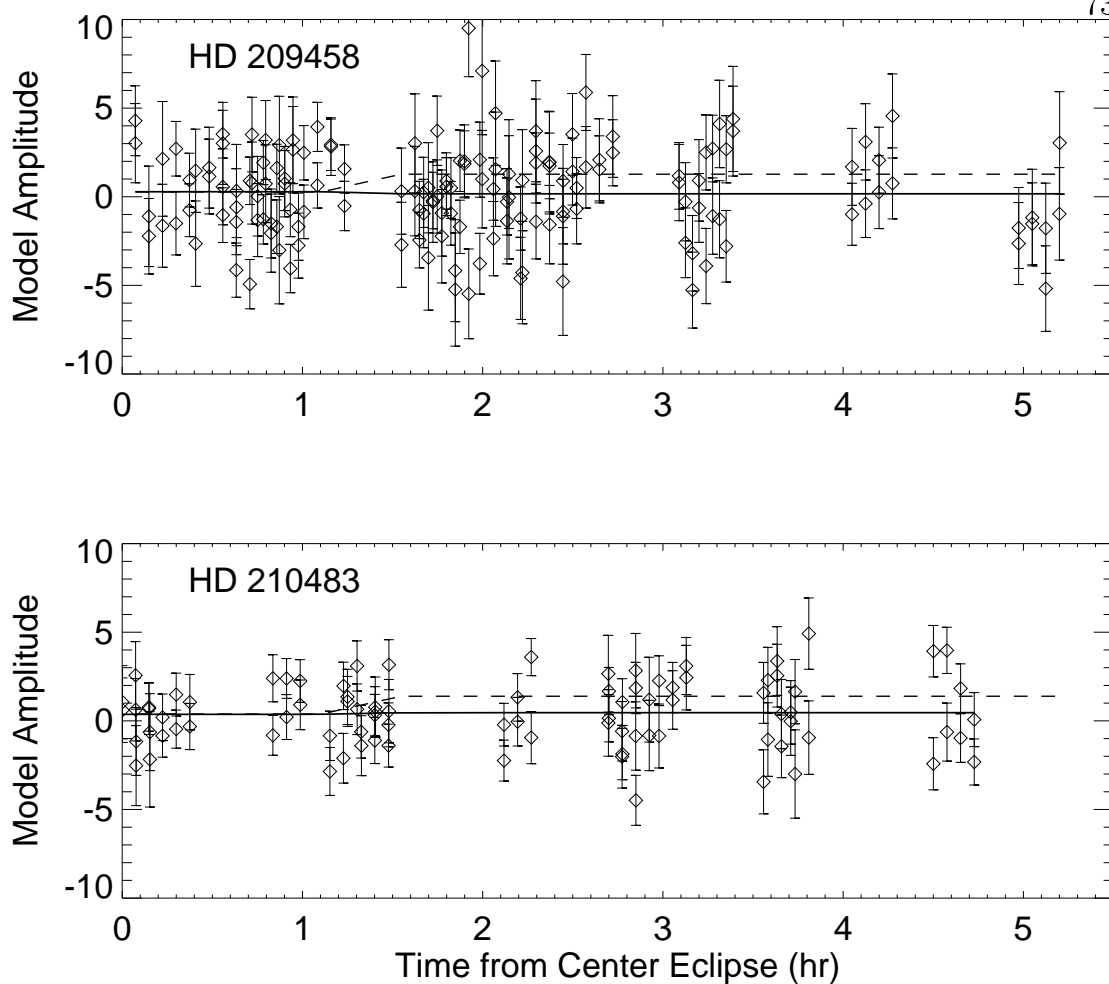


Figure 4.7: Fitted secondary eclipse curves (solid line) for HD 209458 (upper panel) and the comparison star (lower panel). These fits assume the current best-fit Doppler value of the orbital eccentricity,  $e = 0.01$ , resulting in the eclipse being 31.1 minutes earlier than that of an orbit with zero eccentricity. The dashed lines represent an eclipse amplitude of unity.

$> 3\sigma$  level. Given our error distributions, this case is firmly rejected. Assuming an eccentricity of zero, non-detection of the secondary eclipse is ambiguous ( $0.5 \pm 0.4$ ). However, even if we explore eccentricities over the entire plausible range from 0.0 to 0.03, and assume  $\omega$  values in the first and second quadrants, the fitted secondary eclipse amplitudes never reach unity. Instead, the amplitudes vary from  $-0.2$  to  $+0.9$ , and the amplitudes for the comparison star similarly range from  $-0.5$  to  $+0.9$ . At a given eclipse time, the amplitudes for the two stars are uncorrelated,

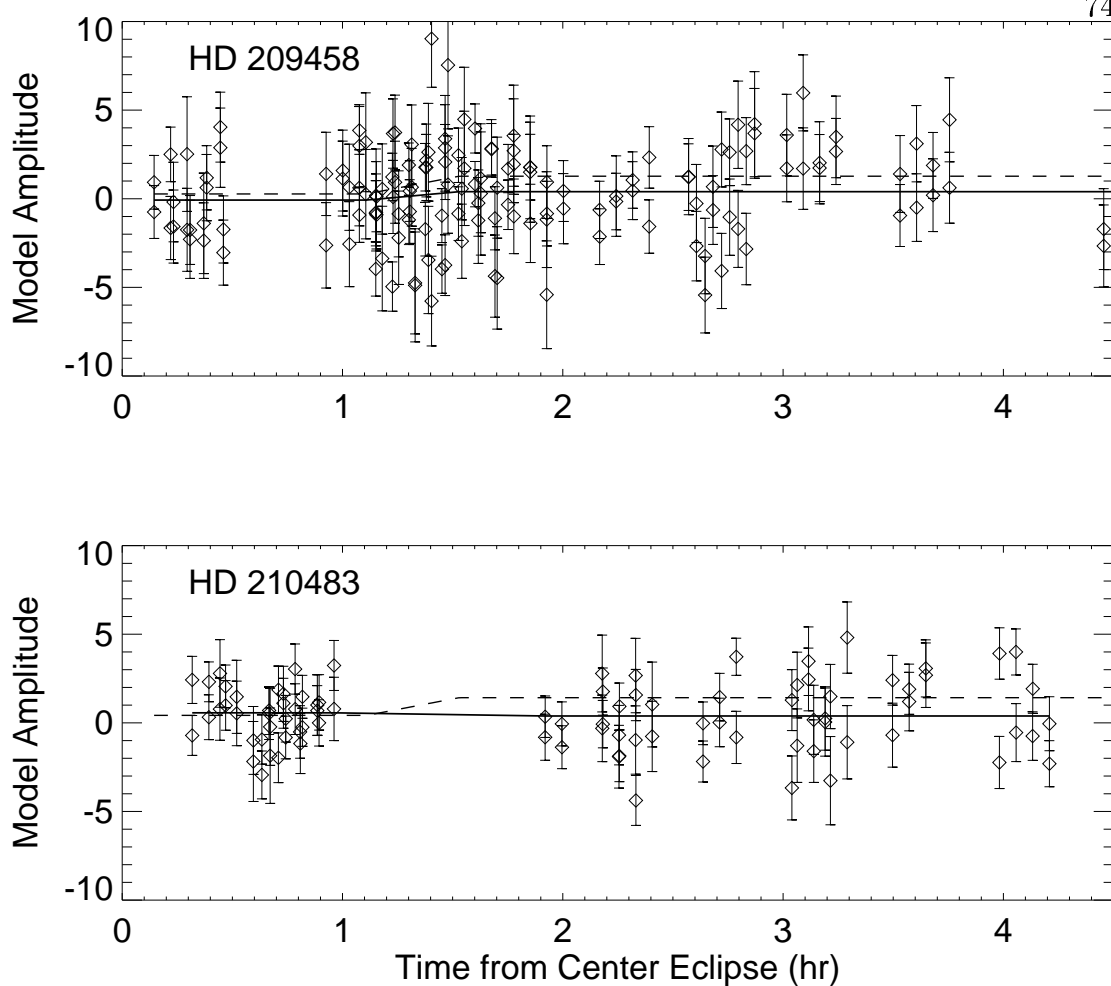


Figure 4.8: Fitted secondary eclipse curves (solid line) for HD 209458 (upper panel) and the comparison star (lower panel). These fits assume that the orbital eccentricity is zero. The dashed lines represent an eclipse amplitude of unity.

as expected when sampling the noise envelopes resulting from fitting independent random data to eclipse curves of variable timings. We therefore conclude that the secondary eclipse is not detected using our ‘methane template.’ Given the similarity between HD 209458 and the comparison star in terms of the noise envelope, and noting the nearly identical reduced chi-squared values, we conclude that HD 209458 b probably does not exhibit significant methane absorption features, in agreement with the models of Sudarsky et al. (2003). Methane absorption in the combined light spectrum (star plus planet) has a total equivalent width of no

more than  $0.025 \text{ cm}^{-1}$  within our absorption bandpass ( $2667 - 2852 \text{ cm}^{-1}$ ).

Deviation of the planetary atmosphere from our fiducial model is not difficult to explain. As discussed in Section 4, models of this planet must be exceptionally clear if significant methane absorption is to appear in their spectrum. In this respect our fiducial model represents a limiting case. Our results are certainly consistent with the suggestion of a cloudy atmosphere based on the observed low sodium abundance (Charbonneau et al., 2002). However, even in a clear atmosphere there may be other viable explanations for both the sodium result (Barman et al., 2002), and our present result (e.g., photochemical depletion of methane). Nevertheless, it is significant that we can now begin to limit the range of parameters of viable models of the planet using **ground-based** observations.

## Chapter 5

### IRTF Observations and Analysis

The material in this chapter has been submitted for publication in the *Astrophysical Journal*.

#### 5.1 Introduction

The discovery of the first transiting extrasolar planet, HD 209458 b, (Charbonneau et al., 2000; Henry et al., 2000) has led to several new observations designed to characterize the physical properties of the planet. These observations have provided a determination of the planetary and stellar radii and the true planetary mass (Brown et al., 2001b; Cody & Sasselov, 2002). Furthermore, given the geometry of the orbit, we are now beginning to learn about the structure of the planet's atmosphere. The atmosphere was first probed conclusively by Charbonneau et al. (2002), who reported a detection of the sodium doublet in transmission as the planet crossed in front of the star. Although typical models account for the strong stellar irradiation and estimate that the effective temperature of the planet is  $T \simeq 1100\text{--}1800$  K (e.g., Seager & Sasselov, 1998; Charbonneau et al., 2000), no measurements of the temperature are available from actual observations of the planet. An attempt to detect the reflected starlight from the planet during **secondary eclipse** (i.e., the time when the planet disappears behind the star) has recently been reported (Kenworthy & Hinz, 2003), but these observations

were performed in the visible region and were limited by instrumental and atmospheric effects. The infrared observations reported here have sufficient sensitivity to detect the thermal emission spectrum from the planet at the level predicted by several models for the planetary atmosphere.

In paper I (Richardson et al., 2003), we applied the method of occultation spectroscopy observations of the secondary eclipse from the Very Large Telescope (VLT), and using this technique over a narrow bandpass near  $3.6 \mu\text{m}$ , we were able to place limits on the abundance of methane in the planetary atmosphere. The most stringent limit applied only to an exceptionally clear model atmosphere, and only for certain values of the eclipse timing, which is uncertain by as much as  $\sim 30$  minutes, given the  $1\sigma$  error in the eccentricity of the orbit. In this paper, we report a further attempt to detect the secondary eclipse of HD 209458 b using the SpeX instrument at the NASA Infrared Telescope Facility (IRTF). We took a different approach for these observations; we used a broader wavelength range, in order to look for the infrared continuum of the planet near  $2.2 \mu\text{m}$ . By observing the combined light from the star and planet, we search for a change in the shape of the spectrum as the planet disappears behind the star and later reemerges. The nature of this technique makes our observations quite sensitive to the temperature gradient in the planetary atmosphere.

## 5.2 Observations

We obtained a total of four nights of data from the SpeX instrument (Rayner et al., 2003) at the NASA IRTF located on Mauna Kea in Hawaii. These are UT 19, 20, 26, and 27 September 2001, and secondary eclipse events were predicted for UT 20 and 27 September.

The SpeX instrument is a cross-dispersed echelle spectrometer capable of imaging and spectroscopy in the wavelength region between  $0.8$  and  $5.5 \mu\text{m}$  with

low to moderate spectral resolution (maximum around 2500). We operated the instrument in 1.9 to 4.2  $\mu\text{m}$  mode using the 0.5 arcsec slit, giving a spectral resolution of 1500; this mode gives nearly-continuous wavelength coverage in this region, over six orders of the echelle. The weather was excellent (low water vapor), and the seeing conditions were good—less than 1.0 arcsec on all four nights. Both eclipses occurred within an hour of the transit of the star across the local meridian, meaning that the eclipse was observed with the object directly overhead.

The use of a comparison star is an important aspect of our observation technique, and we selected HD 210483, a close spectral match to HD 209458 and nearby in the sky (see Table 1 in Paper I). The comparison star was observed immediately following each observation of the HD 209458 system. We nodded the telescope between the ‘a’ and ‘b’ positions on the slit to remove the terrestrial atmospheric background, and we recorded spectra in the sequence ‘abba.’ A given spectrum at either slit position was recorded with an integration time of 6 seconds per coadd and a total of 3 coadds; since the two objects were nearly the same visual magnitude, we used the same integration time for observing both objects. Typically we would record two successive ‘abba’ sets of HD 209458 and then switch to the comparison star for two more ‘abba’ sets, giving approximately a 50% duty cycle. It required only about 15 seconds to switch between the two stars. Over the four nights of observations, we obtained 1036 individual spectra of HD 209458 and 868 spectra of HD 210483, with a typical signal-to-noise ratio of  $\sim 100$  near 2.2  $\mu\text{m}$ . Finally, we record calibration spectra approximately once per hour. To account for flexure and other changes over the night, important for the large SpeX instrument, we record flats using an IR continuum lamp, and we record arc lamp spectra for wavelength calibration.

### 5.3 Analysis

In this section we discuss the details of the analysis process used to interpret the observations. This process consists of rejecting outlying points (or ‘hot pixels’), extracting the spectra from the raw data, and subtracting a suitable comparison spectrum to remove the telluric features. We search for changes in the resulting ‘difference spectrum’ that are synchronous with the secondary eclipse and are therefore due to the spectrum of the planet.

#### 5.3.1 Spectral Extraction

The first step in the analysis was the rejection of energetic particle events and other intermittently bad pixels from the raw data. This was accomplished using a median filter over a set of eight raw data frames, corresponding to two ‘abba’ sets.

For extracting the spectra from the raw data frames, we used the Spextool software package, written by Mike Cushing and Bill Vacca for analysis of SpeX data (Cushing et al., 2003; Vacca et al., 2003). The IDL widgets allow the user to enter an ‘ab’ pair of raw images, with the corresponding calibration files (flats and arcs). Given an individual ‘ab’ pair, the program extracts the sky background using the region of the slit between the ‘a’ and ‘b’ object positions, and removes this from the extracted ‘a’ and ‘b’ spectra. Further, it checks for the residual sky background in the pair-subtracted image, and removes it if necessary. Currently, the program outputs a standard extraction of the ‘a’ and ‘b’ spectra; that is, it performs a sum over the spatial dimension to calculate the flux at each wavelength point. Spextool also performs a wavelength calibration of the extracted spectra using the arc frames (recorded by taking an image of an Argon lamp) as well as tabulated information on telluric lines and comparing with the extracted spectra.

Finally, Spextool corrects for slight detector non-linearities in the SpeX array.

### 5.3.2 Corrections to the Extracted Spectra

The spectra of each object for a given night are first interpolated onto a constant and uniform wavelength scale. At this point we perform a second quality control check to find and correct any remaining outlying points due to uncorrected ‘hot pixels.’ For each wavelength point we perform a median filter over the time series of all values of that point for a given object during the night. A point is considered to be an outlier if the difference between the value of the point and the median value is greater than  $4\sigma$ , and it is then replaced by the median value. This process effectively removes outlying points from the spectra, but it is only necessary to correct about 0.3–0.4% of the total number of points for each object.

Next we remove from the stack any spectra that are clearly discrepant. The rejected spectra correspond in most cases to observations that were listed in our notes as questionable, either because of short-term changes in terrestrial atmospheric conditions or poor focus of the telescope. The stacks of spectra for both objects now contain only those spectra that will later be used in the calculation of the difference spectra.

With the individual spectra (again, of a given object) now interpolated onto the same wavelength scale and cleaned of outlying points, we then correct the data at each wavelength point for telluric absorption. We fit a line to the log of the intensity as a function of air mass, as described in Richardson et al. (2003, Equation 3), although in this case, we correct to air mass of unity. In order to ensure that we do not remove the effect of the planet from the HD 209458 spectra, we experimented with using the air mass correction calculated for the comparison star to correct the HD 209458 spectra. We found that this did not have a large effect on the resulting difference spectrum, showing that correcting

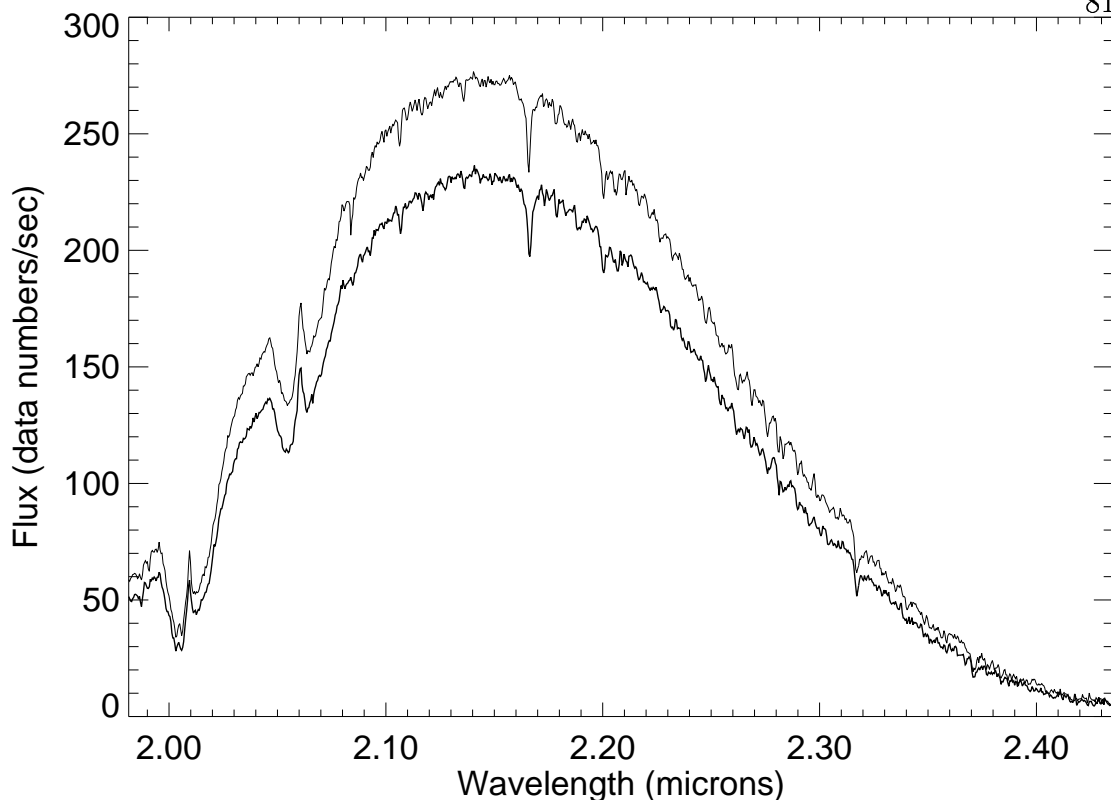


Figure 5.1: Sample extracted spectra of HD 209458 (lower, thick curve) and HD 210483 (upper, thin curve) from UT 27 September (near air mass of 1.27). The comparison star has not yet been normalized for subtraction from the HD 209458 spectrum. The overall shape of the spectra is due to the instrument response function.

the HD 209458 and HD 210483 spectra separately did not introduce a bias in the resulting residual spectrum. An example of extracted spectra (only order 4,  $\sim 2.0$ – $2.4 \mu\text{m}$ ) of HD 209458 and HD 210483 after the air mass correction is shown in Figure 5.1.

We then calculate an average air mass-corrected spectrum of each object for that particular night. By comparing the average spectra of HD 209458 and HD 210483 we can identify stellar lines; at this resolution ( $R = 1500$ ), only strong stellar lines are important. Because of the large difference in the radial velocities of the two stars,  $|\Delta v| \simeq 55.2 \text{ km s}^{-1}$  (Nidever et al., 2002; Wilson, 1953), a given

stellar line will appear at a slightly different wavelength in one star relative to the other. These show up clearly by subtracting the two average spectra. We remove them by linearly interpolating between the points on either side of the line. In comparing HD 209458 and HD 210483, we found a total of 16 stellar lines, identified as Mg and Si, as well as a single H line and a single Na line.

### 5.3.3 Difference Spectra

With the groups of spectra cleaned and adjusted for the average telluric absorption, we are now ready to consider individual spectra. First, we remove the known stellar lines from the individual spectra in the same way that they were removed from the average spectra. Note that at this point in the analysis, the two sets of spectra (corresponding to the two stars) have been extracted and interpolated onto separate wavelength scales. Next, an optimum shift value in wavelength is calculated (for both the average as well as the individual spectra separately) by minimizing the standard deviation of the difference in intensity between a target and a normalized comparison spectrum for each order separately. Using the calculated wavelength shift, we can then interpolate each comparison spectrum onto the wavelength scale of each HD 209458 spectrum. This ensures that the telluric absorption features line up in the average and individual spectra of both objects.

Next, we calculate difference spectra by comparing individual spectra of HD 209458 and HD 210483. As described, we record spectra of HD 209458, typically in groups of 8, or two ‘abba’ sets, and then switch to the comparison star. The subsequent observations of the comparison star are recorded at nearly the same air mass as those of HD 209458. We then calculate the normalized ‘differ-

ence spectrum'  $d_i$  from

$$d_i = \frac{(t_i - f_i c_i)}{g_i \bar{c}} \quad (5.1)$$

where  $t_i$  represents a single spectrum of HD 209458,  $c_i$  is the corresponding comparison star spectrum,  $f_i$  and  $g_i$  are normalization factors, and  $\bar{c}$  is the average comparison star spectrum for a given night of observations. We calculate a difference spectrum for each individual spectrum of HD 209458 by subtracting the corresponding subsequent comparison spectrum; for example, the first 'a' spectrum of HD 209458 in a given 'abba' set would be compared to the first 'a' spectrum in the subsequent comparison set. The normalization factors are used to place the comparison spectra (average and individual) on the same scale as the spectra of HD 209458. Although the two stars are nearly the same brightness, we nevertheless expect that they will not have exactly the same intensity levels, as seen in the example in Figure 5.1, due to slit losses, variable atmospheric absorption, and changes throughout the night. Both normalization factors are calculated for the entire spectrum, rather than for each order independently, to ensure that any overall slope in the planetary spectrum is not removed. The factors are computed by enforcing the condition that the total of all orders in the comparison spectrum is equal to the total of all orders in the spectrum of HD 209458, as in

$$f_i = \frac{\sum_{\lambda} t_i}{\sum_{\lambda} c_i} \quad (5.2)$$

and similarly for  $g_i$ .

This process effectively and completely removes the terrestrial absorption lines that dominate the object spectra. Furthermore, the process also has two desirable side-effects. First, it removes any time-varying changes in the detector response that may not have been corrected by the flat-fielding. Second, it removes many of the variations in the continuum and line absorption that were not corrected by the fit to air mass, because these variations may also be time-variable.

Note also that the resulting normalized difference spectrum contains the candidate planetary spectrum in flux units relative to the stellar spectrum, or the ‘contrast’ (Sudarsky et al., 2003).

### 5.3.4 Averaging over Wavelength

Once the individual difference spectra have been calculated, we then proceed to average over wavelength in order to improve the signal-to-noise ratio. We separate the spectra into sections, or ‘bins’, and average the points within each bin. The bins are defined specifically for each region, such that a bin boundary does not fall on a telluric or stellar feature. This ensures that we do not introduce a bias in the bin average. The width of each bin is therefore variable but is typically  $\sim 0.025 \mu\text{m}$ .

In looking at the series of binned difference spectra, we see that most of them exhibit an overall slope. The variation in intensity is a slowly-varying function of wavelength, amounting to typically 1–5% from 2–4  $\mu\text{m}$ ; a slight slope is evident in the example difference spectrum from UT 27 September shown in Figure 5.2. We attribute this effect to image motion on the slit due to guiding errors, coupled with the  $\lambda^{-0.2}$  wavelength dependence of seeing (Linfield et al., 2001). Our interpretation is based on three considerations: 1) the extreme slopes are clearly related to image quality, as judged by the slit losses through total intensity; 2) we constructed a simple model of the process and found that we expect to see such slopes, based on the wavelength dependence of seeing combined with guiding errors of plausible magnitude; and 3) the IRTF staff also see the effect (M. Cushing, private communication, 2002). We have investigated several methods for removing this baseline effect, but we found that our results for the short wavelength region (2–2.5  $\mu\text{m}$ ) are robust and do not change significantly based on whether a correction is made or on the details of the correction. This makes sense, given

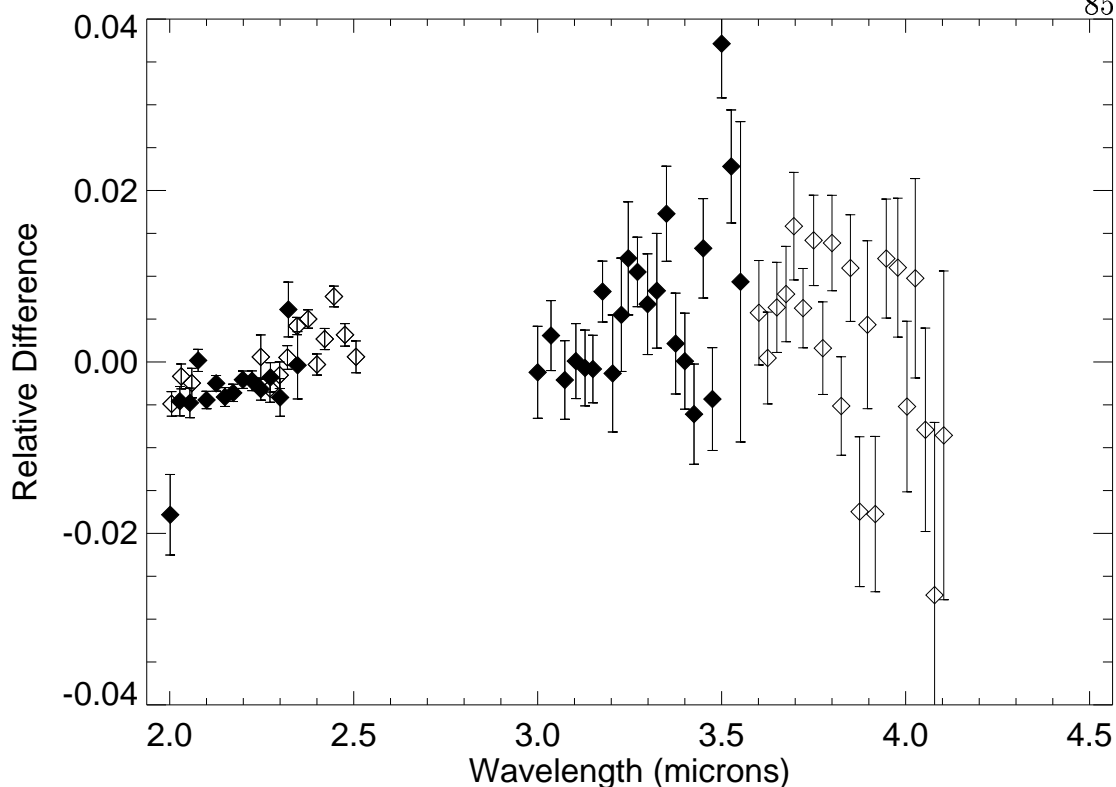


Figure 5.2: Sample binned residual spectrum from UT 27 September, corresponding to spectra shown in Figure 5.1. Five different orders from the spectrograph (three in the short wavelength region (1.9–2.5  $\mu\text{m}$ ) and two in the long wavelength region (3.0–4.1  $\mu\text{m}$ )) are shown as alternating filled and empty symbols. Because of large uncertainties resulting from the terrestrial background, the long wavelength data are not considered further in this analysis.

that the flux peak in the planetary spectrum, predicted by Sudarsky et al. (2003) and others, is a relatively sharp peak and therefore insensitive to the removal of a low-order polynomial over the entire 2–4  $\mu\text{m}$  region. We therefore present our results with no attempt to remove these gradual slopes.

Finally, the uncertainties have been carefully propagated through the entire analysis. At the beginning of the analysis, after the spectra have been extracted from the raw frames using Spextool, we calculate the noise level in each data set. (Each data set consists of a time-series of spectra of a given object for a given night of observations.) We take the error in each point to be the standard deviation

in the time series at each wavelength point independently. This error value is propagated through the calculation of the difference spectra and the wavelength binning using the standard error propagation formulae. Furthermore, we tested our analysis technique by adding a synthetic planetary signal to the data and verifying that our algorithms could extract it with the correct amplitude.

### 5.3.5 Fit to Eclipse Curve

The final step in the analysis is the comparison of the processed stack of residual difference spectra to the eclipse timing curve. The eclipse curve is calculated based on the predicted time of center of secondary eclipse (corrected for the Earth-Sun light travel time), using known values of the period and time of center eclipse from Schultz et al. (2003) ( $P = 3.5247542 \pm 0.0000044$  days and  $T_c = 2452223.896173 \pm 0.000086$  HJD) and assuming a circular orbit (eccentricity  $e = 0$ ). We also note that updated ephemeris data ( $P = 3.5247501 \pm 0.0000004$  days and  $T_c = 2452618.66888 \pm 0.00010$  HJD) is available from Wittenmyer et al. (2002). The eclipse curve is constructed in a simple way; zero represents during eclipse, unity represents out of eclipse, and we perform a linear interpolation between the ingress and egress points. Then we perform a linear least squares fit of the difference spectra to the eclipse curve, at each wavelength bin. The amplitude from the least squares fit effectively produces a final spectrum that represents the out-of-eclipse spectra minus the in-eclipse spectra, and therefore represents the candidate planetary spectrum.

Finally, we consider the possibility of a shift in the predicted time of center of secondary eclipse. The predicted times are based on the assumption of zero eccentricity, which implies that the orbit is circular and that the secondary eclipses occur exactly between primary eclipses. However, the current value of the eccentricity, calculated by Geoff Marcy and based on a single-planet fit to the Doppler

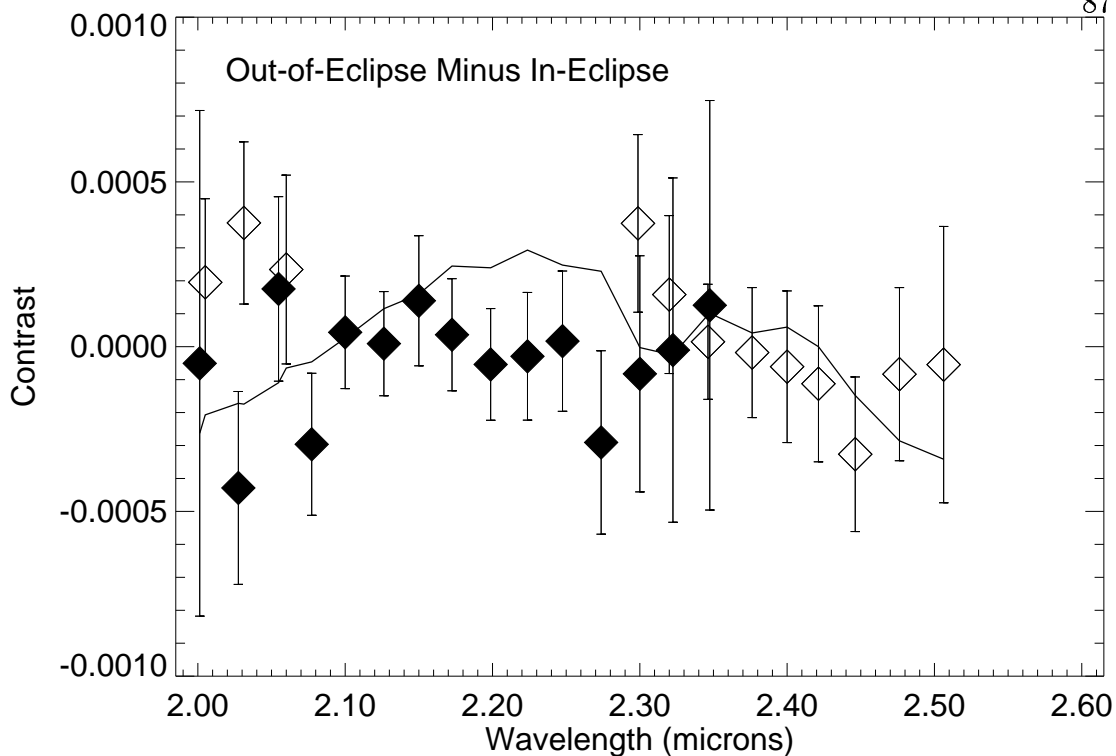


Figure 5.3: Final difference spectrum, calculated by averaging the data from the two ‘in-eclipse’ nights. This was obtained using 550 individual spectra of HD 209458, with an equal number of HD 210483 spectra. The Sudarsky et al. (2003) model is overplotted at the spectra resolution of the binned data ( $\lambda/\Delta\lambda \sim 90$ ). The offset between the model and the data is not important, since we are comparing the shapes of the two spectra. In this plot, the mean has been subtracted from the data and model, respectively.

velocity measurements, is  $e = 0.0281 \pm 0.0120$  with  $\omega = 69.78 \pm 1.2^\circ$  (G. Laughlin, private communication, 2003). If this eccentricity is taken at face value, it implies a shift in the timing of the secondary eclipse of  $\delta t = 31.4$  minutes, a slightly later eclipse. We have investigated the effect of changing the time of center eclipse by as much as 120 minutes in either direction, but we found no dramatic change in our results.

The final residual spectrum shown in Figure 5.3 represents the resulting fit to the eclipse curve, averaged for both of the in-eclipse nights, assuming zero orbital eccentricity. We show only the result for the short wavelength region (1.9–

2.5  $\mu\text{m}$ ). The larger error bars in the 3.0–4.0  $\mu\text{m}$  region (suggested by Figure 5.2) are caused by the terrestrial background and prevent a conclusive interpretation of the planetary spectrum in this region. Analysis of these long-wavelength data is continuing but is beyond the scope of this paper. Also plotted in Figure 5.3 is a model spectrum by Sudarsky et al. (2003), and we were surprised to realize that this model is excluded by our data. We pursued this idea further to see what limits could be placed on the planetary spectrum based on the residual spectrum in the short wavelength region.

We note that a flat line would be consistent with our data shown in Figure 5.3, implying that any model that does not exhibit the peak shown in the Sudarsky et al. (2003) model would escape detection in the present analysis. A flat line drawn through the data overlaps 21 of the 27 points within the individual  $1\sigma$  error bars. Note that for a normal distribution of errors, 19 of 27 points would be expected to fall within  $\pm 1\sigma$ ; therefore, our data are certainly consistent with random deviations from a flat line. Given that the details of the analysis are well understood, we are confident that a peak in the planetary spectrum is not being fortuitously canceled by some systematic error in the data. We also note that the results shown in Figure 5.3 have a slight negative curve (i.e., concave upward), but this is not statistically significant. As for comparison with the Sudarsky et al. (2003) model, the individual points are only 1 or 2  $\sigma$  from the model, but the deviations are systematic, and we exclude this model more rigorously below. In order to explore the range of models that are rejected by our data, we do some diagnostic model calculations.

#### 5.4 Model Calculations

Our model calculations are intended to help interpret the null result for the planetary spectrum in the region between 2.0–2.5  $\mu\text{m}$ . We have implemented a

simple spectral synthesis code to calculate model spectra for HD 209458 b. The algorithm consists of adopting a temperature-pressure profile and computing the emergent thermal emission spectrum. We then scale the temperature-pressure profile in an ad hoc fashion and re-compute the spectrum. Although we do not enforce radiative equilibrium when scaling the profile, the method is nonetheless consistent with our intent, which is to provide a diagnostic of the planetary atmosphere.

The three fiducial temperature-pressure profiles, described below, were used as input to the spectral synthesis code were calculated in radiative equilibrium using improvements on the method given by Seager & Sasselov (1998) and Seager et al. (2000). We devised a simple way of scaling the fiducial temperature-pressure profiles to see how these scalings changed the resulting spectrum. The prescription we used was

$$T'_i = T_i + \gamma(T_i - T_0) + T_{\text{offset}}, \quad (5.3)$$

where  $T_i$  is the temperature of layer  $i$ , and  $T_0$  is the boundary temperature, i.e., the temperature at small optical depth. Two parameters control the shape of the synthetic profile:  $\gamma$  determines the temperature gradient, or atmospheric heating, and  $T_{\text{offset}}$  is used to adjust the overall temperature of the profile. We characterize the shape of the resulting profile using the temperature at optical depth unity for  $\lambda = 2.15 \mu\text{m}$  (the center of the bandpass) and subtracting the boundary temperature:

$$\Delta T = T(\tau_{\nu_c} = 1) - T_0. \quad (5.4)$$

Armed with a temperature-pressure profile, we continue by calculating the continuous opacity due to collision-induced absorption (CIA) for  $\text{H}_2\text{-H}_2$  (Borysow, 2002) and  $\text{H}_2\text{-He}$  (Jørgensen et al., 2000). We include line opacities for  $\text{H}_2\text{O}$ ,  $\text{CO}$ , and  $\text{CH}_4$ . The water lines are taken from the extensive line database calculated

by Partridge & Schwenke (1997) and compiled by Kurucz,<sup>1</sup> the CO lines are from Goorvitch (1994), and the CH<sub>4</sub> lines were obtained from HITRAN (Rothman et al., 1998). The relative mixing ratios of the three species were determined using the simple thermochemical equilibrium formulae provided by Burrows & Sharp (1999). We then compute emergent intensity as the formal solution to the radiative transfer equation, with the source function equal to the Planck function, from

$$\mu \frac{dI_\nu}{d\tau} = I_\nu - B_\nu(T). \quad (5.5)$$

We then solve for  $I_\nu$  and calculate the flux density by integrating over  $\mu$ , as in

$$F_\nu = \int_\mu \int_\tau B_\nu(T(\tau)) e^{-\tau/\mu} d\tau d\mu. \quad (5.6)$$

Finally, we calculate the contrast ratio by dividing by a Kurucz model (Kurucz, 1992) for HD 209458. The parameters used in the Kurucz model were  $T = 6000$  K,  $\log g = 4.25$  (cgs), and  $[\text{Fe}/\text{H}] = 0.0$ , as calculated by Cody & Sasselov (2002) using the parameters in Mazeh et al. (2000).

The assumption that the source function is given by the Planck function amounts to ignoring scattering processes in the model atmosphere. Only clouds and aerosols will produce significant scattering and absorption at this wavelength. Any attempt to specify the distribution of clouds in our suite of diagnostic models would be problematic, since the structure of these models has been perturbed in an ad hoc fashion. Fortunately, the amplitude of the flux peak at this wavelength is determined primarily by the wavelength distribution of CO and H<sub>2</sub>O opacity and the temperature profile of the atmosphere.

It is useful at this point to clarify our usage of the Sudarsky et al. (2003) model. We use their tabulated flux values<sup>2</sup> for the planet, divided by the Kurucz model described above. We also multiply by the area ratio 0.016, obtained

---

<sup>1</sup> <http://kurucz.harvard.edu/molecules/h2o/>

<sup>2</sup> <http://zenith.as.arizona.edu/~burrows/>

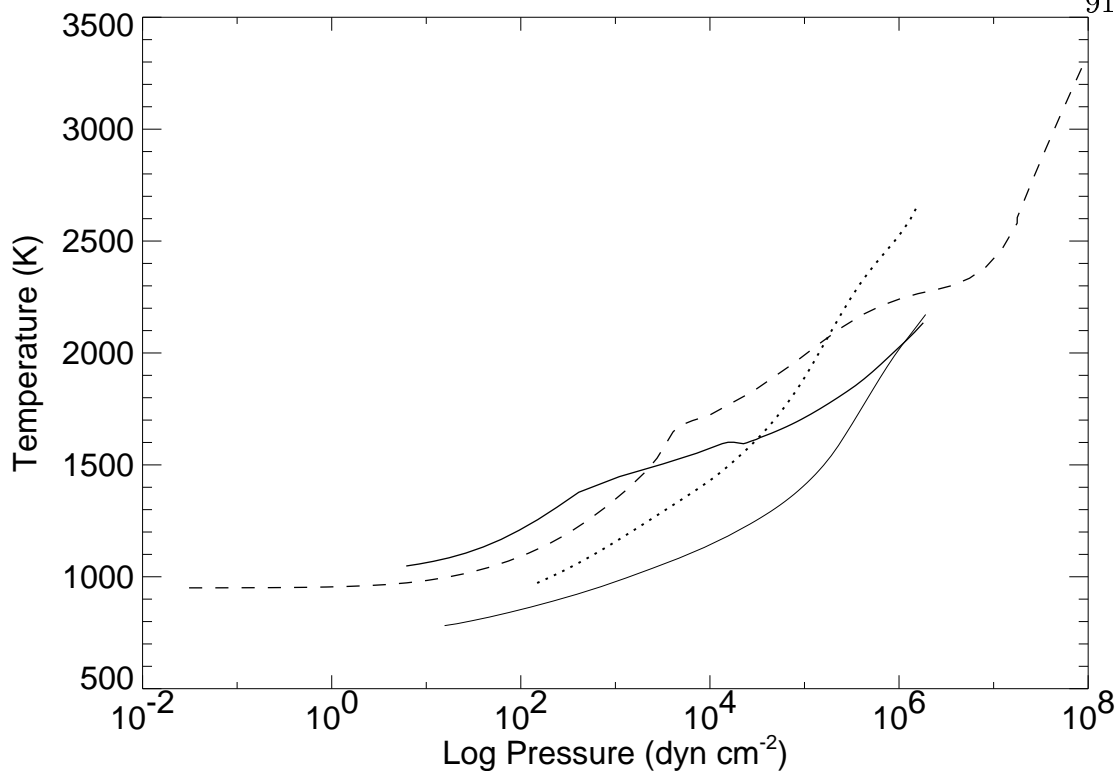


Figure 5.4: Temperature-pressure profiles of the four fiducial cases. The dashed curve is from the Sudarsky et al. (2003) model, the thick solid curve is the cloudy  $f = 1$  case, the thin lower curve is the cloudless  $f = 1$  case, and the dotted line is the cloudless  $f = 2$  case.

by taking  $R_p = 1.42 R_J$  (Cody & Sasselov, 2002) and  $R_* = 1.146 R_\odot$ . This yields approximately twice their tabulated contrast values, because their contrast is phase-averaged (Sudarsky, private communication, 2002). Using their temperature-pressure profile as input, we calculate a flux peak of similar but slightly larger magnitude with our simplified spectral synthesis code, and the differences could be explained by the fact that we ignore their cloud opacities in our calculation. Note that our limit is based on the Sudarsky et al. (2003) flux divided by the Kurucz model, NOT on our re-calculation of the spectrum.

The assumed redistribution of incident stellar radiation is also different among the models. We define the redistribution factor  $f$ , where the  $f = 1$  case

represents the situation in which the incident radiation is evenly redistributed over the entire planet. The  $f = 2$  case represents the one in which the incident radiation is completely absorbed and re-emitted on the day side of the planet. The Sudarsky et al. (2003) model assumes  $f = 2$  (or equivalently,  $f = 0.5$  using their definition of  $f$ ). As noted, our first case for comparing with the observational results is the Sudarsky et al. (2003) flux divided by the Kurucz model. We choose three other cases as fiducial models for comparison with the data. These have been selected in order to test a wide range of the possible physical conditions in the atmosphere. We choose two  $f = 1$  models, one with no clouds and one with cloud opacity due to  $\text{MgSiO}_3$ , Fe, and  $\text{Al}_2\text{O}_3$ . Since the Sudarsky et al. (2003) model considers cloud opacities and assumes  $f = 2$ , we further select a cloudless model with  $f = 2$ . The temperature profiles of these four cases are shown in Figure 5.4, and the results for the four flux peaks (the Sudarsky et al. (2003) result as well as the cloudless and cloudy fiducial cases) are shown in Figure 5.5.

## 5.5 Results and Interpretation

We now fit these four modeled flux peaks to the data using linear least squares, as in

$$r_i = a + bm_i, \quad (5.7)$$

where  $r_i$  represents the resulting difference spectrum (shown in Figure 5.3),  $m_i$  represents the contrast ratio from a given model,  $i$  represents the wavelength bin, and  $a$  and  $b$  are the coefficients of the fit. The slope of this fit,  $b$ , which we call the ‘model amplitude,’ therefore represents the ‘amount’ of the model signal that appears in the data. A model amplitude of unity would mean that the model clearly fits the data (depending on the errors), while a value of zero represents no correlation between the model and the data. Note that the y-offset between

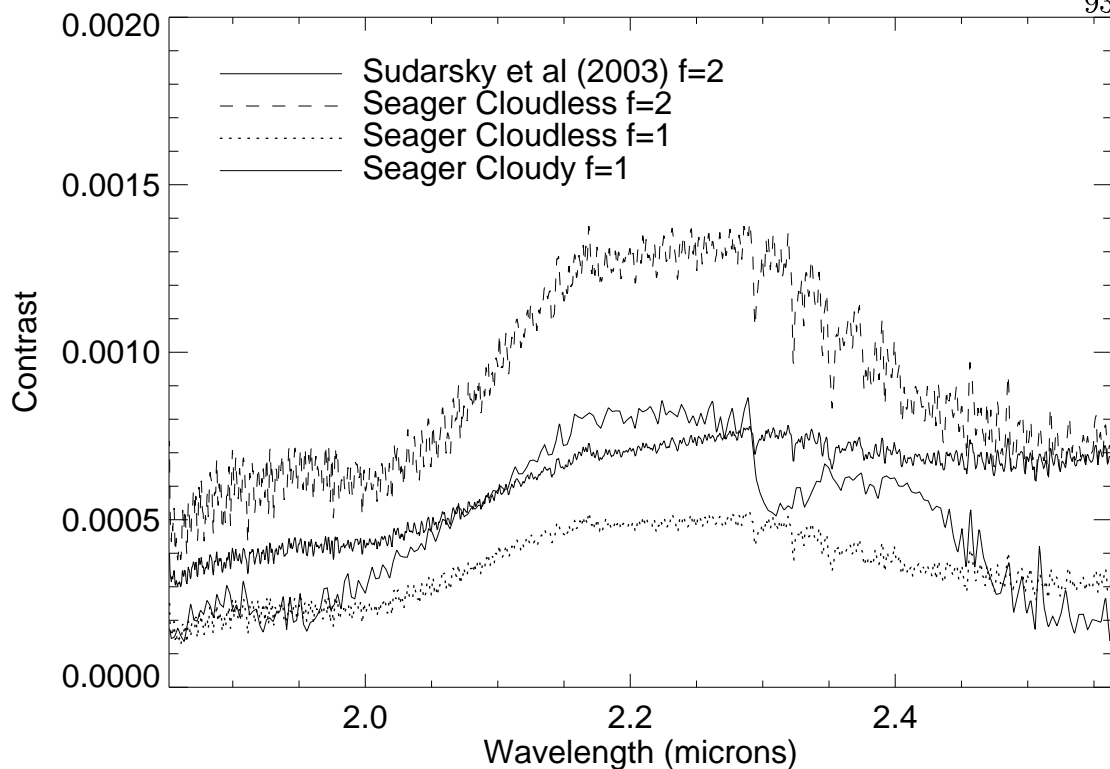


Figure 5.5: Comparison of contrast for the four fiducial cases. Uppermost dashed curve is the cloudless  $f = 2$  case. The thick middle curve is the cloudy  $f = 1$  case, and the lower dotted curve is the cloudless  $f = 1$  case; these three are the result of the simple spectral synthesis calculations, plotted at a spectral resolution of 1500. The thin, solid curve is the Sudarsky et al. (2003) result for the planetary flux divided by the Kurucz model (see text).

the model and the data is irrelevant, since we are searching only for the evidence of the shape of a given model within the data. For the model given by Sudarsky et al. (2003), the resulting model amplitude is  $-0.04 \pm 0.28$ , indicating that this  $f = 1$  model is excluded by our data at the  $3\sigma$  level. For our other cases, the results are  $0.02 \pm 0.57$  for the cloudless ( $f = 1$ ) case,  $-0.25 \pm 0.47$  for the cloudy ( $f = 1$ ) case, and  $0.03 \pm 0.20$  for the cloudless ( $f = 2$ ) case. The two models with  $f = 1$  are not rejected quite so strongly.

The least squares fit described above is difficult to interpret for models with small amplitude flux peaks, as in some of our scaled models. It is also desirable

Table 5.1: Results of our ‘fake data’ simulations for the fiducial cases. The value  $N_f$  represents the number of detection failures in  $10^5$  trials, as plotted in Figure 5.6.

Model	$\Delta T$ (K)	$N_f$
Cloudless ( $f=1$ )	960.36	11127
Cloudless ( $f=2$ )	1265.38	15
Cloudy ( $f=1$ )	797.92	3183
Sudarsky et al. (2003) Flux Ratio* ( $f=2$ )	–	360

\*As calculated by dividing planetary flux by the Kurucz model; see Figure 5.5 (thin, middle curve).

to explore another way to quantify the degree to which the four specific models are rejected by the data. We use a Monte Carlo technique to accomplish this. To quantify the statistical significance of the rejection of any particular model, we constructed ‘fake data’ by adding normally-distributed noise to the modeled contrast values, with  $\sigma$  equal to the size of the error bar in each bin of Figure 5.3. We created  $10^5$  fake data sets for each model and then fit each one to the original model using linear least squares (in the same way in which the real data were fit to the model to calculate the model amplitude). Next, we determine the number of resulting model amplitudes which are less than or equal to the value obtained by fitting the original model to the actual data. We call this the number of detection failures,  $N_f$ , out of  $10^5$  trials. Since the data are essentially flat, we are not seeking to determine which models are detected (none are); rather, we want to know which models **would have been detected**, given the errors in the data, and can therefore be rejected. Thus, the lower the value of  $N_f$ , the stronger a given model is rejected by the data. The results for the four specific models discussed thus far are shown in Table 5.1, and are also plotted in Figure 5.6 (filled symbols). The Sudarsky et al. (2003) result and the cloudless  $f = 2$  case are rejected, while the cloudless and cloudy ( $f = 1$ ) fiducial cases are more acceptable.

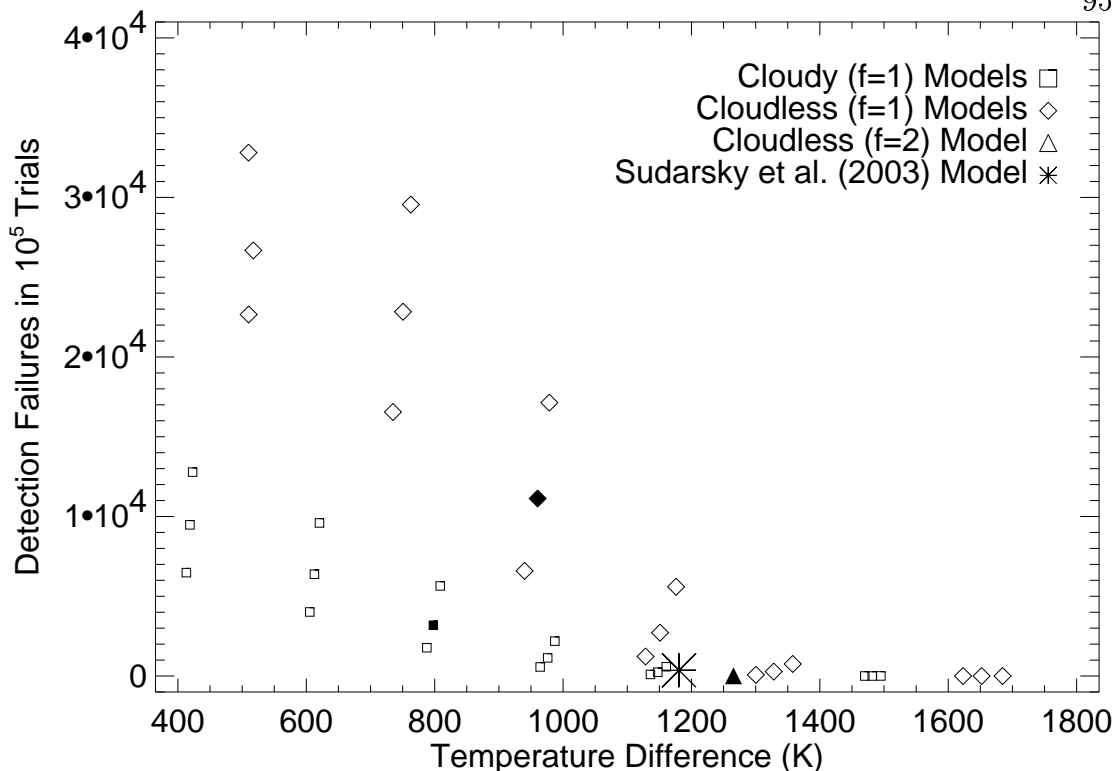


Figure 5.6: Number of detection failures out of  $10^5$  for a suite of scaled models vs.  $\Delta T$ , which represents the difference between the temperature at optical depth unity at the center of the bandpass and the boundary temperature (see Equation 5.4). See Table 5.2 for details of each scaled profile. The filled symbols, along with the asterisk, represent the four fiducial cases described in Table 5.1.

We tested our suite of scaled models, with the prescription given by Equation 2.38, using this technique. The parameters and results of these models are shown in Table 5.2 for the cloudless and cloudy  $f = 1$  cases. The results of  $N_f$  vs.  $\Delta T$  are plotted in Figure 5.6 for both sets of models. Now we must choose a limit on  $N_f$  to conclude that a given model is rejected by the data. We take 1%, or  $N_f = 1000$  as a conservative rejection limit. Table 5.2 shows that 6 of the scaled cloudless  $f = 1$  models can be rejected as inconsistent with the data. These correspond to steeper scaled profiles, with  $\gamma \geq 1.5$ . Thus, we can see that the temperature profiles with a higher temperature gradient, causing a larger peak near  $2.2 \mu\text{m}$  in the emergent spectrum, can be eliminated as inconsistent with

Table 5.2: Scaling parameters for each cloudless and cloudy  $f = 1$  profile. The value  $N_f$  represents the number of detection failures in  $10^5$  trials, as plotted in Figure 5.6.

	$\Delta T$ (K)	$\gamma$	$T_{\text{offset}}$	$N_f$
Cloudless	517.42	0.50	0	26680
	510.21	0.50	100	22665
	510.00	0.50	-100	32808
	750.58	0.75	0	22834
	734.92	0.75	100	16550
	762.85	0.75	-100	29557
	960.36	1.00	0	11127
	939.94	1.00	100	6589
	978.55	1.00	-100	17136
	1151.05	1.25	0	2714
	1128.48	1.25	100	1225
	1175.98	1.25	-100	5594
	1328.16	1.50	0	280
	1300.31	1.50	100	73
	1357.76	1.50	-100	758
	1652.07	2.00	0	0
	1623.06	2.00	100	0
	1684.67	2.00	-100	0
Cloudy	418.63	0.50	0	9477
	413.15	0.50	100	6482
	422.91	0.50	-100	12783
	612.63	0.75	0	6383
	605.37	0.75	100	4014
	620.46	0.75	-100	9597
	797.92	1.00	0	3183
	787.74	1.00	100	1772
	808.55	1.00	-100	5646
	976.03	1.25	0	1136
	964.24	1.25	100	568
	987.11	1.25	-100	2189
	1147.48	1.50	0	240
	1136.11	1.50	100	97
	1160.71	1.50	-100	584
	1481.52	2.00	0	2
	1470.01	2.00	100	1
	1495.06	2.00	-100	6

our observations. The more isothermal profiles, on the other hand, are consistent with the data. Furthermore, 7 of the scaled cloudy  $f = 1$  profiles tested also can be rejected. All of the profiles with  $\gamma \geq 1.25$  and positive  $T_{\text{offset}}$  fall below the detection limit and are clearly inconsistent with the data. Figure 5.6 indicates that only models with  $\Delta T \lesssim 1100$  K are consistent with our data. Note that the rejection also depends on  $T_{\text{offset}}$  from Equation 2.38; for example, the higher values have raised the temperature profile such that it is clearly rejected by the data. The rejection limit, however, is strongly dependent on  $\Delta T$ .

## 5.6 Conclusion

Our results are extremely sensitive to the shape of temperature-pressure profile, which is as expected, given that the Planck function varies strongly with temperature in this wavelength region. Besides the shape of the profile, there are a variety of other possible processes in the planetary atmosphere that could render the planet undetectable with these observations. For example, the broad peak in the spectrum near  $2.2 \mu\text{m}$  is caused by the large number of weak water lines on either side of this feature. Absorption by these lines lowers the continuum level on either side, thus creating the peak. One obvious process by which the peak would not appear is a lowering of the water abundance in the planetary atmosphere. We tested this idea and found that only when the water abundance was lowered by a factor of 10 did the peak become small enough to escape detection using our method. This value for the water abundance ( $\sim 9.8 \times 10^{-5}$ ) seems unrealistically small.

The atmospheric dynamics of HD 209458 b could also have a strong impact on the emergent spectrum. The Sudarsky et al. (2003) model assumes that the heat is absorbed and re-radiated only on the day side ( $f = 2$ ), thus giving rise to a hot side and a cold side of the planet. Since this model is rejected by our

data, this implies that the large temperature asymmetry scenario may not be viable and that some sort of transport mechanism must be at work to move the incident energy from the hot to the cold side. Showman & Guillot (2002) suggest that the day-night temperature difference may be as great as 300 K, leading to strong winds of  $1 \text{ km s}^{-1}$  or more. We further caution that we have observed only two secondary eclipses of HD 209458 b. Recent simulations by Cho et al. (2003) indicate that the temperature asymmetry between the two hemispheres may be time-variable; this effect can be so strong as to render the day side to be colder than the night side at times.

We suggest two ways in which the  $2.2 \mu\text{m}$  flux peak would be lowered sufficiently to be consistent with our observations. The first is the efficient redistribution of the incident radiation over the entire planet. A subset of these models, specified by  $f = 1$  with no clouds and assuming solar abundance of elements, seem to be consistent with our data. Second, additional opacity in the upper atmosphere will flatten the T/P profile, reducing the relative amplitude of the  $2.2 \mu\text{m}$  peak. For example, the T/P profiles shown by Barman et al. (2001) are nearly isothermal, and will certainly produce  $2 \mu\text{m}$  spectra consistent with our observed limit. Barman (2003, private communication) attributes this behavior to their treatment of the opacity, specifically the inclusion of strong gaseous opacity due to metals. We suggest that a high-altitude cloud (favored by Charbonneau et al. (2002) to explain their low sodium result) would also make the atmosphere more isothermal if the cloud is sufficiently absorbing. Note, however, that the Charbonneau et al. (2002) sodium result requires placing such a cloud at the limb of the planet, whereas our results require the clouds to be broadly distributed on the day side.

Finally, we note that our results have been obtained using the 3-meter IRTF, indicating that valuable observations of extrasolar planets, leading to new infor-

mation on the atmospheres of these objects, can be conducted using smaller telescopes from the ground, given favorable observing conditions and careful analysis.

## Chapter 6

### Conclusion

The field of extrasolar planet detection and characterization is currently one of the newest and most exciting research topics in astrophysics, and the transiting planet HD 209458 b has generated much interest and a wealth of new knowledge on the subject. This chapter concludes by summarizing the results of this research on HD 209458 b and by giving some ideas for future observational studies on this and other transiting planets to be discovered in the future.

#### 6.1 Implications for HD 209458 b

We have discussed at length the observations of HD 209458 b performed at the IRTF and the VLT in 2001. These observations represent the first attempts to detect the secondary eclipse in the infrared region of the spectrum. Although we have not yet been able to detect the planet atmosphere directly, the high sensitivity of our measurements has allowed us to place strong limits on the properties of the atmosphere. We now discuss the significance of our results, as well as other measurements of HD 209458 b, in the context of the physical processes at work in the atmosphere.

The IRTF results described in Chapter 5 have interesting implications for the physical structure of the atmosphere of HD 209458 b in the 2.0–2.5  $\mu\text{m}$  region. Our resulting spectrum was essentially flat; we saw no evidence for the flux peak

near  $2.2 \mu\text{m}$  as predicted by some models. Because the Planck function varies strongly with temperature in this wavelength region, we expect the results to be extremely sensitive to the temperature-pressure profile. We find overall that the steeper profiles (the ones with a higher temperature gradient) are excluded by the data, while the more isothermal ones are more consistent. As discussed in Chapter 4, the VLT results show no evidence for methane absorption in the  $3.5\text{--}3.7 \mu\text{m}$  region, although these results depend on the eclipse timing.

The detection of the sodium doublet in transmission represents the first detection of an extrasolar planet atmosphere. From these measurements, Charbonneau et al. (2002) concluded that the sodium equivalent width was about a factor of three lower than expected. Preliminary results from another observational program suggest that CO is not detected in transmission (Brown, private communication, 2002). Finally, we note the radius of HD 209458 b is larger than that of Jupiter ( $R_p = 1.42R_J$ ).

One explanation for these observed results is that a high cloud deck covers the upper layers of the atmosphere. This would be an unfortunate situation for observers hoping to learn about the composition and structure of the atmosphere of HD 209458 b. Such a situation would severely restrict radiation from the deepest layers from reaching the top of the atmosphere. If this were the case, the continuum would be formed high in the atmosphere, meaning that the column density of a given species would be much smaller. This would imply that spectral features would be difficult to detect.

As described in Section 6.2, the high cloud would also have a strong impact on the temperature structure in the atmosphere. If it were strongly absorbing, the upper layers would be heated, thus flattening the temperature profile. On the other hand, if the cloud were strongly reflecting, a smaller fraction of the incident radiation would reach the deeper layers of the atmosphere, causing those layers to

be cooler. In both cases, the overall effect is to make the temperature profile more isothermal. We have shown that this case is consistent with the short-wavelength IRTF data, but in fact, it is also consistent with other observational programs to detect the atmosphere of HD 209458 b. For example, one explanation of the observed low sodium abundance is the presence of a high cloud on the terminator (Charbonneau et al., 2002). We also note that this idea is consistent with the fact that we were not able to detect methane in the VLT results, although the non-detection was only for certain eclipse timings.

Another situation that would drastically change the structure of the planet atmosphere is photochemistry in the upper atmosphere. That is, the chemical composition of the planetary atmosphere may not be described by thermochemical equilibrium considerations. Because of the planet's proximity to its star, photochemical processes could have a drastic effect on the emergent spectrum. Recalling that this is a Jupiter-sized planet orbiting at 0.042 AU (approximately ten times closer to the primary than Mercury is to the Sun), it is clear that the ultraviolet flux density at the top of the atmosphere must be a large effect. A consideration of this effect has not yet been reported in the context of extrasolar planetary atmospheres.

## 6.2 The Effect of Clouds on Temperature Structure

Since the IRTF results exclude models for the planetary atmosphere with large temperature gradients, we consider the effect of clouds on the temperature structure. The following discussion is based on a derivation from Salby (1996, Section 8.5). We begin with the expressions for the upwelling and downwelling flux density, as derived using the well-known two-stream approximation:

$$\frac{dF_{\lambda}^{\uparrow}}{d\tau_{\lambda}^*} = F_{\lambda}^{\uparrow} - S_{\lambda}^* \quad (6.1)$$

$$-\frac{dF_{\lambda}^{\downarrow}}{d\tau_{\lambda}^*} = F_{\lambda}^{\downarrow} - S_{\lambda}^*. \quad (6.2)$$

The superscript (\*) refers to the simplifying approximation that the optical depth scale is given by

$$\tau_{\lambda}^* = \bar{\mu}^{-1} \tau_{\lambda}, \quad (6.3)$$

where  $\bar{\mu}$  is called the diffusivity factor and essentially represents an effective inclination that can be used to eliminate the integral over zenith angle. We ignore scattering effects and take the source function  $S_{\lambda}^*$  to be the Planck function  $B_{\lambda}^*$ . The derivation also assumes that the atmosphere is gray, meaning that the absorption is independent of wavelength. We further define the expressions for the net flux density and the total flux density:

$$F = F^{\uparrow} - F^{\downarrow} \quad (6.4)$$

$$\bar{F} = F^{\uparrow} + F^{\downarrow}. \quad (6.5)$$

We consider two cases. The first is the situation in which the incident short wavelength (SW) radiation is completely transmitted through the atmosphere and absorbed by the surface; since the atmosphere is transparent to the SW radiation, this corresponds to the cloudless case. The surface then re-radiates long wavelength (LW) radiation, and each layer of the atmosphere then absorbs and re-emits LW radiation.

Looking at Equations 6.1 and 6.2, we can add and subtract the two expressions and transform them using Equations 6.4 and 6.5. This leads to

$$\frac{dF}{d\tau^*} = \bar{F} - 2B^* \quad (6.6)$$

$$\frac{d\bar{F}}{d\tau^*} = F. \quad (6.7)$$

We note that under the assumption of radiative equilibrium, the net flux density  $F$  is equal to a constant, from the first law of thermodynamics. That is, there is

no source or sink of radiation within the atmosphere. Thus, Equation 6.7 can be integrated directly to obtain

$$\bar{F} = F\tau^* + C, \quad (6.8)$$

while Equation 6.6 reduces to

$$\bar{F} = 2B^*. \quad (6.9)$$

By equating 6.8 and 6.9, we have

$$B^*(\tau^*) = \frac{F}{2}\tau^* + B_0^*. \quad (6.10)$$

The quantity  $B_0^*$  represents the amount of radiation emitted at the top of the atmosphere. We can determine this quantity explicitly by balancing the SW radiation incident on the top of the atmosphere (given by  $F_0$ ) with the outgoing LW radiation emitted at the top:

$$F^\uparrow(0) = F_0.$$

At the top of the atmosphere,  $\tau^* = 0$ , and the downwelling LW radiation vanishes:

$$F^\downarrow(0) = 0.$$

Applying this to Equation 6.4 for the net flux, we have

$$F = F^\uparrow = F_0 \quad (6.11)$$

and similarly for  $\bar{F}$  from Equation 6.5,

$$\bar{F}(0) = F^\uparrow. \quad (6.12)$$

These expressions can be applied to Equation 6.9 at the top of the atmosphere, leading to

$$B_0^* = \frac{\bar{F}}{2} = \frac{F^\uparrow}{2} = \frac{F_0}{2}. \quad (6.13)$$

Substituting Equation 6.13 into Equation 6.10 gives

$$B^*(\tau^*) = \frac{F_0}{2}(\tau^* + 1). \quad (6.14)$$

Finally, we can now calculate the temperature as a function of optical depth using the Stefan-Boltzmann Law (see Equation 2.11):

$$T(\tau^*) = \left[ \frac{F_0}{2\sigma}(\tau^* + 1) \right]^{\frac{1}{4}} \quad (6.15)$$

For the second case, we depart from the derivation in Salby (1996) and assume that the atmosphere absorbs a portion of the incident SW radiation, which simulates the presence of a cloud. Suppose that the SW flux is absorbed according to the usual expression,

$$F_{\text{SW}} = F_0 e^{-\tau'^*}, \quad (6.16)$$

where  $\tau'^*$  is the optical depth scale for the SW radiation. We parameterize this in terms of the LW optical depth scale  $\tau^*$ :

$$\tau'^* = \beta \tau^*. \quad (6.17)$$

The parameter  $\beta$  can be adjusted to control the amount of SW radiation absorbed, simulating the magnitude of the effect of the clouds. This absorbed SW radiation is also re-emitted as LW radiation at each layer, and we assume that it is re-emitted equally in the upward and downward directions:

$$F_{\text{SW}}^{\uparrow} = F_{\text{SW}}^{\downarrow} = \frac{1}{2} F_0 e^{-\beta\tau^*}. \quad (6.18)$$

In this case, we must add a term, given by Equation 6.18, to the source function to account for the absorption. Thus, Equations 6.1 and 6.2 become

$$\frac{dF_{\lambda}^{\uparrow}}{d\tau_{\lambda}^*} = F_{\lambda}^{\uparrow} - B_{\lambda}^* - \frac{1}{2} F_0 e^{-\beta\tau^*} \quad (6.19)$$

$$-\frac{dF_{\lambda}^{\downarrow}}{d\tau_{\lambda}^*} = F_{\lambda}^{\downarrow} - B_{\lambda}^* - \frac{1}{2} F_0 e^{-\beta\tau^*}. \quad (6.20)$$

The derivation continues almost exactly as in the first case. We add and subtract Equations 6.19 and 6.20 to obtain

$$\frac{dF}{d\tau^*} = \bar{F} - 2B^* - F_0 e^{-\beta\tau^*} \quad (6.21)$$

$$\frac{d\bar{F}}{d\tau^*} = F. \quad (6.22)$$

Note that we can still define the net flux density and the total flux density as in Equations 6.4 and 6.5 and that the assertion that the net LW flux density is constant is still valid. We then have

$$\bar{F} = F\tau^* + C, \quad (6.23)$$

exactly as before, and

$$\bar{F} = 2B^* - F_0 e^{-\beta\tau^*}. \quad (6.24)$$

By equating the two expressions (6.23 and 6.24) for  $\bar{F}$ , we obtain

$$B^*(\tau^*) = \frac{F_0}{2} e^{-\beta\tau^*} + \frac{F}{2}\tau^* + B_0^*. \quad (6.25)$$

Now we can eliminate  $F$  by balancing the incident SW radiation with the upwelling LW radiation at the top of the atmosphere, just as before:

$$F_0 = F^\uparrow(0) + \frac{1}{2} F_0 e^{-\beta\tau^*(0)}.$$

Since  $\tau^*(0) = 0$ , this reduces to

$$F^\uparrow(0) = \frac{F_0}{2} \quad (6.26)$$

Note that from Equation 6.4 and the fact that the downwelling radiation vanishes at the top, we also have

$$F = \frac{F_0}{2}. \quad (6.27)$$

Next we find an expression for  $B_0^*$  in Equation 6.25 by combining Equations 6.24 and 6.5:

$$\bar{F} = 2B^* - F_0 e^{-\beta\tau^*} = F^\uparrow + F^\downarrow,$$

and evaluating at  $\tau^*(0) = 0$  to obtain

$$\bar{F} = 2B_0^* - F_0 = F^\uparrow = \frac{F_0}{2}, \quad (6.28)$$

where we have used Equation 6.27 in the final equality. Solving for  $B_0^*$ , we have

$$B_0^* = \frac{3}{4} F_0 \quad (6.29)$$

We now substitute Equations 6.27 and 6.29 into Equation 6.25:

$$B^*(\tau^*) = \frac{F_0}{2} \left( e^{-\beta\tau^*} + \frac{\tau^*}{2} \right) + \frac{3}{4} F_0. \quad (6.30)$$

Finally, just as in the first case above (see Equation 6.15), we use the Stefan-Boltzmann law to calculate the run of temperature with optical depth:

$$T(\tau^*) = \left[ \frac{1}{\sigma} \left[ \frac{F_0}{2} \left( e^{-\beta\tau^*} + \frac{\tau^*}{2} \right) + \frac{3}{4} F_0 \right] \right]^{\frac{1}{4}}. \quad (6.31)$$

We are now in a position to consider the difference in the temperature profile for the two cases. We take the incident SW flux  $F_0$  to be the radiation from a 6000 K blackbody, multiplied by the solid angle subtended by the star at the planet's orbital distance. The result for the temperature profile for both cases is shown in Figure 6.1, where the solid line represents the case with no absorption of SW radiation (given by Equation 6.15), and the dashed line represents the case with inclusion of absorption of SW radiation (given by Equation 6.31). As shown, with the absorption of some SW radiation in the upper layers of the atmosphere, the temperature of these layers has increased; consequently, less radiation reaches the deeper layers, causing them to cool off and thus decreasing the overall temperature gradient. For this plot, a value of  $\beta = 0.7$  has been assumed. We note that for larger values,  $\beta \gtrsim 1.5$ , a temperature inversion begins to appear, as expected.

### 6.3 Continuing Work

The analysis of the data obtained at the IRTF and the VLT is continuing, to determine what other information can be extracted from the data. As

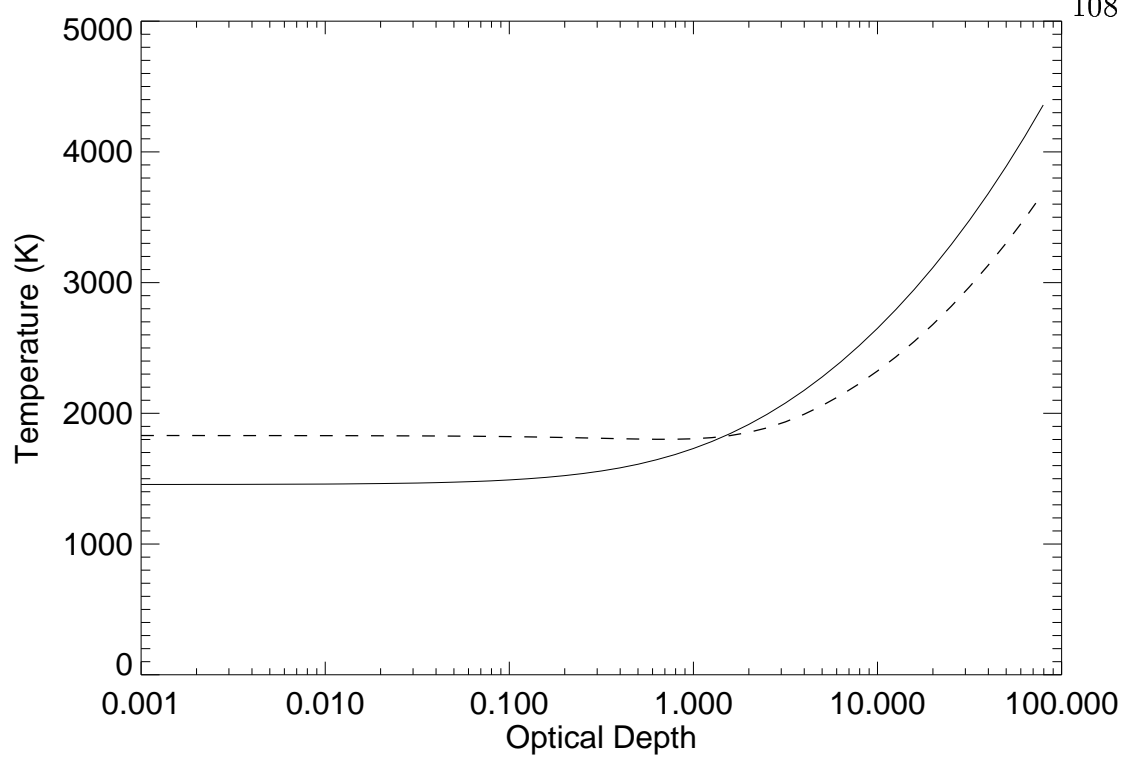


Figure 6.1: The solid line represents the resulting temperature profile when the atmosphere is assumed to be transparent to the incident SW radiation. The dashed line is the result for the assumption that the incident SW radiation is absorbed according to the usual  $e^{-\tau}$ .

alluded to in Chapter 5, no result was obtained using the long wavelength region of the IRTF data. The two longest-wavelength orders (3–4  $\mu\text{m}$ ) were dominated by variations in the terrestrial atmospheric absorption, making extraction of the planetary signal difficult at best. However, early work on these data suggested possible evidence for the planetary signal, and the investigation continues. Finally, with a new version of Spextool released very recently, we intend to re-extract the spectra from the raw images. Since the new version has the capability to perform optimal extractions, this may alleviate the problem with terrestrial atmospheric absorption in the long wavelength orders.

Furthermore, the variability of the terrestrial atmosphere is another problem that may be addressed by our data. The IRTF data recorded continuous

monitoring of the terrestrial background in the unused portions of the slit. This information, combined with our methods of removing the terrestrial background, could be useful to other researchers in the field of infrared astronomy. Few projects have achieved such small error levels in the analysis of infrared spectroscopy.

## **6.4 Future Studies**

In this section we briefly outline some of the exciting future observational possibilities that will certainly lead to even more information about HD 209458 b.

### **6.4.1 Day-Night Temperature Asymmetry**

The question of atmospheric dynamics and circulation in the atmosphere of HD 209458 b can be probed with further observations. The orbit of the planet is nearly circular, and the planet is expected to be tidally locked. That is, the same side of the planet will always be facing the star, meaning that the incident stellar radiation will always be absorbed by the ‘day side.’ The large amount of absorbed stellar radiation suggests a mechanism for transporting the energy from the day side to the night side. An observational program that could address this question is a temperature measurement of the planet during primary eclipse and just before secondary eclipse (Charbonneau et al., 2000). Calculations by Showman & Guillot (2002) suggest that the day-night temperature difference could reach as much as 300 K, giving rise to large wind speeds, as high as 1 km/s. A measurement of the infrared light curve of the planet may be possible within the next few years, using upcoming space instruments. Showman & Guillot (2002) point out that observations of the infrared light curve of HD 209458 b will help constrain the direction and magnitude of planetary winds, by discerning temperature changes in the atmosphere as a function of longitude.

### 6.4.2 Space-Based Observations

An exciting prospect for future observations of this and other transiting extrasolar planets is the opportunity for observing from space. A large part of the current work has been to correct for the variations in the terrestrial atmosphere; this problem is avoided altogether by performing the observations from space. We describe some of the upcoming space missions relating to infrared astronomy and how they can be applied to observations of extrasolar planets.

The Space Infrared Telescope Facility (SIRTF), scheduled to launch in April 2003, is the third of NASA's Great Observatories, covering the infrared region of the spectrum, with a wavelength coverage of 3–180  $\mu\text{m}$ . One of the main scientific goals of SIRTF is the characterization of brown dwarfs and extrasolar planets.<sup>1</sup> SIRTF is a 0.85-meter telescope that will be placed in an Earth-trailing orbit around the Sun. One of the three instruments on SIRTF is the Infrared Spectrograph (IRS), which provides six modes for low and high resolution spectroscopy in the wavelength region between 5 and 40  $\mu\text{m}$ . The low resolution, short wavelength mode, for example, covers 5.3–14  $\mu\text{m}$  at  $R \sim 62$ –124.<sup>2</sup>

The Stratospheric Observatory for Infrared Astronomy (SOFIA),<sup>3</sup> a joint project of NASA and the German Aerospace Center, is an airborne observatory slated to see first light in late 2004. It is a 2.5-meter telescope mounted aboard a modified Boeing 747SP aircraft. Nine instruments are currently planned for SOFIA. One is the Echelon-Cross-Echelle Spectrograph (EXES), which will provide wavelength coverage between 5 and 28  $\mu\text{m}$ . The instrument has three resolution modes:  $10^5$ ,  $10^4$ , and 3000.

The James Webb Space Telescope (JWST),<sup>4</sup> formerly the Next Generation

---

<sup>1</sup> <http://sirtf.caltech.edu/science/overview/index.shtml>

<sup>2</sup> <http://sirtf.caltech.edu/SSC/obs/overview.html>

<sup>3</sup> <http://sofia.arc.nasa.gov/>

<sup>4</sup> <http://www.stsci.edu/jwst/overview/design/index.html>

Space Telescope, is currently poised to move from Phase A, the planning and technical study stage, to Phase B, the definition stage. Thus, many of the details are in a state of flux, and the specifics of the final instrument suite are not known. The basic design is a 6-meter telescope placed in orbit around the second Lagrange (L2) point, where the thermal effects from the Earth and Moon are small. Currently, three instruments are planned for the JWST focus on the infrared region of the spectrum. The Near-Infrared Spectrograph (NIRSpec) will provide spectroscopy in the wavelength region 0.6–5  $\mu\text{m}$ . It will have a field of view of 3' by 3', allowing simultaneous spectra of over 100 objects. This suggests the possibility of recording the comparison star truly simultaneously with the observations of HD 209458; we note however, that HD 210483 is nearly a degree away from HD 209458, and therefore both could not be observed in the same field of view. NIRSpec will have two options for the resolving power,  $R \sim 100$  or  $R \sim 1000$ .

The examples cited here represent only a few of the space-based infrared instruments under development. Observations from space will improve measurements because the variable terrestrial atmosphere will not interfere with the observations. More importantly, we will be able to search for spectral features of  $\text{H}_2\text{O}$  and  $\text{CH}_4$ , which can be difficult from the ground because the Earth's atmosphere contains these molecular species. Water is almost certain to be abundant in the atmospheres of extrasolar giant planets (e.g. Hubbard et al., 2001), but detecting this species from the ground is problematic at best.

## 6.5 In Closing

The work described here represents an important addition to the growing body of knowledge of extrasolar planets. The techniques described in this work can be applied to other transiting extrasolar planets certain to be discovered in the coming years. Numerous ground-based observational programs to search for

transits are already in place and more are being planned. The Kepler mission is a Discovery-class mission recently selected by NASA that is planned for launch by 2007. Depending on the frequency of planet formation, Kepler could detect hundreds of Earth-sized extrasolar planets in its four-year mission, and over a thousand Jupiter-sized planets (Borucki et al., 2002). We also note that our technique could even be applied to planets that do not transit, by using differences in radial velocity between the star and planet (Wiedemann et al., 2001).

With the ongoing characterization of the physical parameters, chemical composition, and atmospheric dynamics of HD 209458 b and the discovery of more extrasolar planets, we learn more about the frequency of planet formation in the galaxy. Already useful statistics have been obtained regarding the mass distribution of planets. With the discovery of smaller and smaller planets, we are now at the threshold of discovering Earth-like planets around other stars, the main scientific objective of the Kepler mission. Knowledge of the frequency of other planets in the galaxy and their characteristics help us to study our own solar system in the context of the rest of the galaxy.

## Bibliography

- Anders, E. & Grevesse, N. 1989, *Geochim. Cosmochim. Acta*, 53, 197
- Armitage, P. J. & Bonnell, I. A. 2002, *MNRAS*, 330, L11
- Barman, T. S., Hauschildt, P. H., & Allard, F. 2001, *ApJ*, 556, 885
- Barman, T. S., Hauschildt, P. H., Schweitzer, A., Stancil, P. C., Baron, E., & Allard, F. 2002, *ApJ*, 569, L51
- Barnard, E. E. 1916, *AJ*, 29, 181
- Borucki, W. J., Koch, D. G., Basri, G., Cochran, W., Dunham, E. W., Gilliland, R., Jenkins, J. M., Caldwell, D., Kondo, Y., Latham, D., & Geary, J. 2002, in *NASA Laboratory Astrophysics Workshop*
- Borysow, A. 2002, *A&A*, 390, 779
- Boss, A. P. 2001, *ApJ*, 563, 367
- Brown, L. R., Dulick, M., & Devi, V. M. 2001a, *AAS/Division for Planetary Sciences Meeting*, 33, 0+
- Brown, T. M. 2001, *ApJ*, 553, 1006
- Brown, T. M., Charbonneau, D., Gilliland, R. L., Noyes, R. W., & Burrows, A. 2001b, *ApJ*, 552, 699
- Brown, T. M., Libbrecht, K. G., & Charbonneau, D. 2002, *PASP*, 114, 826
- Buie, M. W., Cruikshank, D. P., Lebofsky, L. A., & Tedesco, E. F. 1987, *Nature*, 329, 522+
- Bundy, K. A. & Marcy, G. W. 2000, *PASP*, 112, 1421
- Burrows, A., Guillot, T., Hubbard, W. B., Marley, M. S., Saumon, D., Lunine, J. I., & Sudarsky, D. 2000, *ApJ*, 534, L97
- Burrows, A. & Sharp, C. M. 1999, *ApJ*, 512, 843

- Butler, R. P., Marcy, G. W., Williams, E., McCarthy, C., Dosanjuh, P., & Vogt, S. S. 1996, *PASP*, 108, 500
- Castellano, T., Jenkins, J., Trilling, D. E., Doyle, L., & Koch, D. 2000, *ApJ*, 532, L51
- Charbonneau, D., Brown, T. M., Latham, D. W., & Mayor, M. 2000, *ApJ*, 529, L45
- Charbonneau, D., Brown, T. M., Noyes, R. W., & Gilliland, R. L. 2002, *ApJ*, 568, 377
- Charbonneau, D., Noyes, R. W., Korzennik, S. G., Nisenson, P., Jha, S., Vogt, S. S., & Kibrick, R. I. 1999, *ApJ*, 522, L145
- Cho, J. Y.-K., Menou, K., Hansen, B. M. S., & Seager, S. 2003, in *ASP Conference Series, Scientific Frontiers in Research on Extrasolar Planets*, D. Deming and S. Seager; Eds.
- Cody, A. M. & Sasselov, D. D. 2002, *ApJ*, 569, 451
- Cushing, M. C., Vacca, W. D., & Rayner, J. T. 2003, *PASP*, submitted
- Farmer, C. B. 1989, *A High-Resolution Atlas of the Infrared Spectrum of the Sun and the Earth Atmosphere from Space: A Compilation of the ATMOS Spectra of the Region from 650 to 4800  $cm^{-1}$  (2.3 to 16  $\mu m$ )*, Reference Publication RP-1224, National Aeronautics and Space Administration
- Frommhold, L. 1993, *Collision-Induced Absorption in Gases* (Cambridge University Press)
- Goody, R. 1995, *Principles of Atmospheric Chemistry and Physics* (Oxford University Press)
- Goorvitch, D. 1994, *ApJS*, 95, 535
- Goukenleuque, C. ., Bézard, B., Joguet, B., Lellouch, E., & Freedman, R. 2000, *Icarus*, 143, 308
- Guillot, T., Burrows, A., Hubbard, W. B., Lunine, J. I., & Saumon, D. 1996, *ApJ*, 459, L35+
- Hauck, B. & Mermilliod, M. 1998, *A&AS*, 129, 431
- Henry, G. W., Marcy, G. W., Butler, R. P., & Vogt, S. S. 2000, *ApJ*, 529, L41
- Horne, K. 1986, *PASP*, 98, 609
- Hubbard, W. B., Fortney, J. J., Lunine, J. I., Burrows, A., Sudarsky, D., & Pinto, P. 2001, *ApJ*, 560, 413

- Jørgensen, U. G., Hammer, D., Borysow, A., & Falkesgaard, J. 2000, *A&A*, 361, 283
- Kenworthy, M. A. & Hinz, P. M. 2003, *PASP*, 115, 322
- Kurucz, R. L. 1992, in *IAU Symp. 149: The Stellar Populations of Galaxies*, 225–+
- Linfield, R. P., Colavita, M. M., & Lane, B. F. 2001, *ApJ*, 554, 505
- Liou, K. N. 2002, *An Introduction to Atmospheric Radiation*, 2nd edn. (Academic Press)
- Livingston, W. & Wallace, L. 1991, *An Atlas of the Solar Spectrum in the Infrared from 1850 to 9000 cm<sup>-1</sup> (1.1 to 5.4 μm)*, Tech. Rep. 91-001, National Solar Observatory
- Mammana, D. L. & McCarthy, Jr., D. W. 1995, *Other Suns. Other Worlds?* (St. Martin's Press)
- Marcy, G. W. & Butler, R. P. 1992, *PASP*, 104, 270
- . 2000, *PASP*, 112, 137
- Mayor, M. & Queloz, D. 1995, *Nature*, 378, 355+
- Mazeh, T., Naef, D., Torres, G., Latham, D. W., Mayor, M., Beuzit, J., Brown, T. M., Buchhave, L., Burnet, M., Carney, B. W., Charbonneau, D., Drukier, G. A., Laird, J. B., Pepe, F., Perrier, C., Queloz, D., Santos, N. C., Sivan, J., Udry, S., & Zucker, S. 2000, *ApJ*, 532, L55
- Mihalas, D. 1970, *Stellar Atmospheres* (W. H. Freeman and Company)
- Moorwood, A. F. 1997, in *Proc. SPIE Vol. 2871*, p. 1146-1151, *Optical Telescopes of Today and Tomorrow*, Arne L. Ardeberg; Ed., Vol. 2871, 1146–1151
- Moutou, C., Coustenis, A., Schneider, J., St Gilles, R., Mayor, M., Queloz, D., & Kaufer, A. 2001, *A&A*, 371, 260
- Nidever, D. L., Marcy, G. W., Butler, R. P., Fischer, D. A., & Vogt, S. S. 2002, *ApJS*, 141, 503
- Nieminen, T. A. & Ross, J. E. R. 2001, *Computer Physics Communications*, 142, 160
- Partridge, H. & Schwenke, D. W. 1997, *J. Chem. Phys.*, 106, 4618
- Perryman, M. A. C., Lindegren, L., Kovalevsky, J., Hoeg, E., Bastian, U., Bernacca, P. L., Crézé, M., Donati, F., Grenon, M., van Leeuwen, F., van der Marel, H., Mignard, F., Murray, C. A., Le Poole, R. S., Schrijver, H., Turon, C., Arenou, F., Froeschlé, M., & Petersen, C. S. 1997, *A&A*, 323, L49

- Pugh, L. A. & Rao, K. N. 1976, in *Molecular Spectroscopy: Modern Research*, ed. K. N. Rao, Vol. 2 (Academic Press)
- Rayner, J. T., Toomey, D. W., Onaka, P. M., Denault, A. J., Stahlberger, W. E., Vacca, W. D., Cushing, M. C., & Wang, S. 2003, *PASP*, 115, 362
- Richardson, L. J., Deming, D., Wiedemann, G., Goukenleuque, C., Steyert, D., Harrington, J., & Esposito, L. W. 2003, *ApJ*, 584, 1053
- Robichon, N. & Arenou, F. 2000, *A&A*, 355, 295
- Rothman, L. S., Rinsland, C. P., Goldman, A., Massie, S. T., Edwards, D. P., Flaud, J.-M., Perrin, A., Camy-Peyret, C., Dana, V., Mandin, J.-Y., Schroeder, J., McCann, A., Gamanche, R. R., Wattson, R. B., Yoshino, K., Chance, K., Jucks, K., Brown, L. R., Nemtchinov, V., & Varanasi, P. 1998, *Journal of Quantitative Spectroscopy and Radiative Transfer*, 60, 665
- Salby, M. L. 1996, *Fundamentals of Atmospheric Physics* (Academic Press)
- Sawyer, S. R., Barker, E. S., Cochran, A. L., & Cochran, W. D. 1987, *Science*, 238, 1560
- Schultz, A. B., Kochte, M., Kinzel, W., Hamilton, F., & Jordan, I. 2003, in *ASP Conference Series, Scientific Frontiers in Research on Extrasolar Planets*, D. Deming and S. Seager; Eds., Vol. 294, 479
- Seager, S. & Sasselov, D. D. 1998, *ApJ*, 502, L157
- . 2000, *ApJ*, 537, 916
- Seager, S., Whitney, B. A., & Sasselov, D. D. 2000, *ApJ*, 540, 504
- Showman, A. P. & Guillot, T. 2002, *A&A*, 385, 166
- Sudarsky, D., Burrows, A., & Hubeny, I. 2003, *ApJ*, 588, 1121
- Vacca, W. D., Cushing, M. C., & Rayner, J. T. 2003, *PASP*, 115, 389
- van de Kamp, P. 1963, *AJ*, 68, 515
- Vernazza, J. E., Avrett, E. H., & Loeser, R. 1976, *ApJS*, 30, 1
- Wenger, C. & Champion, J. P. 1998, *Journal of Quantitative Spectroscopy and Radiative Transfer*, 59, 471
- Wiedemann, G. ., Deming, D., & Bjoraker, G. 2001, *ApJ*, 546, 1068
- Wilson, R. E. 1953, *Carnegie Institute Washington D.C. Publication*, 0
- Wittenmyer, R. A., Welsh, W. F., & Orosz, J. A. 2002, *American Astronomical Society Meeting*, 201, 0
- Wolszczan, A. & Frail, D. A. 1992, *Nature*, 355, 145

## Appendix A

### List of Acronyms

Acronym	Meaning
CEGP	Close-in Extrasolar Giant Planet
CIA	Collision-Induced Absorption
Dec	Declination
ESO	European Southern Observatory
FGS	Fine Guidance Sensor
HA	Hour Angle
HJD	Heliocentric Julian Day
HST	Hubble Space Telescope
IRTF	Infrared Telescope Facility
ISAAC	Infrared Spectrometer and Array Camera
JWST	James Webb Space Telescope
OGLE	Optical Gravitational Lensing Experiment
RA	Right Ascension
SIRTF	Space Infrared Telescope Facility
SOFIA	Stratospheric Observatory for Infrared Astronomy
STIS	Space Telescope Imaging Spectrograph
UT	Universal Time
VLT	Very Large Telescope